UNIVERSITY OF CALIFORNIA
Santa Barbara

Microscale solution manipulation using photopolymerized hydrogel membranes and induced charge electroosmosis micropumps

A Dissertation submitted in partial satisfaction
of the requirements for the degree of

Doctor of Philosophy

in

Chemical Engineering

by

Joel Scott Paustian

Committee in Charge:

Professor Todd M. Squires, Chair

Professor Michael Gordon

Professor Samir Mitragotri

Professor Sumita Pennathur

June 2014

The Dissertation of
Joel Scott Paustian is approved:

Professor Michael Gordon

Professor Samir Mitragotri

Professor Sumita Pennathur

Professor Todd M. Squires, Committee Chairperson

April 2014

Microscale solution manipulation using photopolymerized hydrogel membranes and induced charge electroosmosis micropumps

by

Joel Scott Paustian

Acknowledgements

To my advisor, Todd Squires: I cannot thank you enough for all the ways you contributed to my education, professional growth, and research successes. The support, feedback, and freedom you gave was instrumental to enable my growth as a researcher, problem solver, and communicator. I have greatly enjoyed the opportunity to work on exciting technical challenges in your lab and work together to build its microfluidic capabilities to new levels. Thank you for teaching me an intuition about transport phenomena, and for everything you do to help your students succeed.

I would like to thank my committee, Mike Gordon, Samir Mitragori, and Sumita Pennathur, for your help through the years. Your suggestions helped me to overcome several research challenges, and your feedback greatly improved the stories presented here. An extra thanks goes to Mike for being an excellent lab neighbor by sharing tips and knowledge during equipment-building stages of the projects.

Thank you to all the members of the Squires group, for your feedback, shared knowledge, and friendship through the years. In particular I thank Andy Pascall for our early discussions about electrokinetics, microfabrication, and experiments which greatly helped the ICEO work described here. Also, thank you to the excellent undergraduates I mentored for your persistence, patience, and inquisitiveness.

This work would have been greatly hindered without the help of Dave Walker, who taught me about pneumatic control methods and microvalves. Thank you for helping me import those techniques into the Squires Lab.

I would not be here without the stellar mentors from my undergraduate years that helped inspire me to pursue a research career. I would like to thank Sergey Lamansky, Ed Cussler, and Cong Trinh, for your enthusiasm and honesty about the challenges and rewards of research.

I thank my friends for making my time in Santa Barbara enjoyable. My classmates have been a great support network the last five and a half years, from conquering our first homework sets together to tackling our later challenges. I also thank Austin Somers for holding down the fort with our friends Nicholas and Johnny.

To my parents, Harold and Mary Paustian, I give my deepest gratitude for all that you have done for me. You have provided me with a strong foundation, constant encouragement, and invaluable advice. I thank you for prioritizing my education and for being solid role models in your careers. You have always been an inspiration for me.

Finally, to my fiancée Amanda Schmidt: Your companionship has been a daily source of strength. In the hardest of times, your encouragement helped me to finish

what I started. Your love brings out the best in me. I dedicate this work to you and to our future together.

This work was supported by the Arnold and Mabel Beckman Foundation, the Camille and Henry Dreyfus Foundation, and the Institute for Collaborative Biotechnologies through grant W911NF-09-0001 from the U.S. Army Research Office. The content of the information does not necessarily reflect the position or the policy of the Government, and no official endorsement should be inferred. A portion of this work was performed in the UCSB Nanofabrication Facility, part of the NSF-funded NNIN network.

Curriculum Vitæ

Joel Scott Paustian

Education

2014	Doctor of Philosophy in Chemical Engineering, University of California, Santa Barbara. (expected)
2008	Bachelor of Science in Chemical Engineering, University of Minnesota, Twin Cities. *summa cum laude.*

Professional Experience

2008-2014	Graduate Researcher, University of California, Santa Barbara
2008	Intern, Bioinformatics Summer Institute, Minneapolis, MN
2007-2008	Undergraduate Researcher, University of Minnesota, Twin Cities
2006-2007	Technical Aide, 3M Corporation, Maplewood, MN

Refereed Publications

- Joel S. Paustian, Rodrigo Nery Azevedo, Sean B. Thomas-Lundin, Matthew J. Gilkey, and Todd M. Squires. "Microfluidic microdialysis: spatio-temporal control over solution micro-environments using integrated hydrogel membrane microwindows." *Physical Review X* **3** 041010 (2013)
- Joel S. Paustian, Andrew J. Pascall, Neil M. Wilson, and Todd M. Squires. "Induced charge electroosmosis micropumps using arrays of Janus micropillars." *Submitted.*
- Joel S. Paustian, Craig D. Angulo, and Todd M. Squires. "Solvophoresis of colloidal particles: direct velocity measurements under rapidly imposed solvent gradients." *In preparation.*

Conference Presentations

- Joel S. Paustian and Todd M. Squires. "Rapid dialysis in microfluidic devices using hydrogel membrane microwindows: phoretic migration under imposed gradients." American Institute of Chemical Engineers (AIChE) Annual Meeting. San Francisco, CA. 2013.

- Joel S. Paustian and Todd M. Squires. "Rapid dialysis within microfluidic channels: spatio-temporal control of solution micro-environment using hydrogel membrane microwindows." SciX Conference. Milwaukee, WI. 2013.
- Joel S. Paustian, Rodrigo Nery-Azevedo, and Todd M. Squires. "Microfluidic hydrogel structures for controlled concentration gradients and fast solution switching." American Institute of Chemical Engineers (AIChE) Annual Meeting. Pittsburgh, PA. 2012.
- Joel S. Paustian, Mohammad Mirzadeh, Donghun Kim, Aditya S. Khair, Robert Messinger, Trent Huang, Sumita Pennathur, Frederic G. Gibou, Brad F. Chemlka, and Todd M. Squires. "Self-assembly of nano-scale porous structures within microfabricated fluidic systems for sample preconcentration and energy storage." Institute for Collaborative Biotechnologies (ICB) Annual Meeting. Santa Barbara, CA. 2011 and 2012.
- Joel S. Paustian and Todd M. Squires. "Induced charge electro-osmosis micropumps for portable microfluidics: theory and experiment." American Physical Society-Division of Fluid Dynamics (APS-DFD) Annual Meeting. Long Beach, CA. 2010.
- Joel S. Paustian and Todd M. Squires. "An induced charge electro-osmosis micropump." American Institute of Chemical Engineers (AIChE) Annual Meeting. Salt Lake City, UT. 2010.

Awards

2013	Best Poster, American Electrophoresis Society poster competition, SciX Conference, Milwaukee, WI
2011	Best Poster, Amgen-Clorox Graduate Student Symposium, Santa Barbara, CA
2007	Charles Mann award, Department of Chemical Engineering, University of Minnesota, Twin Cities
2004	Ruby Hackett and Weldon Jones award, Institute of Technology, University of Minnesota, Twin Cities

Abstract

Microscale solution manipulation using photopolymerized hydrogel membranes and induced charge electroosmosis micropumps

Joel Scott Paustian

Microfluidic technology is playing an ever-expanding role in advanced chemical and biological devices, with diverse applications including medical diagnostics, high throughput research tools, chemical or biological detection, separations, and controlled particle fabrication. Even so, local (microscale) modification of solution properties within microchannels, such as pressure, solute concentration, and voltage remains a challenge, and improved spatiotemporal control would greatly enhance the capabilities of microfluidics. This thesis demonstrates and characterizes two microfluidic tools to enhance local solution control.

I first describe a microfluidic pump that uses an electrokinetic effect, Induced-Charge Electroosmosis (ICEO), to generate pressure on-chip. In ICEO, steady flows are driven by AC fields along metal-electrolyte interfaces. I design and microfabricate a pump that exploits this effect to generate on-chip pressures. The ICEO pump is used to drive flow along a microchannel, and the pressure is measured as a function of voltage, frequency, and electrolyte composition. This

is the first demonstration of chip-scale flows driven by ICEO, which opens the possibility for ICEO pumping in self-contained microfluidic devices.

Next, I demonstrate a method to create thin local membranes between microchannels, which enables local diffusive delivery of solute. These "Hydrogel Membrane Microwindows" are made by photopolymerizing a hydrogel which serves as a local "window" for solute diffusion and electromigration between channels, but remains a barrier to flow. I demonstrate three novel experimental capabilities enabled by the hydrogel membranes: local concentration gradients, local electric currents, and rapid diffusive composition changes.

I conclude by applying the hydrogel membranes to study solvophoresis, the migration of particles in solvent gradients. Solvent gradients are present in many chemical processes, but migration of particles within these gradients is not well understood. An improved understanding would allow solvophoresis to be engineered (*e.g.* for coatings and thin film deposition) or reduced (*e.g.* in fouling processes during reactions and separations). Toward this end, I perform velocity measurements of colloidal particles at various ethanol-water concentrations and gradient strengths. The velocity was found to depend on the mole fraction via the equation $u = D_{SP} \nabla \ln X$, where u is the velocity, D_{SP} is the mobility, and X is the ethanol mole fraction.

Contents

List of Figures

List of Tables

Chapter 1

Introduction

1.1 Organization of the dissertation

I begin with a brief introduction where I motivate and review microfluidics in general (Chapter 1). Detailed background is specific to each project, and is therefore introduced along with each new topic in Chapters 2, 4, and 7. In Chapters 2-3, I describe an electrokinetic pump I have developed that uses Induced Charge Electroosmosis (ICEO) to generate on-chip pressures using AC voltages. Chapter 2 describes the concept and theory, while Chapter 3 describes the experimental demonstration. I follow this with a description of Hydrogel Membrane Microwindows (HMMs), thin photopolymerized hydrogel membranes which act as locally permeable microchannel walls. Chapter 4 describes and demonstrates the HMM

concept. Chapter 5 demonstrates the main capabilities of the HMMs for local permeability of microchannel walls. Chapter 6 describes a rapid dialysis experiment performed to study rapid diffusive solution swapping using HMMs. Chapter 7 describes diffusiophoresis and solvophoresis studies using HMMs. Chapter 8 concludes and summarizes the main findings.

1.2 Background

The rapid advance of micro/nanofabrication techniques driven by the semiconductor industry has resulted in an arsenal of tools to fabricate micro- and nanostructures. The application of these techniques to fabricate channels for fluidic control architecture has resulted in microfluidic technology [Squires and Quake, 2005, Whitesides, 2006]. Microfluidics is the study and use of fluids confined to channels of minimum dimension $\mathcal{O}$(10-100 μm). In science, microfluidics provides many advantages for studying phenomena where micrometer length scales are naturally relevant, such as in biology and soft matter. A variety of technological applications are being developed for microfluidic devices, including analytical tools, high throughput experiments, and medical diagnostics. Advantages of using microfluidics for these applications include low sample consumption, optical

accessibility, design flexibility, spatiotemporal control over samples, and unique capabilities imparted from microscale physics.

Early work in the field was focused on analytical chemistry applications ("Micro-Total Analysis Systems") [Reyes et al., 2002] and mainly used microchannels fabricated in silicon or glass, which were fabricated with semiconductor etching techniques or micromachining [Volkmuth and Austin, 1992, Wilding et al., 1994]. However, several steps of these cleanroom processes were time consuming, such as the bonding steps to seal the channels, and the materials were expensive compared to polymers. Rapid prototyping of devices into polymers such as PDMS ("Soft Lithography") allowed faster iteration between design and experiment, and was an important advance in the field [Duffy et al., 1998, Xia and Whitesides, 1998]. Soft lithography, in turn, enabled the invention of PDMS microvalves [Unger et al., 2000]. Because PDMS is a rubbery material, it can be easily deformed, which enables valving of channels containing the fluid of interest ("flow channel"). This is accomplished via pressurization of "control" channels which are made to cross above or below the flow channel [Melin and Quake, 2007]. PDMS valves enabled a new reality for microfluidics, where multi-step processes can be carried out on-chip in an automated manner (via automated pneumatics) because of local control over flow, compartmentalization, and mixing. Meanwhile, more rigid polymers have come into common use when microvalves are not required, such as

injection-molded [McCormick et al., 1997, Mair et al., 2006] or laser-etched plastic [Klank et al., 2002], or UV-curable glues [Bartolo et al., 2008]. Devices made of hydrogels are sometimes used for applications requiring dialysis [Cuchiara et al., 2010]. However, each material has different advantages and disadvantages. For this reason, methods to fabricate composite devices- that is, devices which locally incorporate multiple materials with different properties-will become increasingly important to expanding microfluidics capabilities and applications.

The intial excitement about microfluidics caused an explosion of academic research and publications, with significant effort devoted to developing proof-of-concept devices or improved means of pumping [Laser and Santiago, 2004] and mixing [Nguyen and Wu, 2005]. Given its ubiquitous presence at research institutions, microfluidics has been slower to find applications in industry and commercial products, perhaps unsurprisingly given its relative youth. As recently as 2006, a leading microfluidics figure described the state of the field: "As a field, it is a combination of unlimited promise, pimples and incomplete commitment. This is a very exciting time for the field, but we still do not know exactly what it will be when it grows up." [Whitesides, 2006].

Since this declaration, microfluidics is showing signs of emerging from this adolescent state thanks to a number of benchmark works. The first detection of a circulating tumor cell from patient blood using a microfluidic chip opens the door

to biopsy-free cancer detection [Nagrath et al., 2007]. Many recent efforts have focused on "organs-on-a-chip" [Huh et al., 2010, Zheng et al., 2012]. The goal of this subfield is to develop models for human organs and physiology, which could allow medical and pharmaceutical researchers early insight into the physiological impact of a given treatment, potentially speeding the costly drug development process. A growing number of biomolecular analysis devices are also being developed for diagnosis, *e.g.* next-generation genetic sequencing devices [Loman et al., 2012, Kim et al., 2013]. For low cost portable medical diagnostics, "Paper microfluidic" devices [Martinez et al., 2009]) offer great potential for disposable assays at dramatically reduced price and effort compared to microfabricated devices. Advanced fluid handling with pneumatic microvalves was recently demonstrated in microfabrication-free devices consisting only of tape and plastic films [Cooksey and Atencia, 2014], which could dramatically increase the capabilities of low cost devices. It seems increasingly likely that these microfluidics based technologies will have a widespread positive impact on healthcare and medical research, with continued effort, while work continues on other applications. Fundamental advances in microfluidics capabilities could impact all of these technologies and enable fundamentally new applications.

1.3 Basic microfluidic physics

Awareness of the basic physics of microscale flows [Bruus, 2007] is important for designing, performing, and understanding microfluidics experiments. The Reynolds number is typically much less than one, resulting in laminar flow profiles, such that streams can be co-flowed without significant mixing if desired. The Capillary number is often very small, so wetting properties of a device surfaces are important, and air-water interfaces can drive flows. Small pressure differences between inlets can result in large flow velocities (*e.g.* pressure ΔP $\sim$2 mm H_2O results in velocity U $\sim$100 μm/s in a 20 μm tall channel), and these flows can persist for long times because the small channel cross sections can result in low flow rates. In addition, surface physicochemical effects such as double layer forces and pH equilibria can play large, and sometimes unpredictable, role in observed behavior, and can sometimes be exploited for sample control (*e.g.* electrokinetics for pumping and separations).

1.4 Motivation

The focus of this thesis is the design, fabrication, demonstration, and characterization of "ICEO micropumps" and "Hydrogel Membrane Microwindows." Both share the goal of manipulating solutions in a local and self-contained manner

in microfluidic devices, which will enable new microfluidic applications in several ways. The detailed background and motivation varies by project, and is included when necessary throughout the thesis. The unifying theme to understand and control pressure, electric fields, and concentration fields within solutions at the microscale.

Chapter 2

Induced charge electroosmosis (ICEO) pumps: concept and theory

2.1 Motivation

Significant research continues into the development of microfluidic devices for diverse applications including medical diagnostics, high-throughput chemistry and biology, and analyte monitoring and detection [Mark et al., 2010]. Novel methods for pumping [Laser and Santiago, 2004, Iverson and Garimella, 2008] and valving [Vyawahare et al., 2008, Addae-Mensah et al., 2010, Yldrm et al., 2012] in

microchannels are helping to increase the portability of standard devices [Gervais et al., 2011, Chin et al., 2012], along with the development of capillary-driven paper devices [Martinez et al., 2009]. Nonlinear electrokinetic (EK) flows [Bazant and Squires, 2010] have been demonstrated as one class of low-volume, low-power micropumps. For example, AC electroosmotic (ACEO) [Ramos et al., 1999, Green et al., 2000, Gonzalez et al., 2000, Green et al., 2002] pumps generate high velocities on-chip (often mm/s [Urbanski et al., 2006]) with an AC field applied to an array of microelectrodes.

This chapter describes a new AC electrokinetic approach for pressure generation and fluid delivery on chip. The classic strategy for electrokinetic pressure generation [Rice and Whitehead, 1965] is adapted to be compatible with Induced-Charge Electro-Osmotic (ICEO) flows [Squires and Bazant, 2004, Bazant and Squires, 2004, Levitan et al., 2005, Squires and Bazant, 2006, Squires, 2009, Pascall and Squires, 2010b]. ICEO flows arise when an applied electric field polarizes a metal surface, inducing a non-uniform electric double layer, then drives that induced double layer into electroosmotic flow. Like conventional methods for eletrokinetic pressure generation, the ICEO strategy described here exploits the ease of driving flows electrokinetically through small pores, so that large pressures naturally arise to establish mass-conserving backflows. Specifically, an asymmetric flow is established by oriented arrays of Janus metallo-dielectric micropillars

(fig. 2.1). AC electric fields applied *across* the pumping channel drive ICEO flows *along* the channel. In so doing, higher field strengths can be achieved with a given potential difference than in DC electrokinetic flow, where electric fields must be applied along the length of a pumping channel. The proof of concept device establishes pressures comparable to standard ACEO pumps, suggesting that further optimization and enhanced fabrication methods will enable higher pressures.

The design concept and theory for the ICEO pump is described in Chapter 2. This includes a review of electrokinetic flows (Sec. 2.2.1) and electrokinetic pressure generation (Sec. 2.2.2), followed by a description of the strategy for ICEO-based pressure generation (Sec. 2.3.1). I then analyze the theoretical performance of the pump (Sec. 2.3.2), using the Lorentz Reciprocal Theorem to derive expressions for the maximum pressure $\Delta P_{\max}$ and flow rate $Q_{\max}$ to enable the rational analysis and design of such pumps. The experimental demonstration of the pump is described in Chapter 3. I describe a novel microfabrication method to fabricate arrays of electrically isolated Janus micropillars (Sec. 3.2), and the experimental setup used to measure the pressure generated (Sec. 3.3). Sec. 3.4 presents pressure results for a range of electric field strengths and frequencies, as well as electrolyte compositions. Finally, Sec. 3.5 discusses these results more broadly and suggests improvements and future research directions to optimize ICEO-based pressure generation.

2.2 Background and relevant physics

2.2.1 Electrokinetic flows

Electrokinetic (EK) flows have long been exploited to drive microscale flows [Squires and Quake, 2005]. Solid surfaces are typically charged when in contact with electrolytes, wherein a diffuse layer of ions forms to screen the surface charge. The thickness of this electric double-layer (EDL) depends on the ionic strength of the electrolyte, but typically ranges from nanometers for $\sim$ mM electrolytes to hundreds of nm for $\sim$10 μM electrolytes. An electric field applied *along* such a charged surface – *e.g.* the wall of a microchannel or capillary [Rice and Whitehead, 1965] – forces the EDL into electroosmotic flow (EOF) (fig. 2.2a), with Helmholtz-Smoluchowski velocity

$$u_{\mathrm{HS}} = \frac{\epsilon \zeta E}{\eta}. \tag{2.1}$$

Here u_{HS} is the 'slip' velocity that is driven just outside the EDL, ϵ and η are the electrolyte permittivity and viscosity, and E is the applied electric field. The potential drop across the diffuse layer, ζ, depends upon the surface charge density and electrolyte characteristics, and typically inferred from electrokinetic measurements.

The discovery of AC electroosmotic (ACEO) flow over microelectrodes [Ramos et al., 1999] inspired significant research into understanding and controlling nonlin-

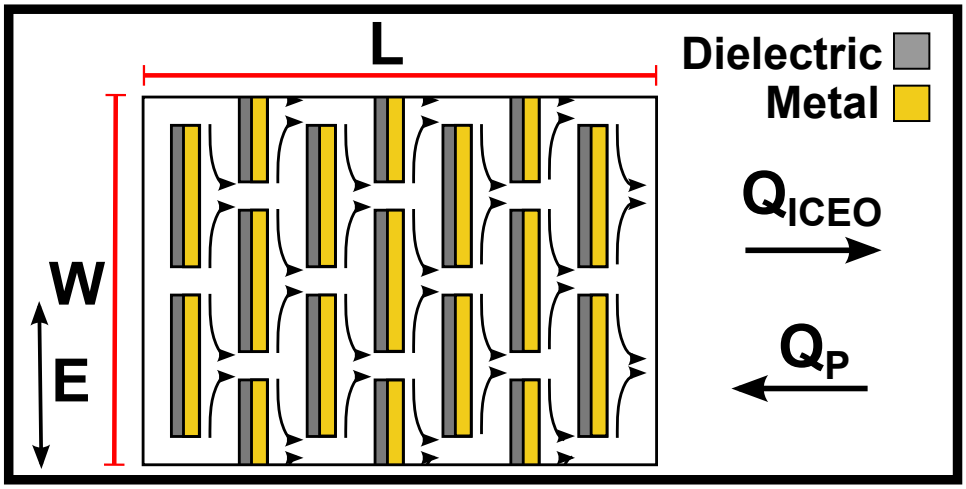

Figure 2.1: ICEO pumping using an array of width W and length L of rectangular metallo-dielectric Janus micropillars. An AC field E drives a flow Q_{ICEO} from the array. Mass conservation requires a pressure driven backflow Q_P, forcing a pressure difference along the pump.

ear EK flows [Green et al., 2000, Gonzalez et al., 2000, Green et al., 2002, Bazant and Squires, 2010]. ACEO flows occur when AC potentials are applied between closely spaced microelectrode pairs. In a particular range of frequencies, the transient EDLs that form over each electrode are driven by the transient applied fields, driving non-zero, time-averaged counter-rotating flow rolls over the electrode pair. Moreover, asymmetric electrodes break the symmetry of the rolls, driving a directed net flow [Ramos et al., 2003, Ajdari, 2000]. Interdigitated electrode arrays, both planar [Ajdari, 2000, Brown et al., 2000, Studer et al., 2004b] and three-dimensional [Bazant and Ben, 2006, Urbanski et al., 2006, Huang et al., 2009], drive strong ACEO flows and generate increased pressures. Typical velocities and

pressures in ACEO devices are ∼mm/s and 10-100 Pa, with fully optimized serpentine ACEO pumps achieving up to 1300 Pa [Huang et al., 2009]. Other nonlinear electrokinetic effects have also been explored for microscale pumping, including traveling wave electroosmotic pumps [Ramos et al., 2005] and electrothermal pumps [Gonzlez et al., 2006]. More recently, nonlinear flows due to conductivity and permittivity gradients has been explored, both in dielectric liquids [Ryu et al., 2010] and electrolytes undergoing Faradaic reactions [Ng et al., 2011] or local heating [Park and Wereley, 2013].

Induced Charge Electro-Osmosis (ICEO) [Squires and Bazant, 2004, Bazant and Squires, 2004, Levitan et al., 2005, Squires and Bazant, 2006, Squires, 2009] occurs when an electric field is applied along a polarizable (*e.g.* metal) surface. The applied electric field initially polarizes the metal, induces an electric double layer in the electrolyte (fig. 2.2b), then forces the induced double layer into induced-charge electro-osmotic flow (fig. 2.2c). Reversing the field direction also reverses the charge in the induced double layer, but the flow direction (which depends on the product of the two) is unchanged (fig. 2.2d) [Mansuripur et al., 2009, Pascall and Squires, 2010b, Pascall and Squires, 2010a]. Although ACEO and ICEO share their central physical mechanism – an electric field that induces, then forces, an EDL – in ACEO, the electric field and induced double-layer are both driven on the same structure, whereas the driving field in ICEO is estab-

lished by external electrodes, and the induced double-layer forms over electrically floating objects. The ICEO velocity obeys eq. (2.1); under an AC applied field, however, only the induced potential ($\zeta_i \sim Ea$, where a is the length of polarized surface) contributes to the time-averaged flow $\langle u_{\mathrm{ICEO}} \rangle \sim \langle E\zeta_i \rangle$ to give

$$u_{\mathrm{ICEO}} \sim \frac{\epsilon E^2 a}{\eta}. \tag{2.2}$$

Although ICEO is most easily observed over solid metal surfaces, theoretical and experimental studies have also involved more exotic surfaces [Eckstein et al., 2009, Zhao and Yang, 2011, Pascall and Squires, 2011]. Previous experiments have investigated ICEO flows near individual polarizable objects [Levitan et al., 2005, Mansuripur et al., 2009, Eckstein et al., 2009, Pascall and Squires, 2010b, Pascall and Squires, 2010a], measured the induced-charge electrophoretic velocity of metallodielectric colloids [Gangwal et al., 2008], and used conductive micropillars for ICEO-driven mixing [Harnett et al., 2008, Wu and Li, 2008]. More recently, experimental application of ICEO has focused on local flow control within microchannels, for example by using electroplated gold [Sharp et al., 2011] or carbon derived from pyrolyzed photoresist [Sugioka, 2011] to generate tall conducting structures for local ICEO flow.

Although the $u \sim E^2$ scaling holds theoretically and experimentally at small ζ, additional physico-chemical effects can reduce the ICEO velocity, in some cases by orders of magnitude. Electrode contamination reduces u_{ICEO} via dielectric

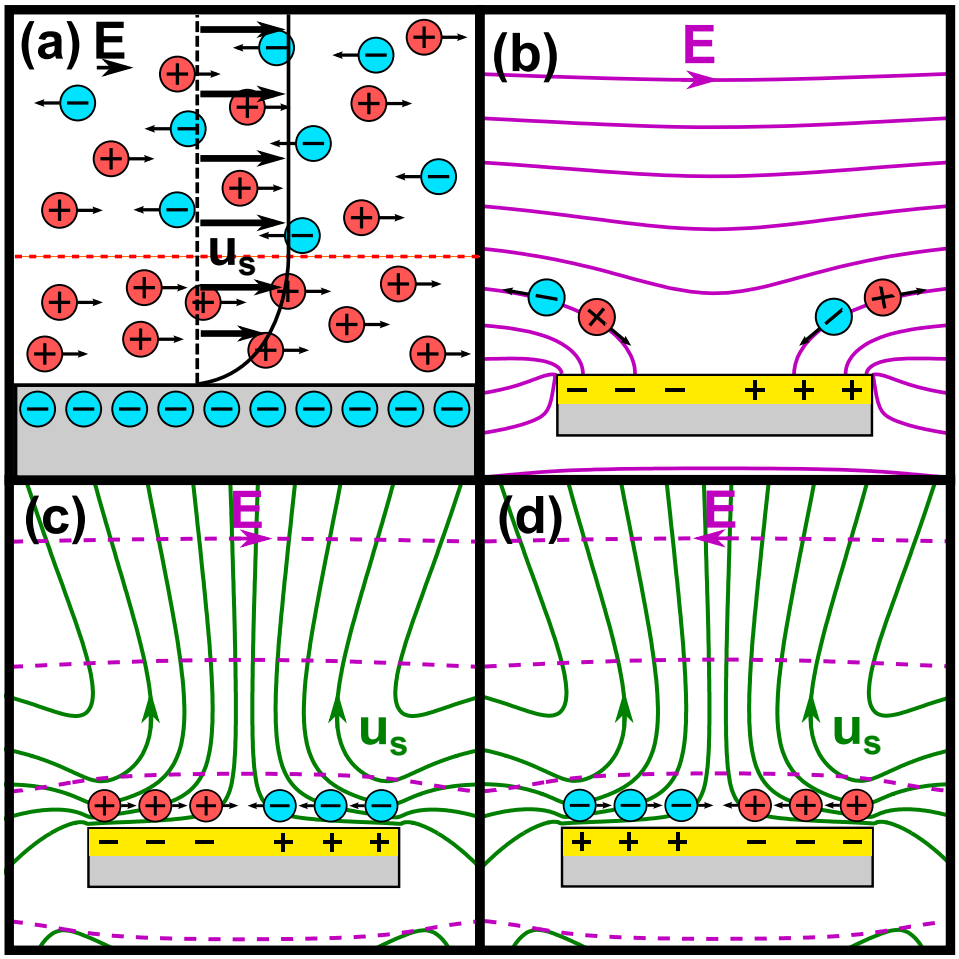

Figure 2.2: Electroosmosis and ICEO. **(a)** Electroosmotic flow occurs when an electric field is applied along a charged surface in an electrolyte, exerting a body force on the ionic screening layer. **(b)** ICEO pumping using a rectangular metallodielectric Janus micropillar. Upon application of an electric field in the electrolyte, a dipolar charge is induced on the metal surface, driving dipolar double layer formation. **(c)** After charging of the double layer, the electric field runs tangent to metal surface, driving electroosmosis perpendicular to the surface. **(d)** The same flow profile occurs upon reversal of the electric field. Steady flow is driven with an AC field. (Adapted from ref. [Pascall and Squires, 2010a]. Field lines computed with COMSOL.)

capacitance, with reductions from pH surface equilibration and ion adsorption due to "buffer capacitance" [van Hal et al., 1996, Pascall and Squires, 2010b, Pascall and Squires, 2010a]. Capacitive coupling of the floating electrode to external metal such as microscope stages can introduce stray flows [Mansuripur et al., 2009], although this effect can be eliminated by reducing the area of floating electrodes.

At larger ζ ($\zeta \gg k_B T/e$) – typical for micropumps – further physical mechanisms may suppress ICEO, even affecting the E^2 scaling in (2.2). Important factors can include concentrated ionic environments [Bazant et al., 2009a], changes in material properties such as viscosity and permittivity [Bazant et al., 2009b], and surface conduction [Khair and Squires, 2008, Khair and Squires, 2009, Messinger and Squires, 2010, Schnitzer and Yariv, 2012b, Schnitzer and Yariv, 2012a]. Surface conductivity can suppress ICEO flows near electrode edges and corners, or along surfaces with nanoscale roughness [Messinger and Squires, 2010] or nonuniform ζ [Khair and Squires, 2008]. To succinctly quantify the disagreement between observed velocity u_{expt} and theoretical velocity u_{theory}, Bazant [Bazant et al., 2009b] introduced a correction factor,

$$\Lambda = \frac{u_{\text{expt}}}{u_{\text{theory}}}. \tag{2.3}$$

which in this work is defined $u_{\text{theory}} = u_{\text{HS}}$, in order to quote measured velocities in the form

$$u_{\text{expt}} \sim \Lambda \frac{\epsilon E^2 a}{\eta}. \tag{2.4}$$

Notably, Λ may depend on E, ζ, geometry, and interfacial chemistry. Furthermore, eq. (2.2) for the ICEO slip velocity assumes a fully-charged induced EDL, an assumption that is violated at sufficiently high frequencies [Squires and Bazant, 2004, Pascall and Squires, 2010b]. Eq. 2.4, then, represents the low frequency limit, and provides a simple metric for ICEO velocity under various experimental conditions. While Λ ranges between 10^{-3} and 1 in the published literature, systems with high ζ generally show $\Lambda \ll 1$ [Bazant et al., 2009b].

2.2.2 Pressure generation using electrokinetic flows

Electroosmotic pumps exploit the ease with which EK flows can be driven through small spaces, forcing nature to establish the high pressures required to drive whatever backflow is required by mass conservation. Electrokinetic pressure generation was studied by Rice and Whitehead [Rice and Whitehead, 1965] and Morrison and Osterle [Morrison Jr and Osterle, 1965]. An electric field applied along a microchannel (or capillary) with cross-sectional area A establishes an

electroosmotic slip u_{HS}, driving a volumetric flow rate $Q_{\max}^{\mathrm{EO}}$,

$$Q_{\max}^{\mathrm{EO}} \sim u_{HS} A \sim A \frac{\epsilon E \zeta}{\eta}. \tag{2.5}$$

If the capillary is closed, mass conservation requires an equal and opposite pressure driven flow, $Q_P \sim Q_{\max}^{\mathrm{EO}}$, where Q_P is given by Poiseuille flow,

$$Q_P \sim A \frac{\Delta P s^2}{\eta L}. \tag{2.6}$$

Here L is the channel length ΔP is the pressure drop along the channel, and s is the smallest cross-sectional dimension (height or width for microchannels, radius for capillaries). Matching these two flow rates reveals the pressure that naturally builds to satisfy mass conservation,

$$\Delta P_{\max}^{EO} \sim \frac{\epsilon E \zeta L}{s^2}. \tag{2.7}$$

This $\Delta P_{\max}^{EO} \sim 1/s^2$ dependence has been exploited both to generate pressure within microfluidic channels [McKnight et al., 2001] and to create high-pressure pumps by applying electric fields through porous structures such as membranes, frits, and gels [Laser and Santiago, 2004, Yao et al., 2003, Yao and Santiago, 2003, Brask et al., 2005] (fig. 2.3a). Nanoscale pores result in high pressure pumping, with pressures from $\mathcal{O}(10 - 10^3)$ bar [Brask et al., 2005, Snyder et al., 2013]. The pressure decreases from its maximum value when electroosmotic pumps are used to drive flows through a load channel (fig. 2.3b-c). To understand the interaction between pressure and flow rate, hydraulic circuits may be used.

Hydraulic circuits allow simple flow calculations in low Reynolds number microchannels because of the linear relation between pressure and flow rate [Bruus, 2007]. These equations are valid for both standard electroosmotic pumps described above and nonlinear EK pumps [Studer et al., 2004b, Huang et al., 2009]. In both cases, the maximum obtainable pressure, $\Delta P_{\max}$, depends on the pump's internal hydraulic resistance R_P and maximum flow rate $Q_{\max}$ via

$$\Delta P_{\max} = Q_{\max} R_P. \tag{2.8}$$

The maximum ("open-circuit") pressure $\Delta P_{\max}$ is the pressure that would be established along the pump in a completely closed channel (fig. 2.3d). Electrokinetic pump pressures can therefore be increased by increasing $Q_{\max}$ (*e.g.* increasing slip velocity) or R_P (*i.e.* decreasing pore size). When the pump circuit is closed, however – *e.g.* by attaching a load with hydraulic resistance R_L (fig. 2.3e), the pressure ΔP established by the pump is generally reduced, as the flow is split between the pump and load resistances R_P and R_L, according to

$$\frac{\Delta P}{\Delta P_{\max}} = \frac{R_L}{R_L + R_P}. \tag{2.9}$$

In this case, the flow rate Q through the load is given by

$$\frac{Q}{Q_{\max}} = \frac{R_P}{R_P + R_L}. \tag{2.10}$$

Equations 2.9-2.10 enable the design of EK micropumps and interpretation of experiments. For high pressure pumping, the experiment should be designed so

that $R_L \gg R_P$ and $\Delta P \approx \Delta P_{\max}$. If $R_L \ll R_P$, the pressure drop across the pump is nearly zero and $Q \approx Q_{\max}$, analogous to an electrical "short-circuit."

The above equations assume steady-state flow rates and pressures. Long equilibration times can arise if the system is deformable, contains bubbles, or is open to external reservoirs (hydraulic capacitance, $C = dV/dP$ with volume V [Bruus, 2007, Wunderlich et al., 2010]). Such capacitances give startup transients for EK pumps which will occur as deformable walls and tubing relax, bubbles compress, and external reservoirs fill. The resulting pressure transients decay over a time scale $\tau \sim \Delta V/Q_{\max}$ with displaced volume ΔV. High pressure pumps must be designed to have adequate flow rate to overcome this effect and quickly reach steady state. In particular, pumps contained within microchannels will often have small $Q_{\max}$ due to the small channel area. To ensure pressure generation and avoid transients, small $Q_{\max}$ pumps should be mechanically isolated with valves from all sources of macroscale compliance, such as open reservoirs or bubbles.

In electrolytes, DC applied fields require Faradaic reactions to be maintained at electrode surfaces, which present an engineering hurdle in DCEO pumps by causing bubble generation, electrode dissolution, changes in electrolyte composition, and concentration polarization in the electrolyte [Strickland et al., 2010]. Several creative solutions have been developed to overcome these problems and enhance long-term pump stability [Yao et al., 2003, Brask et al., 2005, Brask

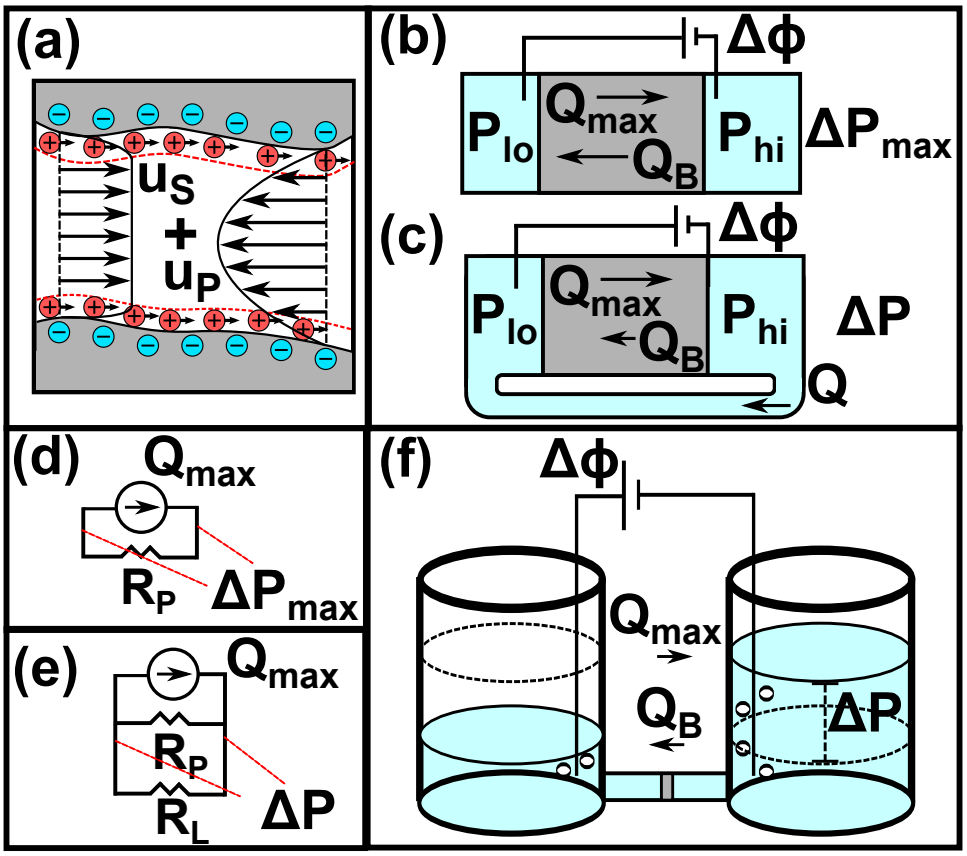

Figure 2.3: **(a)** An electric field applied through a charged porous frit results in an electroosmotic velocity u_s. An equal and opposite pressure driven backflow, u_p, superposes at steady state. **(b)** A porous frit (grey square) inside a rigid microchannel imposes an electroosmotic flow $Q_{\max}$. An equal and opposite backflow Q_B is driven by pressure $\Delta P_{\max}$. **(c)** When the pump is driving a flow Q through a load, the pressure ΔP is reduced according to 2.9. **(d-e)** Hydraulic circuit diagrams for (b) and (c) respectively. **(f)** Transients can develop, for example when microchannels are left open to external reservoirs. The left reservoir drains and the right reservoir fills unitl the pump has supplied enough volume to reach steady state, where $Q_B = Q_{\max}$. (d-e adapted from [Huang et al., 2009].)

et al., 2006]. Recently, new designs of electroosmotic pumps have continued to optimize designs for high flow rate or pressure [Gu et al., 2012] or low voltage [Shin et al., 2011, Snyder et al., 2013]. Nonlinear electrokinetic flows represent an alternative solution; the capacitive AC current used to drive such flows alleviates Faradaic reactions. However, the pressures achieved in ICEO pumps are typically orders of magnitudes smaller than those achieved with DC electroosmosis through porous structures, largely due to the limited 'pore size' s in typical ACEO systems ($\Delta P_{\max} \sim 1/s^2$) compared with the small s possible in DCEO through porous frits. Generating ICEO within anisotropically metallized arrays is meant to achieve the benefits of both approaches: small pores (s) establish a high ΔP, while AC fields alleviate Faradaic reactions.

2.3 ICEO pump

2.3.1 Design concept

Fig. 2.1a shows the design of the ICEO pump described in this work. A 'North-South' AC electric field is applied across a Janus micropillar array, whose 'Eastern' faces are metallic and 'Western' faces are dielectric. The N-S AC field drives ICEO flows on the eastern face of each pillar, which converge and push fluid eastward along the array, resulting in an ICEO driven flow rate Q_{ICEO}. If

the array were completely closed, an equal and opposite pressure-driven backflow Q_P must arise, naturally establishing a pressure drop along the pump (eqn. 2.7) which varies inversely with the squared size (s^2) of the gap between pillars. In principle, any 2D geometry could be used for ICEO pumping, as long as it provides an asymmetric ICEO flow [Squires and Bazant, 2006]. A rectangular array has straight paths between driving electrodes, maximizing the applied electric field, given a particular electrode separation.

2.3.2 Theoretical pressure and flow rate

To calculate the theoretical pump pressure and flow rate of the pump, consider a micropillar array with total length L and width W. The array can be broken into NxM unit cells (fig. 2.4a) of length $l = L/N$ and width $w = W/M$. Each unit cell has pressure drop ΔP_{cell} and flow rate Q_{cell}. The array pressure ΔP will then be the series sum, $\Delta P = N\Delta P_{\text{cell}}$, and the array flow rate Q will be the parallel sum, $Q = MQ_{\text{cell}}$. The maximum pressure and flow rate of the pump, $\Delta P_{\max}$ and $Q_{\max}$, can be calculated from the maximum pressure and flow rate of the individual unit cell using this method. The full calculation is included in Appendix A and is summarized here.

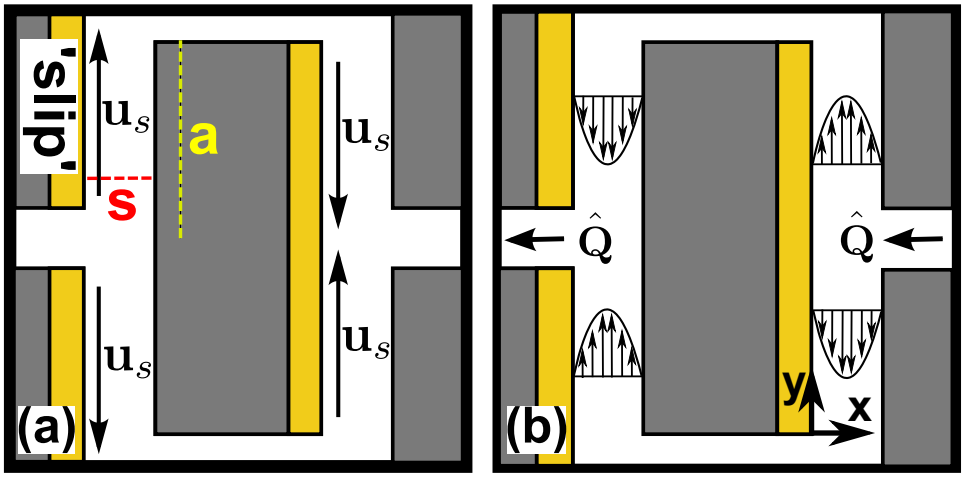

Figure 2.4: **(a)** In a closed channel, an imposed ICEO driven flow results in a pressure driven backflow. **(b)** Unit cell of the micropillar array used for reciprocal theorem analysis. The boundary condition for the unknown (ICEO driven) flow along the metal surface is given by the ICEO slip veloicty u_s. **(c)** The known flow $\hat{Q}$ is given by Poiseuille flow through a rectangular channel.)

The fluid follows the Stokes equation and incompressibility at zero Reynolds number,

$$\eta \nabla^2 \mathbf{u} = \nabla p \tag{2.11}$$

$$\nabla \cdot \mathbf{u} = 0 \tag{2.12}$$

with viscosity η, velocity field $\mathbf{u}$, and pressure p. The dielectric surfaces all exhibit a no-slip condition,

$$\mathbf{u}|_{\text{dielectric}} = \mathbf{0}. \tag{2.13}$$

By symmetry of the flow, the $y-$ and $z-$ components of the fluid velocity are zero along the North and South (top and bottom) edges of the unit cell,

$$\mathbf{u}|_{\text{North,South}} = (u_x, 0, 0), \tag{2.14}$$

and the velocity profiles at the West and East (left and right) edges of the unit cell are identical,

$$\mathbf{u}|_{\text{West}} = \mathbf{u}|_{\text{East}}. \tag{2.15}$$

However, the stress tensors at the West and East outlets vary by ΔP.

ICEO slip velocities establish "sliding wall" boundary conditions on the eastern faces of the pillars that vary along the surface,

$$\mathbf{u}|_{\text{slip}} = \mathbf{u_S}(y), \tag{2.16}$$

assuming the double layers are thin ($\lambda_D \ll s$). The slip velocity $\mathbf{u_S}$ depends upon the electric field, frequency, electrolyte composition, and surface chemistry, and can be measured experimentally, or computed analytically or numerically. This analysis holds for an arbitrary $\mathbf{u_S}$, assuming quasi-steady flow.

I now compute the flow rate Q_{cell} and pressure difference ΔP_{cell} between the West and East edges of the unit cell. The Lorentz Reciprocal Theorem [Leal, 2007, Squires, 2008] allows integrated quantities of an unknown flow (here, the ICEO driven flow, $\mathbf{u}$, fig. 2.4a) to be computed from a known reference flow, $\hat{\mathbf{u}}$,

via

$$\int \hat{\mathbf{u}} \cdot \mathbf{T} \cdot \hat{\mathbf{n}} dA = \int \mathbf{u} \cdot \hat{\mathbf{T}} \cdot \hat{\mathbf{n}} dA, \tag{2.17}$$

where $\mathbf{T}$ and $\hat{\mathbf{T}}$ are the stress tensors for the ICEO-driven and reference flows, respectively, and the integration is performed over all the surfaces A bounding the fluid.

Because the gaps are long and slender, I approximate the reference flow as fully-developed Poiseuille flow (fig. 2.4b), although the full 3D pressure driven flow could be computed if desired.

Inserting boundary conditions into Eq. (A.1) gives

$$\hat{Q}\Delta P - Q\Delta\hat{P} = 4\eta \int_{\text{slip}} u_s(y) dy \int_{\text{slip}} \left. \frac{\partial \hat{u}_y(z)}{\partial x} \right|_{x=0} dz, \tag{2.18}$$

where details of the derivation are shown in the ESI. Taking $\hat{u}_y$ to be Poiseuille flow in a rectangular channel gives an equation for the unit cell pressure and flow rate,

$$\hat{Q}\Delta P - Q\Delta\hat{P} = \frac{32 s^2 \Delta\hat{P}}{p\pi^2} f(A) \int_{\text{slip}} u_s(y) dy, \tag{2.19}$$

where

$$f(A) = \sum_{n,odd}^{\infty} \frac{A}{n^2} \left(1 - \frac{2}{An\pi} \tanh \frac{n\pi A}{2} \right) \tag{2.20}$$

and

$$A = \frac{h}{s}, \tag{2.21}$$

with unit cell perimeter p, channel height h and aspect ratio A.

The maximum flow rate for the unit cell, Q_{cell}, occurs when the unit cell has no pressure-driven backflow ($\Delta P = 0$), giving

$$Q_{\text{cell}} = \frac{16s^2}{p\pi^2} f(A) \int_{\text{slip}} u_s(y) dy. \tag{2.22}$$

By contrast, the maximum pressure ΔP_{cell} established along the unit cell occurs when the total flow rate Q through the unit cell is zero, giving

$$\Delta P_{\text{cell}} = \frac{\pi^2 \eta}{s^2} \frac{f(A)}{g(A)} \int_{\text{slip}} u_s(y) dy, \tag{2.23}$$

where

$$g(A) = \sum_{n,odd}^{\infty} \frac{A}{n^4} \left(1 - \frac{2}{n\pi A} \tanh \frac{n\pi A}{2} \right) \tag{2.24}$$

contains the geometry dependence of $\hat{Q}$.

The maximum pump pressure for an array is given by adding N cells in series, $\Delta P_{\text{max}} = N \Delta P_{\text{cell}}$, while the maximum flow rate is given by adding M cells in parallel, $Q_{\text{max}} = M Q_{\text{cell}}$, giving total pump performance

$$Q_{\text{max}} = \frac{W}{w} \frac{16s^2}{p\pi^2} f(A) \int_{\text{slip}} u_s(y) dy \tag{2.25}$$

$$\Delta P_{\text{max}} = \frac{L}{l} \frac{\pi^2 \eta}{s^2} \frac{f(A)}{g(A)} \int_{\text{slip}} u_s(y) dy, \tag{2.26}$$

for general arrays of rectangular micropillars.

In the experiments described below, I employ a pump geometry with A=1, $l = 4s$, and $w = 2.4a$, giving a maximum pressure and flow rate

$$\Delta P_{\text{max}} = 3.6 \frac{L\eta}{s^3} \int_{\text{slip}} u_s(y) dy \tag{2.27}$$

$$Q_{\max} = 0.21 \frac{W}{a} \frac{s^2}{(a+2s)} \int_{\text{slip}} u_s(y) dy \tag{2.28}$$

for the specific geometry used below. The $\Delta P_{\max} \sim 1/s^3$ scaling indicates that higher pressure can be attained by decreasing the gap width between micropillars, albeit at the expense of lower $Q_{\max}$. This scaling result holds for unit cells where the gap size s is on the same order as the cell length l, giving $N \sim L/l \sim L/s$ and $\Delta P_{\max} \sim N/s^2 \sim L/s^3$.

Proceeding further requires the quasisteady ICEO slip velocity $u_s(y)$ – which depends on the electric field, frequency, and ζ – to be specified. To derive a simple and approximate design equation, I will employ an analytical approximation which follows from a simple estimate of the local electric field. Consider an AC potential $\Delta\phi \sin \omega t$ with amplitude $\Delta\phi$ and frequency ω applied across the array, and neglect edge effects around each pillar to yield a uniform electric field $E \sin \omega t = \Delta\phi \sin \omega t / W$ along each metal surface. Using the time averaged ICEO velocity [Mansuripur et al., 2009, Pascall and Squires, 2010b] in the low frequency, small ζ limit ($\zeta \ll k_B T/e$) gives

$$\Delta P_{\max,\text{sm}} = 0.9 \frac{\Lambda \epsilon L E^2 a^2}{s^3}, \tag{2.29}$$

where Λ will depend upon many factors, as discussed in the introduction. Note that the spatially dependent Λ is effectively averaged over each micropillar. Knowl-

edge of the magnitude of Λ, however, is important for designing pumps with adequate pressure and flow rate for the desired load.

2.4 Conclusions

In this chapter I derived a design expression to calculate the maximum pressure and flow rate of the ICEO pump array. In the next chapter, I fabricate the ICEO pump and measure the pump pressure.

Chapter 3

Induced charge electroosmosis (ICEO) pumps: experiments

3.1 Introduction

In the previous chapter I described the concept and theory of an Induced-Charge Electroosmotic (ICEO) pump. In what follows, I fabricate a proof-of-concept device to show that ICEO can be used to drive non-local chip-scale flows using arrays of Janus micropillars, and measure the resulting pressure under various voltages, frequencies, and electrolyte compositions.

3.2 Device fabrication

3.2.1 Janus array fabrication

Fused silica substrates (500 μm DSP, University Wafer) were cleaned in 2:1 H_2SO_4:H_2O_2 at 120°C for 10'. A dehydration bake was performed in a convection oven for 30' at 160°C. SU-8 2015 was spun to a 10 μm thickness (500 rpm, 5"; 4700 rpm, 45"). A soft bake was then performed (65°C, 1'; 95°C, 3'; 65°C, 1'). Exposure was performed using a chrome mask (made using a DWL 200 maskwriter) and an MJB-3 aligner at 7.5 mW/cm^2 through a long pass filter (Omega Optical) for 2'15". A post exposure bake was then performed (65°C, 1'; 95°C, 4'; 65°C, 1'). The SU-8 was developed by dipping in SU-8 developer for 20", then rinsing in isopropanol. The substrate was then sprayed with SU-8 developer from a spray bottle, followed by isopropanol from a spray bottle, then repeating this procedure 3 additional times by alternating between SU-8 Developer and isopropanol spraying. The substrate was then inspected using a microscope, and if fully developed, a hard bake was performed at 160°C for 20'.

The liftoff resist (AZ5214) was patterned immediately after the hard bake. HMDS was spun at 2500 rpm for 30", followed by spin coating of AZ5214 resist (500 rpm, 5"; 2000 rpm, 30"). A soft bake was performed at 95°C for 2'. A transparency mask (CAD/Art Services) containing the liftoff mask geometry was

inserted into an MJB-3 aligner. The substrate was aligned and exposed at 7.5 mW/cm^2 for 12". The substrate was then baked at 110°C for 1', followed by a UV flood expose for 1'. The substrate was then developed for 5' using AZ726MIF developer and rinsed in DI water. The resulting photoresist liftoff mask contained a rectangular gap within the SU-8 array, as well as gaps defining the driving electrode geometry (2 cm x 300 μm electrodes connected to 5mmx5mm pads).

Just prior to performing the metal evaporation, a brief O_2 plasma clean was again performed (Technics PEIIA, 100 W/300 mTorr O_2, 2'). The electron beam evaporator (Sharon 4-pocket, single sample chamber, UCSB Nanofabrication Facility) was then loaded with the sample by setting the sample holder to a 40-42° angle with the vertical axis. The chamber was pumped to below 3x10^{-6} Torr and two evaporation steps were performed (5 nm Ti/50 nm Au, .05/.2 nm/s, no sample rotation). A gentle solvent liftoff was then performed. First, the photoresist was removed by spraying with an acetone spray bottle. The substrate was then rinsed with isopropanol. The substrate was then briefly sonicated on the lowest power setting for 10" in acetone; the sonication had to be brief and gentle to avoid SU-8 liftoff, but was necessary to liftoff the resist between the driving electrodes and array. The substrate was then rinsed with acetone again for approximately 20" while gently agitating, followed by isopropanol again for 20" under gentle ag-

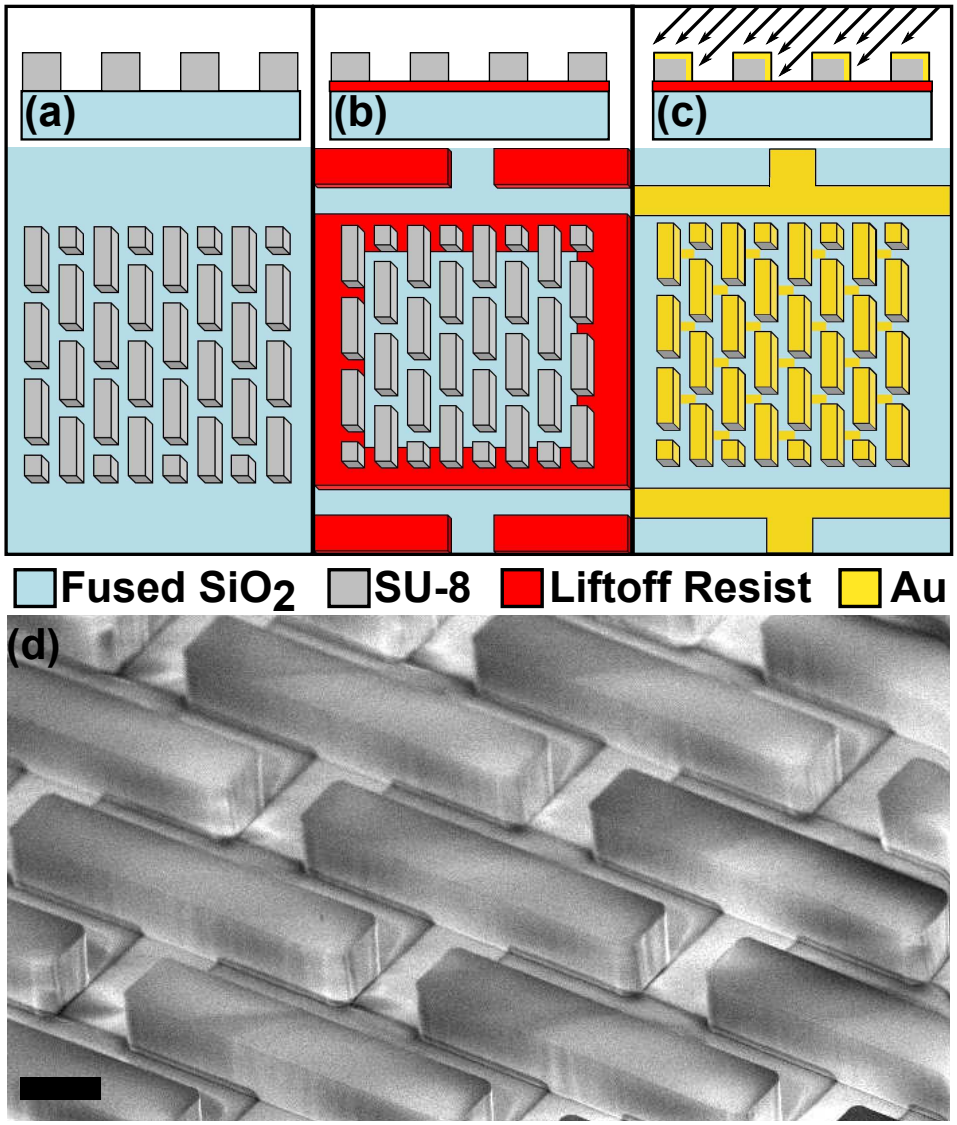

Figure 3.1: **(a)** Photolithography with SU-8 (10 μm thick) is used to pattern the array of rectangles. **(b)** A thin liftoff resist is patterned to allow evaporation windows for driving electrodes and array. **(c)** Ti/Au is evaporated at a tilt to coat half the pillar with gold and deposit driving electrodes while selectively shadowing the back side of the micropillars and the fused silica substrate between pillars.) **(d)** SEM showing micropillar array after tilted evaporation, with gold-coated side facing up. The channel floor is shadowed by the pillars except the 10 μm at the center of the pillars (Scale bar: 10 μm.)

itation. The final acetone/isopropanol rinse under gentle agitation was repeated 2 additional times.

3.2.2 Multilayer PDMS device fabrication

Multilayer PDMS molds were fabricated using standard Multilayer Soft Lithography (MSL) procedures for "push-up" valves [Studer et al., 2004a] and the geometry shown in the main text. Briefly, two separate molds were fabricated. The first (bottom layer) mold contained two photoresist coatings. A 10 μm SU-8 2015 layer was coated using the same procedure as above to define the pump and loop channel. An 18 μm layer of SU-8 2015 was patterned after this at 2000 rpm to define the 150 μm wide control channels for MSL valves. The second mold contained the 150 μm wide curved channels (top,"flow layer" or "injection layer"), which were patterned using a double coat of SPR 220-7. (1750 rpm for 45", bake at 110°C for 90", repeat the coating and bake, expose for 70", and develop for 5-10' until fully developed in 2:1 water:AZ400K) A reflow at 190°C for 2 hr resulted in 25 μm tall curved channels. The wafers were then treated with a non-stick fluorosilane vapors ((tridecafluoro-11,22-tetrahydrooctyl)-trichlorosilane, Gelest Inc, 20' in vacuum desiccator). The remaining details of the multilayer PDMS device fabrication may be found in the MSL literature.

3.3 Experimental methods

3.3.1 Microfluidic device description

The successful operation of the pump to generate ICEO flow is shown in fig. 3.2. To determine the pressure, a microfluidic pressure measurement device was designed and fabricated. The array and driving electrodes were enclosed in a microfluidic channel which was 1.82 cm x 2.0 mm, with a 4.22 cm long, 100 μm wide, 10 μm tall channel loop from front to back of the pump (fig. 3.3a-b, based upon previous experiments [Studer et al., 2004b, Huang et al., 2009]). The channel was fabricated in PDMS using Multilayer Soft Lithography (MSL)[Unger et al., 2000, Hansen et al., 2002, Liu et al., 2003] using "push-up" valves [Studer et al., 2004a, Melin and Quake, 2007], which allowed valves to be fabricated at the inlets to aid in channel filling and stray flow elimination (fig. 3.3c).

After soft lithographic patterning of the channels, the remaining device fabrication steps were performed. Holes were cut in the PDMS with a scalpel to make electrical contact to the driving electrode pads, while holes were punched with a hole puncher to the flow inlets and control channels. Just prior to use, the pump was treated with oxygen plasma for 10 minutes to aid in wetting of all surfaces within the pillar array. The pump and PDMS were then ozone treated for 5 minutes, aligned under a stereomicroscope, and bonded together by baking

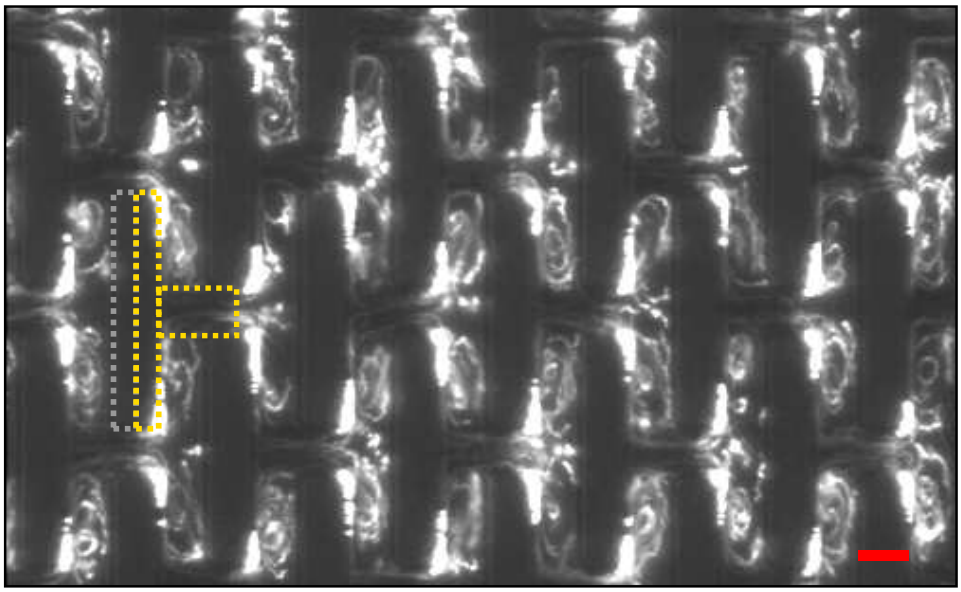

Figure 3.2: Flow profile within ICEO pump is shown using a long exposure image of fluorescent tracer particles (100 V_{pp}, 1 kHz). Dashed lines show outline of a Janus pillar and the region coated with gold. (Scale bar: 10 μm.)

at 120°C for 10'. Wires were attached to the contacts using conductive epoxy and an additional 10 minute, 120°C cure.

The array-containing channel had to be wide enough to allow alignment tolerance between the PDMS and substrate, so a 200 μm gap was left between the array and PDMS wall. For optimal pump performance, the backflow through this region had to be plugged to avoid a "short-circuit" backflow that would reduce the pump pressure. The plugged side channels had to remain permeable to electrical current. To achieve this, PEG-DA gel plugs were photopolymerized (fig. 3.3d) periodically along the side channels using Microscope Projection Pho-

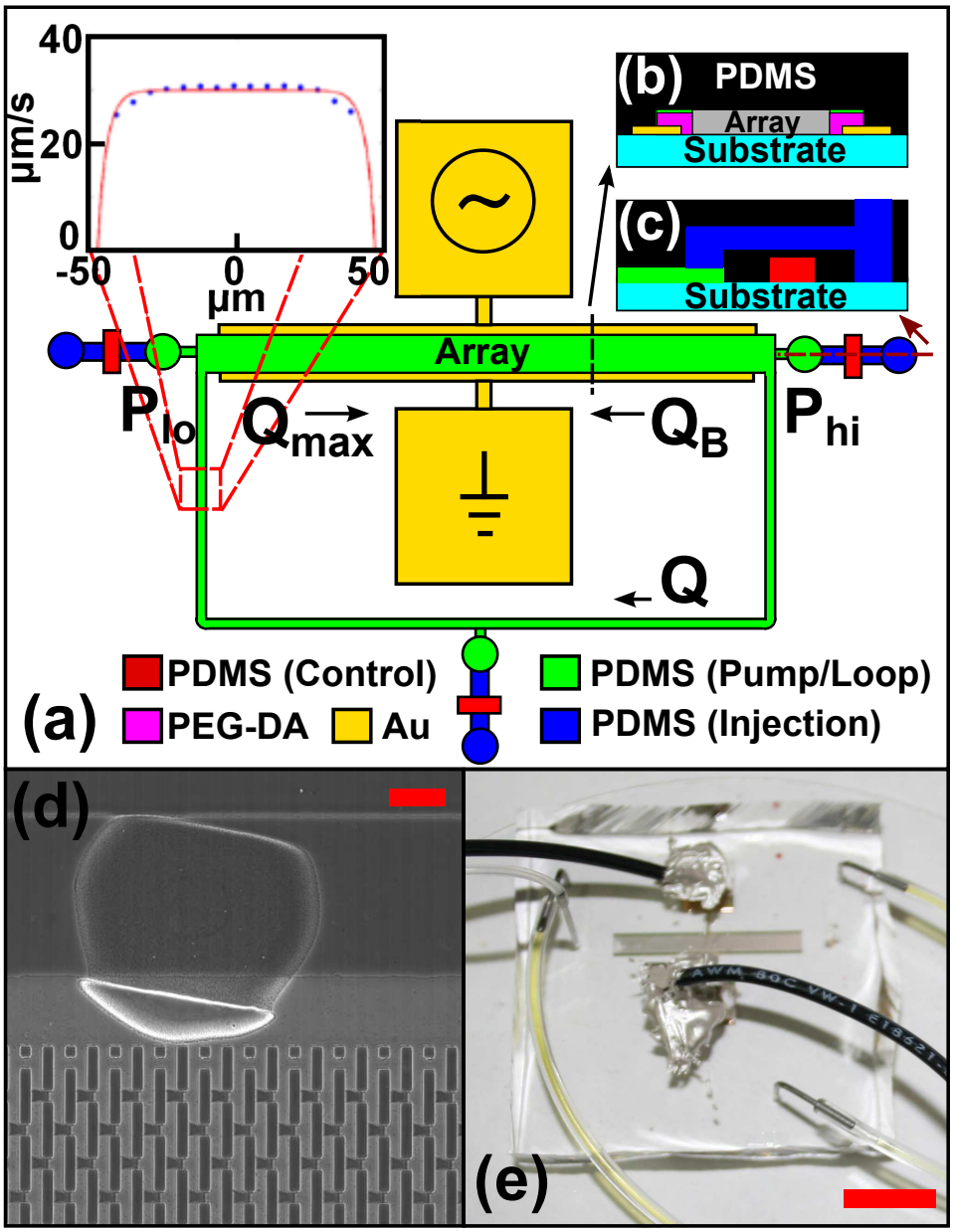

Figure 3.3: **(a)** Microfluidic channel geometry. The pressure generated by the pump was used to drive a flow in a microfluidic loop. The velocity profile in the loop was measured with PIV. PDMS valves were used to eliminate stray flows. **(b)** Side view of array region. **(c)** Side view of multilayer PDMS channels at inlets. **(d)** Electrically permeable hydrogel plugs were periodically photopolymerized along the driving electrodes to block backflow. (Scale bar: 50 μm).**(e)** Final device picture. (Scale bar: 1 cm).

tolithography [Love et al., 2001, Randall et al., 2006, Dendukuri et al., 2006, Paustian et al., 2013]. The channels were filled with a PEG-diacrylate solution (95% v/v PEG-DA, n=400, Polysciences Inc. and 5% v/v photoinitiator, 2-hydroxy-2-methylpropiophenone, Sigma Aldrich). The field diaphragm was set to 1 mm diameter and the microscope UV lamp was used to polymerize 200 μm diameter circular gel barriers approximately every 500 μm along the driving electrode by stepping the stage in 500 μm increments and exposing for 1 second to form a gel. The PEG-DA solution was then flushed from the channels. During the flushing step, the gels shifted in location due to large osmotic pressures and lack of adhesion to the untreated PDMS; however, they still blocked most of the backflow over the driving electrodes while allowing good contact with the electrolyte and a corresponding high electrical conductivity. The final device is shown in fig. 3.3e.

3.3.2 Pump testing procedure

7 100 μM electrolyte solutions were prepared, two using strong electrolytes (KCl and NaCl) and 5 using weak electrolytes (chloroacetate, acetate, MES, MOPS, and Tris). Bulk conductivity of each solution was measured using an Oakton ECTestr11+ conductivity meter. The weak electrolyte solutions contained pH buffer salt and its conjugate acid or base in equivalent concentrations. Each solution also contained fluorescent polystyrene tracers (Bangs Labs FS03F,

50x dilution, 500 nm polystyrene). Channels were loaded by flushing for at least 5 minutes at 5 psi with new solution. Removal of all bubbles was verified throughout the array and loop before commencing data collection. MSL valves were then closed by applying 8 psi of air pressure (Aro Precision Regulator PR4021-200, Grainger) to sealed water vials which were connected to the control channels.

The microscope was focused on a region near the low-pressure side of the loop using a 20x ELWD objective (Nikon, NA 0.45), and the focus was adjusted to the center of the channels. A function generator (Agilent 33220A) and amplifier (Trek PZD350 M/S) were connected to the driving electrode wires and a voltage and frequency sweep was performed (automation program described previously [Pascall and Squires, 2010a]). Voltages were applied between 100-175 V_{pp} and frequencies between 1-20 kHz. After turning on the voltage, 10 seconds were allowed to pass to reach steady state, then the flow velocity profile was measured in the loop channel by recording 5 second videos of the flow using a fluorescence camera (Andor iXon 885).

3.3.3 Data analysis

Micro-Particle Image Velocimetry (μPIV) [Santiago et al., 1998, Raffel et al., 2007] was applied to the videos to measure the velocity profile in the loop channel. First, a μPIV MATLAB algorithm was applied to the videos (64x64 pixel interro-

gation regions with 75% overlap). This resulted in a 2D depth-averaged velocity field that was uniform along the channel length y; averaging along y resulted in an experimental velocity profile that varied the channel width x, $u_y(x)$. The full 3D velocity profile $u_y(x,z)$ was related to the measured profile by a weighing function $W(z)$ [Olsen and Adrian, 2000],

$$u_y(x) = \frac{\int u_y(x,z)W(z)dz}{\int W(z)dz}. \tag{3.1}$$

The weighing function [Soni, 2008, Pascall and Squires, 2010a] is given by

$$W(z) = \left(1 + \left(\frac{3\left(z - z_{\text{foc}}\right)}{z_{\text{corr}}}\right)^2\right)^{-2}, \tag{3.2}$$

with focal plane $z_{\text{foc}} = h/2$ and depth of correlation $2z_{\text{corr}} = 10.6\mu$m in these experiments. The 3D profile obeys Poiseuille flow in a rectangular channel [Bruus, 2007],

$$u_y(x,z) = \frac{4h^2}{\pi^3\eta}\frac{\Delta P}{L_c}\sum_{n,odd}^{\infty}\frac{1}{n^3}\left(1 - \frac{\cosh\frac{n\pi x}{h}}{\cosh\frac{n\pi w}{2h}}\right)\sin\frac{n\pi z}{h}, \tag{3.3}$$

with width w, height h, length L_c, and channel domain $-w/2 \leq x \leq w/2$ and $0 \leq h \leq z$. Combining eqns. 3.1-3.3, the depth-averaged velocity profile is

$$u_y(x) = \alpha\sum_{n,odd}^{\infty}\left(\frac{1}{n^3}\left(1 - \frac{\cosh\frac{n\pi x}{h}}{\cosh\frac{n\pi w}{2h}}\right)\int_0^h \sin\frac{n\pi z}{h}w(z)dz\right), \tag{3.4}$$

where

$$\alpha = \frac{4h^2\Delta P}{\pi^3\eta L_c\int_0^h W(z)dz}. \tag{3.5}$$

The pressure was calculated by performing a least squares fit for eqn. 3.4 to find α, then calculating ΔP from α using eqn. 3.5. The maximum pressure was calculated from the experimental ΔP, along with the theoretical R_P and R_L, using eqn. 2.9, with R_L calculated from standard Poiseuille flow [Bruus, 2007] and R_P calculated using eqns. 2.8 and 2.27-2.28.

3.4 Results and Discussion

The pump pressures measured for the seven electrolytes, each with 40 different combinations of frequency-voltage (ω-ϕ), are shown in fig. 3.4a. Observed pressures varied between 15-150 Pa (1-1.5 mbar). An enhancement of 3x was observed between the lowest pressure (100 μM KCl) and highest pressure (100 μM Tris) buffers. A $\Delta P \propto \log \omega$ scaling was observed for each individual electrolyte-voltage combination (fig. 3.4a).

To calculate Λ for design purposes, fig. 3.4b shows the maximum pressure nondimensionalized by the pressure computed from the Helmholtz-Smoluchowski velocity using eqn. 2.29. The x-axis is nondimensionalized by a charging time $\tau = a\epsilon/\sigma\lambda_D$ [Squires and Bazant, 2004, Pascall and Squires, 2010b] with conductivity σ and Debye length λ_D. The correction factor Λ varies between 0.005 and 0.025

which is within the range of typical ICEO velocities over bare metal surfaces [Bazant et al., 2009b].

When $\zeta \ll k_B T/e$ (where the thermal voltage $\zeta_T = k_B T/e = 25$ mV for 1:1 electrolytes), the EDL charging time can be calculated using an RC time, with resistance $R = a/\sigma$ and capacitance $C = \epsilon/\lambda_D$. When $\zeta \gg \zeta_T$, the double layer capacitance C diverges according to Gouy-Chapman theory [Squires and Bazant, 2004],

$$C = \frac{\partial q}{\partial \phi} \sim \cosh \frac{\zeta}{2\zeta_T}. \tag{3.6}$$

Equation 3.6 implies that the double layer may not be fully charged in the high-ζ experiments shown here. A charge balance on the double layer in the high frequency limit ($\tau\omega \gg 1$) with small surface conduction (Dukhin number $\mathrm{Du} \ll 1$) gives

$$\frac{\partial q}{\partial t} = j_\perp = \sigma E_\perp \sin \omega t, \tag{3.7}$$

with perpendicular current $j_\perp$ and field amplitude $E_\perp$. The time averaged induced charge in the double layer is then

$$\langle |q| \rangle = \frac{\sigma E_\perp}{\omega}. \tag{3.8}$$

When $\zeta \gg \zeta_T$, the nonlinear Poisson-Boltzmann equation predicts

$$\frac{q}{q_0} = \sinh \frac{\zeta}{2\zeta_T} \approx \frac{e^{\zeta/2\zeta_T}}{2}, \tag{3.9}$$

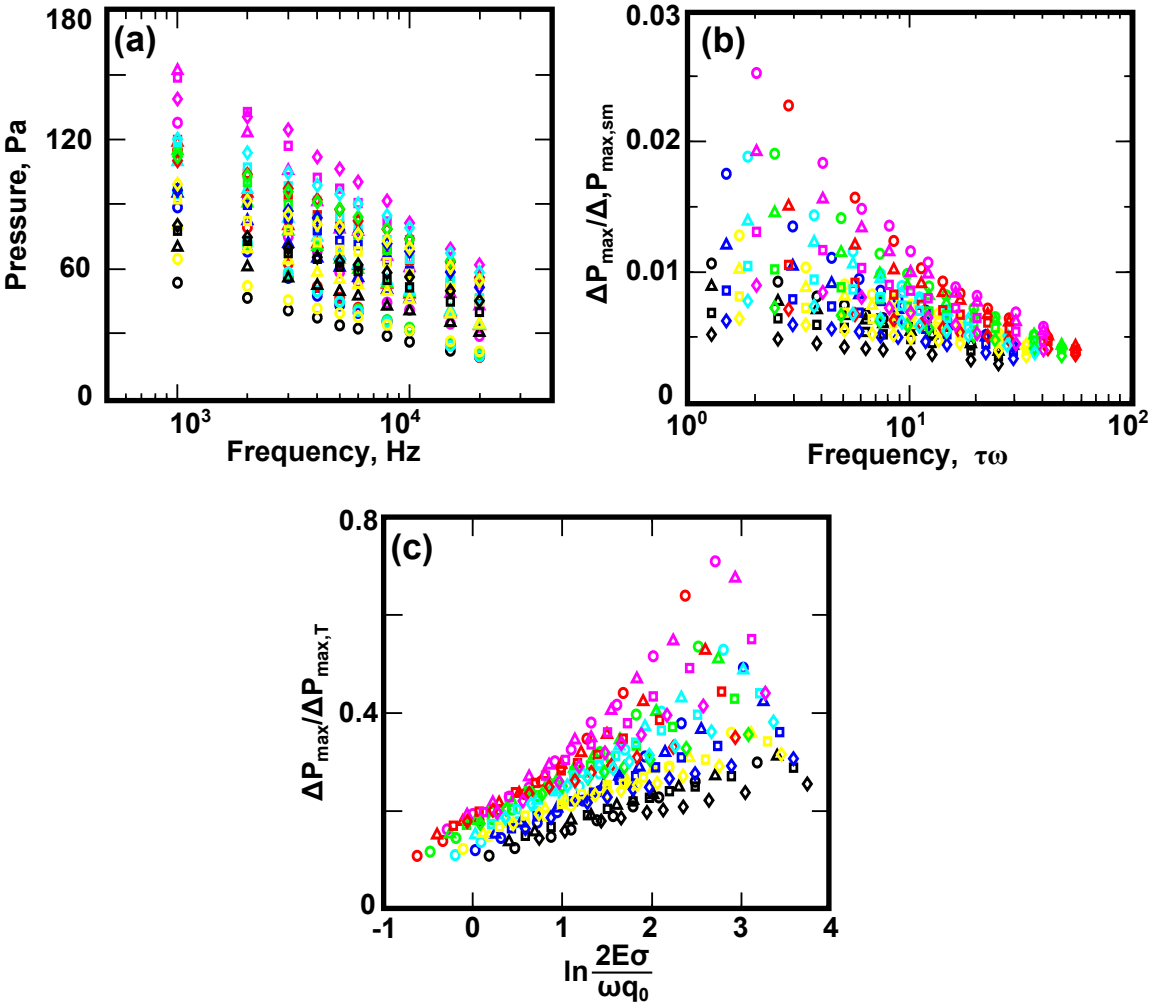

Figure 3.4: ICEO pump pressure. **(a)** Pressure was measured for 10 frequencies between 1-20 kHz, 4 voltages between 100-175 V_{pp} (100 V_{pp}, circles; 125 V_{pp}, triangles; 150 V_{pp}, squares; 175 V_{pp}, diamonds) and 7 electrolytes (KCl, black; NaCl, blue; Chloroacetate, pKa 2.9, yellow; Acetate, pKa 4.8, cyan; MES, pKa 6.2, green; MOPS, pKa 7.2, red; Tris, pKa 8.3, magenta). **(b)** Pressure naively nondimensionalized by theoretical maximum pressure computed using Helmholtz-Smoluchowski velocity and charging time. The y-axis also corresponds to the correction factor Λ. **(c)** Nondimensional pressure plotted against ζ using scaling factors derived in text.

where $q_0 = \sqrt{8\epsilon k_B T n_0}$ with salt concentration n_0. Combining eqns. 3.8 and 3.9 when $\zeta \gg \zeta_T$ gives [Olesen et al., 2006, Hjgaard Olesen et al., 2010]

$$\frac{\zeta}{\zeta_T} \sim \ln \frac{2E_\perp \sigma}{\omega q_0} \tag{3.10}$$

and

$$u \sim \Lambda \frac{\epsilon E_\parallel \zeta_T}{\eta} \ln \frac{2E_\perp \sigma}{q_0 \omega}, \tag{3.11}$$

with parallel electric field $E_\parallel$. The correction factor Λ depends upon surface chemistry [Pascall and Squires, 2010b] through the buffer capacitance and Stern layer, and is therefore expected to change for different electrolytes. The scaing of $\Delta P_{\max}$ can be obtained (eqn. 2.27),

$$\Delta P_{\max} \sim \Lambda \frac{\epsilon E_\parallel \zeta_T La}{s^3} \ln \frac{2E_\perp \sigma}{q_0 \omega}. \tag{3.12}$$

A full description would require precise computation of $E_\parallel$ and $E_\perp$, but both scale with E, such that the pressure scaling is

$$\frac{\Delta P_{\max}}{\Delta P_{\max,T}} \sim \Lambda \ln \frac{2E\sigma}{\omega q_0}, \tag{3.13}$$

where

$$\Delta P_{\max,\mathrm{T}} = \frac{\epsilon E \zeta_T La}{s^3} \tag{3.14}$$

At lower frequencies (larger E/ω, $\tau\omega \lesssim 1$) this scaling becomes invalid because the charge balance used to derive it is no longer valid.

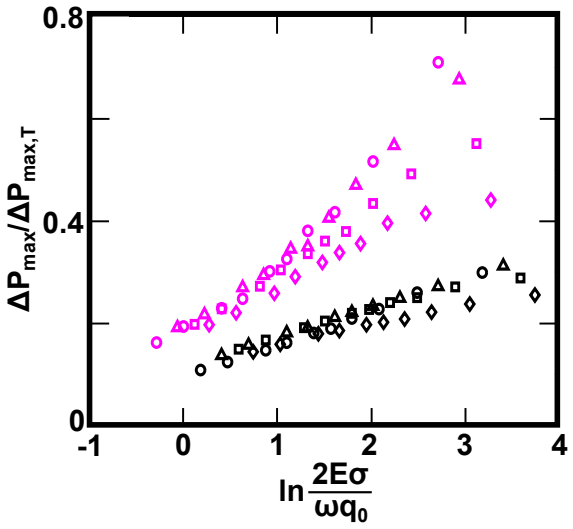

Figure 3.5: Replot of highest and lowest pressure data from fig. 3.4. The data collapses for different applied voltages and frequencies at low ζ and becomes linear. At high ζ the data no longer collapses.(100 V_{pp}, circles; 125 V_{pp}, triangles; 150 V_{pp}, squares; 175 V_{pp}, diamonds. KCl, black; Tris, magenta.)

The data is plotted with this voltage and frequency in fig. 3.4c. Indeed the data collapses by voltage at low ζ, and the data initially follows a linear trend, as predicted by this scaling. The slopes also differ between electrolytes, which suggests an electrolyte-dependent Λ. However, at higher ζ, the pressure increases either nonlinearly or with a different slope, and the voltages no longer collapse, indicating the scaling is no longer valid. This could be due to high-ζ nonlinear effects, as well as a fully charged double layer at lower frequencies. The lowest and highest pressure electrolytes are shown in fig. 3.5 to demonstrate the trends more clearly.

3.5 Conclusions

In the previous two chapters, I explained the design, fabrication, and testing of a microfluidic pump that uses ICEO to generate chip-scale flows and pressure. The pump successfully drove chip-scale flows in standard microfluidic channels using an AC voltage, validating the central design idea for pressure generation.

The design expressions (eqns. 2.27-2.29) suggest several routes to optimize the pump pressure and flow rate. Higher pressures can be achieved by decreasing s, the gap spacing within the pump (*e.g.* increasing the aspect ratio $A = h/s$). Several challenges would be faced in applying this strategy to the fabrication method presented here. Smaller evaporation angles are required as aspect ratio increases, which can cause nonuniform angle and shadowing across large samples ($L \sim$ cm). Conversely, fixing the aspect ratio ($A = 1$) and decreasing s lowers the maximum flow rate $Q_{\max}$ (eqn. 2.28). Flow rates must be maintained at a high enough level to avoid slow response to compliances, causing "short-circuit" performance. Further optimization of ICEO pumps may be possible using the fabrication method presented here, but these issues would need to be overcome or minimized.

Alternatively, an entirely new fabrication method could be developed to fabricate high-A, small-s Janus micropillar arrays, which would increase both the

pressure and flow rate by eqns. 2.25-2.26. Others have successfully demonstrated local ICEO flows using high aspect ratio conducting micropillars, for example via Bosch etching [Harnett et al., 2008], electroplating [Sharp et al., 2011], or C-MEMS [Sugioka, 2011]. I also demonstrate the use of silicon micropillars for ICEO flow in Appendix B. These methods could potentially be used to create ICEO pumps by fabricating asymmetric shapes, which can be designed to exert a net ICEO flow [Squires and Bazant, 2006], eliminating the need for Janus micropillars. Closer spacing between pillars would be a necessity, which would require further fabrication process development. Alternatively, high-A Janus micropillars could be achievable via other enhanced fabrication methods, either by asymmetrically coating (*e.g.* improved tilted evaporation methods), or removing (*e.g.* tilted ion milling [Harnett et al., 2008]) thin metal films.

Less fabrication-intensive routes to enhance pump performance could also be explored. For example, numerical simulations could be applied to optimize the pump geometry (*i.e.* as in [Gregersen et al., 2009] but optimized for pressure). Surface chemistry could also be further optimized by exploring more electrolytes, surface functionalizations and coatings, and electrode materials [Pascall, 2010].

The central design idea of the pump was to generate AC-driven electrokinetic flows within "porous" channel structures in order to increase R_P (and $\Delta P_{\max}$) of the pump. The same strategy could be applied to increase the pressure of other

nonlinear electrokinetic pumps (*e.g.* creating electrokinetic "slip" flow within sidewall-coated micropillar arrays). Continued improvements of $\Delta P_{\max}$ in nonlinear electrokinetic pumps could allow their use for high-load applications, *e.g.* HPLC-on-a-chip [Eijkel, 2007].

Chapter 4

Hydrogel membrane microwindows (HMMs): concept and fabrication

4.1 Motivation and strategy

Provoking the response of cells, organisms, solutions, and materials to environmental changes is a nearly ubiquitous demand in biology, chemistry, physics, and materials science. Microfluidic devices enable such studies to be performed

This chapter is adapted from from Paustian *et al.*, *Physical Review X* 3 041010 (2013). http://dx.doi.org/10.1103/PhysRevX.3.041010.

on micron scales [Meyvantsson and Beebe, 2008, Wheeler et al., 2003, Crane et al., 2010, Dittrich and Manz, 2006, Park et al., 2010], with precise geometric and fluidic control over small sample volumes [Squires and Quake, 2005, Whitesides, 2006]. Techniques for microfluidic logic [Thorsen et al., 2002] have enabled large-scale integration of microfluidic devices capable of complex experiments and high-throughput parameter sweeps [Melin and Quake, 2007]. Robust and versatile methods for manipulating local microscale chemical environments in space and time, however, have remained elusive.

The vertebrate circulatory system provides an ideal model for the rapid and precise chemical delivery to soft targets, by using a stepwise method of convection followed by diffusion. Gas, nutrients, and other solutes are convected rapidly over large distances through arteries and vessels until they reach smaller capillaries, which are distributed densely enough (spacing $\mathcal{O}(100\ \mu\text{m})$) that solute can diffuse rapidly across membranes or pores and into tissues and cells.

This chapter describes a powerful, versatile, yet simple element for microfluidic systems – Hydrogel Microwindow Membranes (HMMs) – that enable an analogous stepwise convection-diffusion chemical delivery in microfluidic systems. HMMs provide an unparalleled combination of rapid delivery, spatial control, optical accessibility, integration with standard devices, and ease/speed of device fabrication. HMMs are compatible with existing microfluidic materials and fabrication

techniques, and enable the rapid imposition and switching of *local* microchemical environments, without introducing convective flows near the sample that might disrupt or wash away fragile or unbound materials.

The core HMM strategy is illustrated in figures 4.1 and 4.2. A 'reservoir channel' (which will contain the solution to be delivered) is made to run alongside a 'sample' channel (to which the solution will be delivered), with a gap in the wall separating them. A thin ($10-25\mu m$ wide) hydrogel membrane microwindow placed into this gap then allows local micro-dialysis. Its pores are small enough that it acts like an impermeable wall from the standpoint of fluid flow, yet is permeable to electric fields, solute, and solvent. Flowing a solution through the reservoir channel establishes and maintains a steady reservoir of solute, which subsequently diffuses through the membrane and into the sample channel. The thinness of the membrane, and the small dimensions characteristic of microfluidic devices, renders a short time scale for diffusive delivery ($\tau_D \sim L^2/D$). Dissolved salts ($D \sim 10^3 \mu\text{m}^2/\text{s}$), for example, require $\sim$ 100ms to diffuse $\sim 10\mu$m, and ~ 10 s to diffuse 100 μm.

Several essential features should be noted. (1) Hydrogel membrane microwindows (HMMs) are exceptionally thin, which enables fast diffusive delivery. (2) Devices can be designed with multiple membranes, each with a distinct, independently-controlled reservoir channel. Complex solution micro-environments can thus be

designed into microfluidic systems, *e.g.* with multiple components, introduced at multiple locations and/or times, as well as sharp concentration gradients (*e.g.* several Molar over tens of μm). (3) HMMs are permeable to electric fields, enabling localized electrokinetic effects (*e.g.* selective electroporation, electrophoresis, sorting, and separations) to be incorporated into complex microfluidic devices. (4) Integration with microfluidic plumbing and logic (including elastomeric valves in PDMS devices [Unger et al., 2000]) enables rapid switching of reservoir solutions, and consequently, of the local solution chemistry within the sample chamber. (5) HMMs hydrodynamically isolate reservoir and sample channels in complex device geometries, without requiring pressures to balance as in laminar flow strategies. Each HMM can thus operate independently, without interfering with upstream or downstream HMMs. (6) The fabrication strategy is relatively simple, and uses little more than standard microscopy equipment. (7) HMMs do not interfere with optical access to the sample, whereas *e.g.* track-etched membranes used to introduce solute to a channel from above or below [Morel et al., 2012] interfere with the optical path. Instead, sample and reservoir channels can lie entirely within a single focal plane, allowing high-resolution gradient visualization within microscale regions, and improved synchronization with reservoir channel flow switching. Hydrogel micro-window membranes can be integrated into conventional microfluidic channel materials, and hydrogel chemistries can be readily adapted as needed for

particular chemical demands, *e.g.* to be permeable to a range of solutes and solvents. HMMs enable a broad range of capabilities for microfluidic studies and applications that demand precise spatial and temporal control over solute and solvent distribution.

The chapter begins with a brief discussion of existing techniques for microfluidic solution manipulation in Section 4.2, then describes the HMM fabrication procedure in Section 4.3. Section 4.4 presents the basic operation and properties of HMMs, showing HMM function for flow-free introduction of solute (pH buffers, evidenced with a fluorescent pH indicator, fig. 4.2) and solvent (triggering local antisolvent crystallization, fig. 4.3). Later chapters demonstrate novel solution control capabilities of the HMMs (local electric permeability, local concentration gradients, and rapid dialysis).

4.2 Background

4.2.1 Diffusive delivery in microfluidic devices

Steady chemical gradients have been created convectively, by using T-junctions [Kamholz et al., 1999] to bring two solutions into co-flowing contact. These can be used to expose surface-fixed samples to chemical gradients or dynamic environments [Hersen et al., 2008, Ahmed et al., 2013], but resulting shear may disrupt or

perturb soft samples (*e.g.* cells or tissues, soft materials, or growing crystals), and flow itself may displace unbound samples (including material precursors, existing solutions, particles or cells) or disrupt gradients. Although shear may be reduced using channel networks for gradient generation [Jeon et al., 2000], all flow-based strategies require precise pressure balances to properly align flows [Choi et al., 2012b], as well as relatively large device areas [VanDersarl et al., 2011], and therefore become increasingly impractical as devices become more complex. Co-flowing techniques are well-suited for certain experiments, but do not represent a versatile, robust technique to rapidly introduce, controllably vary, or precisely modify local chemical micro-environments. Convective solution modification has also been achieved by adding ingredients sequentially, via a rotary mixer [Chou et al., 2001], enabling automated batch preparation of solutions [Hansen et al., 2004], yet each added aliquot necessarily flushes out an equal volume of the existing sample. In some cases, this flushing is advantageous – *e.g.* in maintaining a stable microbial population in a micro-chemostat [Balagadde et al., 2005] – but continuous dilution is undesirable in other experiments.

Introducing solute or solvent diffusively can alleviate some of the issues associated with flow, but poses separate challenges. Diffusive transport becomes prohibitively slow over long distances: the time τ_D for a species with diffusivity D to diffuse a distance L scales like $\tau_D \sim L^2/D$, and any flow U – stray

or otherwise – overwhelms this diffusive delivery beyond a critical length scale $L_c \sim D/U$. Batch diffusive mixing has been enabled through free-interface diffusion, initiated by opening PDMS valves between microchambers [Hansen and Quake, 2003, Hansen et al., 2006, Perry et al., 2009, Streets and Quake, 2010] or sliding lubricated substrates to bring loaded microchambers on opposite sides into contact [Du et al., 2009, Li and Ismagilov, 2010, Li et al., 2009]. Such strategies, however, cannot maintain steady gradients. Steady gradients have been produced by controllably contacting flowing source/sink solutions with large ($L \sim 1mm$, $\tau_D \gtrsim 1000s$) flow-free channels [Frank and Tay, 2013] or chambers [Atencia et al., 2009], but reductions in chamber size (and τ_D) would result in increased stray convection.

Many methods for embedding or fabricating membranes within microchannels have been proposed to allow diffusive solute delivery [De Jong et al., 2006, Keenan and Folch, 2007]. Membrane fabrication has been achieved via interfacial polymerization [Kim and Beebe, 2008] and evaporative assembly of packed beds [Choi et al., 2012a]. Embedding opaque track-etched membranes between multiple microchannel layers [Kuo et al., 2003, VanDersarl et al., 2011, Morel et al., 2012, Kim et al., 2012] allows precise control of pore size and visualization of the bottom channel layer, but their opacity prevents high quality microscopy of all microchannel layers. Devices made entirely of solute-permeable materials [Cheng et al.,

2007, Cuchiara et al., 2010, Palacci et al., 2010, Palacci et al., 2012] allow diffusive delivery along entire channels. Previous works have not, however, demonstrated the *rapid* ($\tau_D \sim$ seconds) and *localized* (L$\sim$ 20 μm) flow-free solution swapping and strong gradient generation afforded by HMMs, which exploit the rapid diffusive equilibration across thin, high-porosity hydrogel membranes.

4.2.2 Photopolymerization in microfluidic channels

Contact photolithography is most commonly used to photopolymerize hydrogels [Beebe et al., 2000], which has been used to create permeable plugs or microchamber walls [Zhan et al., 2002, Seong et al., 2002, Herr and Singh, 2004, Tan et al., 2010, Tentori and Herr, 2011]. At standard substrate thicknesses (0.5-1 mm), contact lithography exhibits limited resolution [Song et al., 2004b] due to the propagation of diffraction through the substrate, resulting in larger membrane size and diffusive equilibration times. This problem can be overcome by using extremely thin substrates (as in [Beebe et al., 2000]), however these are often prone to fracture. Projection lithography has also been used by projecting shaped laser beams into microchannels, which requires custom optics setups [Song et al., 2004b, Song et al., 2004a, Hatch et al., 2006].

Another method of projection lithography has recently come into common use in microfluidics: Microscope Projecton Photolithography (MPP) [Love et al.,

2001], in which a standard microscope provides high resolution photopatterning with UV illumination. In MPP, a photomask is placed within the field conjugate plane, usually in the microscope's field diaphragm, yielding patterned UV illumination in the focal plane. The photomask pattern is also magnified by the objective, resulting in enhanced resolution. The technique has recently become common for flow lithography, wherein hydrogel paticles are synthesized within flowing solutions of UV-curable molecules through polydimethylsiloxane (PDMS) channels [Dendukuri et al., 2005, Dendukuri et al., 2006, Dendukuri et al., 2007, Panda et al., 2008, Shepherd et al., 2008, Helgeson et al., 2011]. The polymerization reaction is inhibited by oxygen that permeates through the PDMS walls, resulting in freely flowing hydrogel particles [Dendukuri et al., 2008]. MPP has also been used to pattern 150 μm wide gel barriers [Randall et al., 2006] and hydrogel posts [Liu et al., 2009] on glass surfaces in glass/PDMS channels.

4.3 Fabrication method

4.3.1 Device fabrication

Here I describe a method to fabricate hydrogel membranes that are much thinner than would be possible using standard methods such as contact lithography, by using MPP to locally polymerize UV-reactive solutions (fig. 4.1). As with

flow lithography, poly(ethylene glycol) diacrylate (PEG-DA) was chosen as the polymer precursor, which can be photopolymerized via a free radical polymerization mechanism [Dendukuri et al., 2008]. Since this reaction is known to be oxygen inhibited [Dendukuri et al., 2006], I chose "microfluidic sticker" channels made of NOA-81 (Norland Optical Adhesives 81, Edmund Optics), a thiol-ene based polymer [Bartolo et al., 2008] which is impermeable to oxygen and can be rapidly templated. NOA-81 channels also have low compliance, which prevents walls from deforming and causing leakage around HMMs, and can be covalently bonded to acrylates [Hoyle and Bowman, 2010], which aids adhesion. A disadvantage of NOA-81 compared to PDMS is that microvalves cannot be directly fabricated into channels; however, this is unnecessary in many experiments. If microvalves are needed, PDMS channels can be bonded atop NOA-81, enabling integrated microvalves and HMMs for precise flow control and rapid switching (see Chapter 6).

Microfluidic stickers were prepared using a procedure similar to the literature procedure [Bartolo et al., 2008]. 10 μm tall PDMS molds were prepared in the inverse shape of the desired channel using standard soft lithography methods [Xia and Whitesides, 1998]. NOA-81 glue was dropped onto a flat PDMS piece and any bubbles in the glue were removed with a syringe. The PDMS mold was placed on top of the glue to form a PDMS sandwich. The NOA-81 was then irradiated with

a 365 nm UV lamp (5 mW/cm^2) for 90 sec. The PDMS mold was carefully peeled off and the sticker was transferred onto a cleaned glass microscope slide. The flat PDMS was firmly pressed across its surface to bring the sticker into contact with the glass. The flat PDMS was removed and the device was irradiated for an additional 3 min. 600 μm diameter holes were cut at the sticker channel inlets using a hole puncher (Syneo Inc). To make leak-free low-volume ports, small "PDMS inlets" ($\sim$5mm cubic PDMS pieces with 600 μm holes) were bonded to the sticker inlets by placing PDMS and NOA-81 device in an ozone chamber for 5', aligning under a stereomicroscope, and baking at 120°C for 10'.

4.3.2 Hydrogel photopolymerization method

After inserting the photomask in the microscope field stop, the UV light shutter was opened, and light appeared as a blue fluorescent rectangle on the NOA-81. The UV shutter was opened only for short periods (less than 30 sec.) to avoid heat damage to the photomask. The device and fluorescence camera were rotated until they were rotationally aligned with the light. The camera software enabled marking of rectangular regions with an adjustable box; this "alignment box" was used to mark the location of the light on screen. Alternatively, without such software, an alignment box could be made by taping paper or a transparency sheet to the computer monitor. Once the light had been aligned to the alignment

box, the shutter could be closed and the stage could be translated freely during channel filling, and re-aligned later to the alignment box simply by translating the stage.

Immediately after bubbling compressed air through the precursor for 10 min., the solution was agitated for 10 seconds to redistribute silica tracers, then injected into the NOA-81 channels using a syringe. Solution was injected only until the NOA-81 layer had been filled; extra precursor injection was minimized to avoid unequal buildup of precursor in the inlets, and resulting stray pressure driven flows. After the NOA-81 layer had been filled, the desired crosslinking region was translationally aligned to the alignment box. Silica tracers were viewed under phase contrast. Flow was minimized by adjusting the syringe pressure, and the UV exposure was performed while viewing the tracers to ensure flow remained slow.

After crosslinking the HMM, channel flushing had to be quickly performed to avoid excess crosslinking of the PEG-DA solution near the HMM. This would happen if solution was allowed to remain quiescent for more than several minutes after crosslinking. If excess crosslinking occurred, the PEG-DA solution would gel throughout the channel width, clogging the device. This problem could be easily prevented by flushing each channel within several minutes of crosslinking, either with fresh PEG-DA solution or working solutions for the next experiment.

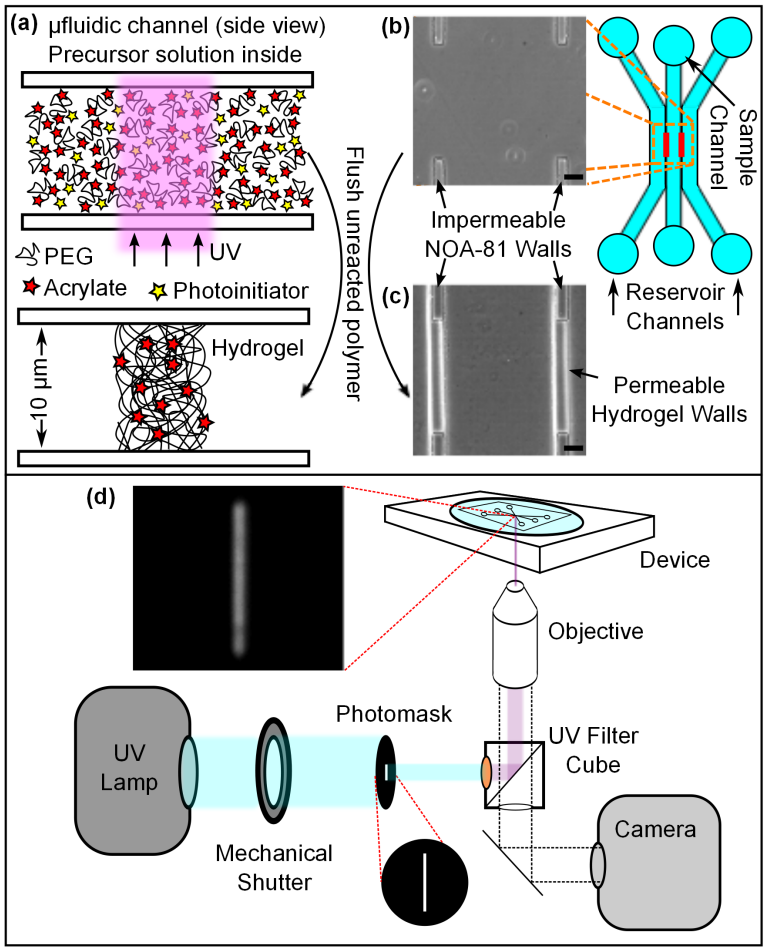

Figure 4.1: Fabrication of hydrogel microwindow membranes (HMMs). **(a)** A UV-polymerizable solution of poly(ethylene glycol)-diacrylate and photoinitiator initially fills a 3-channel microfludic device **(b)**, with gaps in the walls between channels. Patterned UV light is used to crosslink the hydrogel in two specified rectangular regions (width: 10-20 μm) filling the gaps in the walls. **(c)** After flushing the unreacted solution, hydrogel microwindow membranes remain (phase contrast, scale bar=20 μm.) **(d)** Simplified microscope schematic for fabricating HMMs. The microfluidic device is placed on the microscope stage, and photomask inserted into the microscope field aperture. A computer controlled mechanical shutter exposes the PEG-DA solution to UV irradiation for the desired exposure time. Inset: Natural fluorescence of NOA-81 optical glue enables the patterned UV light to be aligned. Credit: Rodrigo Nery Azevedo and Sean B. Thomas-Lundin for photomask design and aiding photopolymerization procedure development.

4.4 Operation and demonstrations of diffusive delivery

4.4.1 Visualization of pH buffer diffusion

For HMMs to function appropriately, they must be permeable to the diffusive transport of solute and solvent, yet concurrently act as rigid, impermeable walls from the standpoint of fluid flow. These twin demands require a hydrogel that is chemically inert, with pores that are large enough to admit molecular diffusion, yet small enough to prevent appreciable flow.

Fig. 4.2 demonstrates the successful operation of HMMs. Each of the three channels contains 25 μM fluorescein, which functions as a pH-indicator due to its increasing fluorescence intensity between pH 5-9. Solutions buffered at different pH are driven through the three channels: the left (reservoir) channel is maintained at pH 8.1 by a 10 mM tris buffer and appears bright, the right (reservoir) is held at pH 4.7 by 10 mM acetate buffer and appears dark, and the center (sample) channel is held at pH 6.3 by 1 mM MES buffer along with 9 mM KCl to balance ionic strength, and appears grey. 0.02 wt% 500nm fluorescent polystyrene beads are added to the sample channel as flow tracers (Bangs Labs FS03F). All channel outlets were connected to a waste reservoir, the two reservoir channel inlets

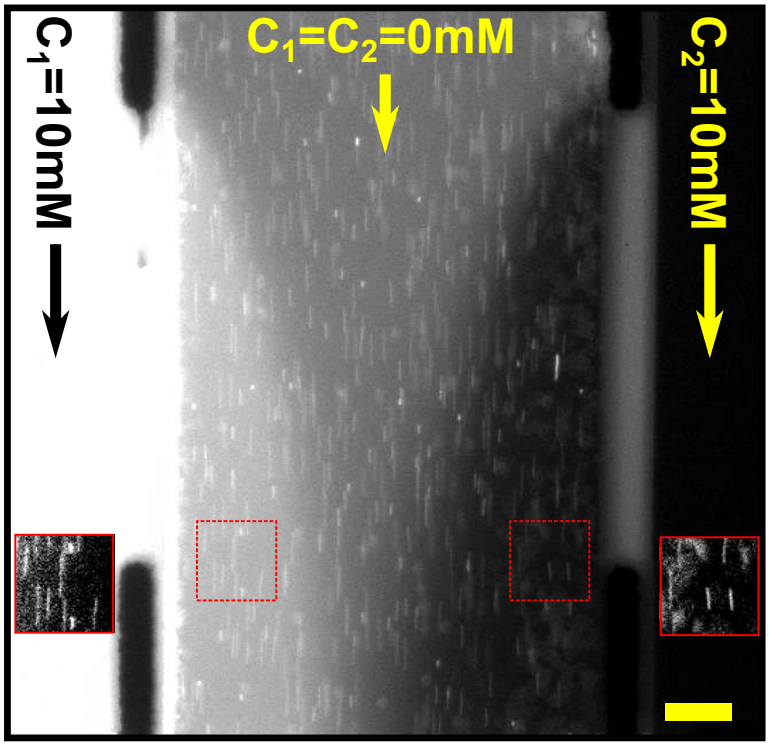

Figure 4.2: HMMs are permeable to small-molecule solutes, yet admit no measurable hydrodynamic flow. The device design is the three-channel device shown in Fig. 4.1b, and specifically show the same close-up view as fig. 4.1c. All channels contain fluorescent pH indicator at the same concentration, and each channel is buffered at a different pH: 8.1 (left, bright), 6.3 (center, intermediate), and 4.7 (right, dark), with ionic strengths balanced. Fluorescent tracer particles (bright lines) travel in straight lines past the center channel, indicating no convective inflow through either the left or right HMM. Diffusion of pH buffers through the membrane is clearly evident. Insets: contrast-enhanced and enlarged images showing tracer particle paths. Scale bar: $20\mu m$.

were pressurized at 150 mbar using compressed air, and the sample channel inlet was held at $\sim$ 2mbar with hydrostatic pressure, giving a transmembrane pressure $\Delta P_m = 75$ mbar and flow velocities that are 75 times faster in reservoir channels than in the sample channel. Buffers in the reservoir channels visibly diffuse into the sample channel, as indicated by the change in fluorescence intensity, and are convected downstream by the sample channel flow. Tracer particles in the sample channel follow straight trajectories past the HMMs, indicating the absence of detectable hydrodynamic flow through the membrane, despite the trans-HMM pressure difference. Transport of buffer through the HMM from the reservoir to the channel is thus predominantly diffusive.

4.4.2 Solvent delivery for antisolvent crystallization

HMMs are also permeable to solvents miscible with water, allowing solvent as well as solute to be introduced from reservoirs. Ethanol, for example, reduces the solubility of KCl in water, and HMMs can be used to trigger anti-solvent crystallization. Fig. 4.3 shows a three-channel device, where ethanol flows through the two outer reservoir channels, and saturated KCl through the central sample channel. When the KCl flow is stopped (fig. 4.3a) ethanol diffuses into the quiescent KCl solution in the sample channel, provoking the nucleation and growth of salt crystals (fig. 4.3b-c). Flushing the anti-solvent by re-starting KCl flow

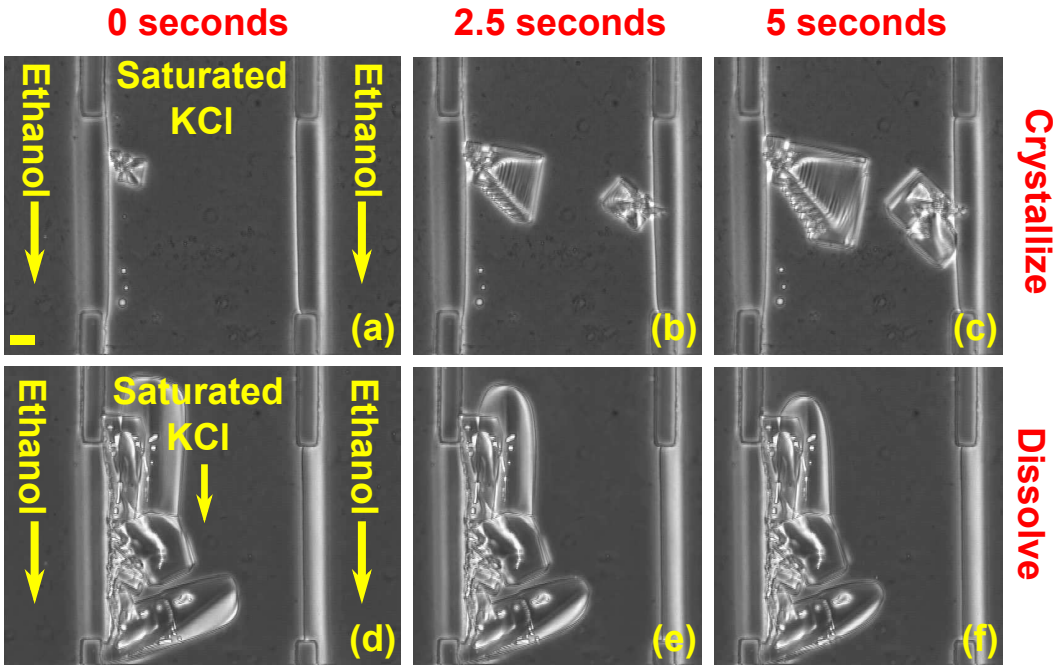

Figure 4.3: Antisolvent from two reservoir channels diffuses across HMMs into a saturated aqueous salt solution in the sample channel, depicted in the three-channel device of fig. 4.1b-c. **(a-c)** Upon stopping KCl flow in the sample channel, ethanol diffuses through the HMMs. As ethanol concentration progressively increases near the HMM, KCl solubility decreases, triggering nucleation and growth of KCl crystals. **(d-f)** Resuming convective delivery of fresh aqueous KCl solution flushes away the ethanol, restoring KCl solubility to its bulk aqueous value, and dissolving the crystals. (Phase contrast, scale bar=20 μm.)

(fig. 4.3d) causes the KCl crystals to gradually dissolve (fig. 4.3e-f). Such crystallization/dissolution experiments can be repeated indefinitely, so long as the sample channel is not completely blocked by crystals, and can thus be flushed with KCl flows.

4.5 Conclusion

In this chapter I described the concept for hydrogel membrane micro-windows (HMMs), thin local membranes that enable stepwise convection-diffusion for microfluidic systems. I described the fabrication method, which relies on photopolymerization of UV-reactive polymers. Finally, I demonstrated the basic operation of HMMs for diffusive delivery of solute and solvent. In the next chapter, I demonstrate how the local permeability of HMMs allows microscale spatial sample and solution control, and measure permeability properties.

Chapter 5

HMMs for locally permeable microchannel walls

5.1 Introduction

In this chapter, I begin by demonstrating how local permeability of microchannel walls can be used for enhanced spatial control over solutions in microchannels. This is demonstrated by using their local electric permeability to electrophoretically control colloid motion (Sec. 5.2), and using their local chemical permeabilty to set up solute and solvent concentration gradients locally across microchannels

This chapter is adapted from from Paustian *et al.*, *Physical Review X* 3 041010 (2013). http://dx.doi.org/10.1103/PhysRevX.3.041010

(Sec. 5.3). I then investigate the hydraulic and diffusive permeability properties of HMMs and find a simple method to engineer their hydraulic permeability.

5.2 Local electric permeability

Most microfluidic walls are electrically insulating, including NOA-81. The electric permeability of hydrogels, by contrast, suggests HMMs may be used to apply and shape local electric fields in microchannels, using electrodes in solutions that are physically distinct from the solution of interest.

Integrating HMMs into electrode systems alleviates many issues that arise in conventional electrokinetic microfluidic systems. First, HMMs require no additional clean room processes, unlike photolithographically patterned electrodes, which typically require clean-room metal deposition steps and separate masks. Second, electrolysis changes solution composition near electrodes, *e.g.* generating gas bubbles or introducing gradients in pH or metal ions, potentially fouling nearby samples of interest. Instead, placing metal pin electrodes in flowing electrolyte reservoirs behind HMMs allows undesirable electrochemical reaction products or bubbles to be continually flushed away, thus maintaining steady electrolyte solutions and unfouled sample environments. No clean room time is required for the electrokinetic systems in fig. 5.1, other than initial silicon master fabrication.

This ability to electric fields naturally suggests novel capabilities for a variety of experiments, including electrophoretic separations [Takahashi et al., 2003], local electrophoretic delivery [Hoffman, 2012], microfluidic salt bridges (*e.g.* for maintaining separate reference and working electrode solutions [Dydek et al., 2012]), and localized or selective electroporation of cells, organisms or vesicles [Fox et al., 2006]. While electrically permeable gels could also be made with contact lithography for these applications (and have been, in some cases [Dhopeshwarkar et al., 2005, Chun et al., 2005, Kim et al., 2009, Chun et al., 2010]), HMMs enable closer electrode spacing, allowing higher currents and smaller dimensions to be obtained. With further development, HMM-electrophoresis could be used for electrophoretic mobility measurements or particle sorting (*e.g.* cell separation based on an upstream measurement).

To demonstrate the electrical behavior near HMMs, I electrophoretically oscillated 500 nm fluorescent polystyrene colloids [Oddy and Santiago, 2004] (Bangs Labs, FS03F) in a 1 mM NaCl solution in the sample channel of a three-channel device by imposing a 5 Hz, 400 V_{pp}, potential difference between stainless steel pins at the inlets of the two reservoir channels. A 0.4s exposure (fig. 5.1) shows colloids tracing the local electric field lines, much like iron filings in a magnetic field, confirming that the electric field passes through HMMs but not microchannel walls.

Figure 5.1b-c show a continuous flow particle separation enabled by HMMs. A DC field is applied across the HMMs, transverse to a pressure driven flow, causing the flowing particles to move electrophoretically to one side of the channel. The direction of colloidal motion and downstream width-fraction containing colloids can be controlled by changing the voltage.

5.3 Local concentration gradients

Steady microfluidic concentration gradients can be used to expose samples and surfaces to impose continuous concentration gradients across a sample, allowing high-throughput experiments (*e.g.* for optimization of reaction conditions, cellular response [Ostrovidov et al., 2012, Kothapalli et al., 2011], or other concentration-dependent phenomena [Pascall and Squires, 2010b, Pascall and Squires, 2010a]). Chemical gradients also drive interesting and useful microscale phenomena such as diffusiophoresis [Derjaguin et al., 1947, Anderson et al., 1982a, Prieve et al., 1984a, Ebel et al., 1988, Anderson, 1989, Abcassis et al., 2008, Abcassis et al., 2009, Palacci et al., 2010, Palacci et al., 2012] , chemotaxis [Dormann and Weijer, 2003, Diao et al., 2006, Cheng et al., 2007, Irimia, 2010], and biological signaling [Nathan, 2006, Cyster, 1999, Moseley et al., 2009, Dubrulle and Pourqui, 2004].

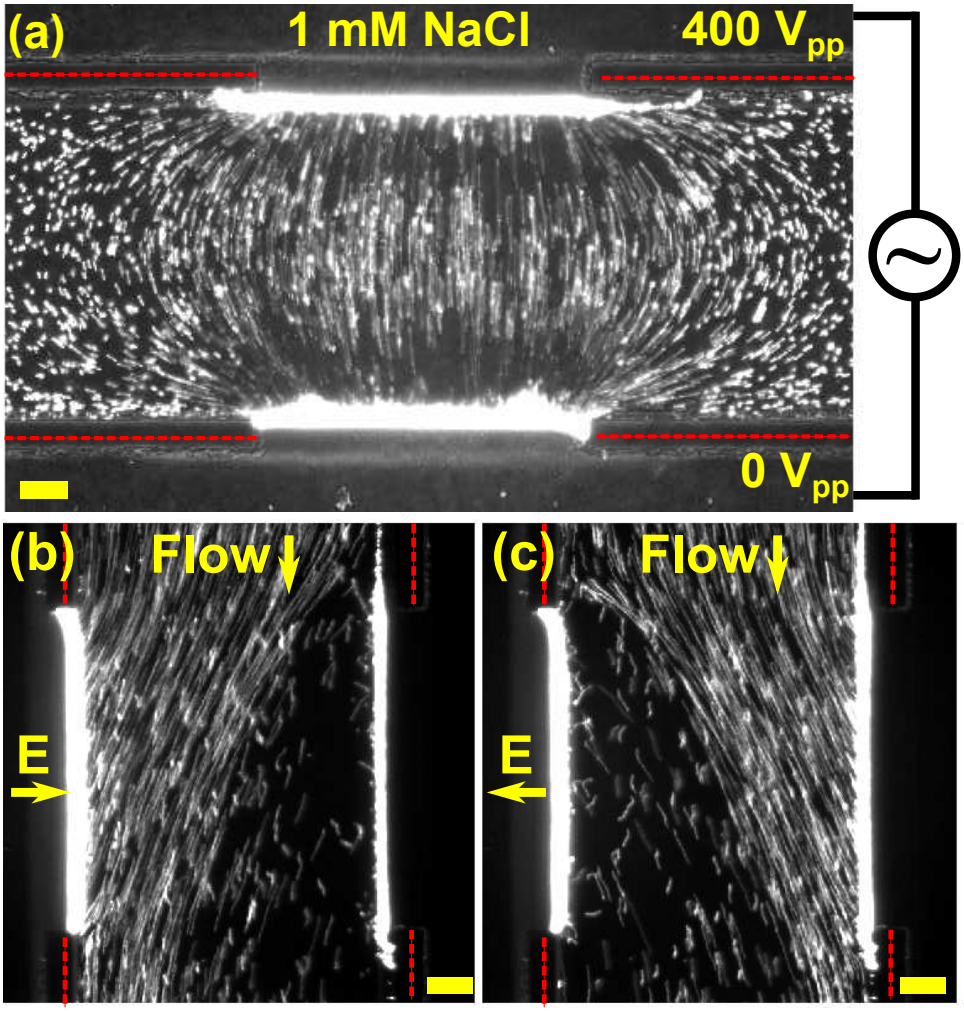

Figure 5.1: **(a)** An AC potential applied between reservoir channel inlets, drives an electric field that only crosses the sample channel through the HMMs. Fluorescent colloids in the sample channel oscillate electrophoretically, tracing local electric field lines much like iron filings align with magnetic fields. **(b-c)** Continuous-flow electrophoretic separations of negatively charged colloids by applying a DC electric field E transverse to flow. Scale bars: 20 μm.

The locally-integrable nature of HMMs allows novel design capabilities for concentration fields, *e.g.* gradient shaping and integration into more complex chips without stringent demands on overall pressure balances. Multiple HMMs, each with its own distinct and individually-addressable reservoir channel, enable the creation of almost arbitrarily complex chemical micro-environments composed of multiple species. The speed, ease, and small chip area of the HMMs makes them particularly appealing for producing on-chip concentration gradients, compared to other microfluidic methods.

Using the three-channel geometry, I used HMMs to suddenly impose a fluorophore concentration gradient (fig. 5.2a). All three channels contain 10 mM MES buffer, but each carries a different concentration of the fluorophore Oregon Green 488 (Invitrogen)) – 0 mM, 0.5 mM, and 1 mM, respectively – so that flowing channels appear dark, medium, and bright. Within several minutes of injecting these solutions, flow in the sample channel is quickly stopped using PDMS valves (0 sec.). A linear gradient is quickly established (20 sec.) and maintained at steady state. The predicted diffusion time ($\tau_D = (2w_m + w_s)^2/(\pi^2 D) = 9$ s, based on D=4x10^{-10}m^2/s [Mller et al., 2008]) agrees well with the transient time scale (*i.e.* $t \approx 2\tau_D$ for the transient to decay by 90%).

Solute gradients drive colloids into diffusiophoretic motion (fig. 5.2b-c). Nonetheless, it has been difficult to directly visualize colloidal diffusiophoresis, as con-

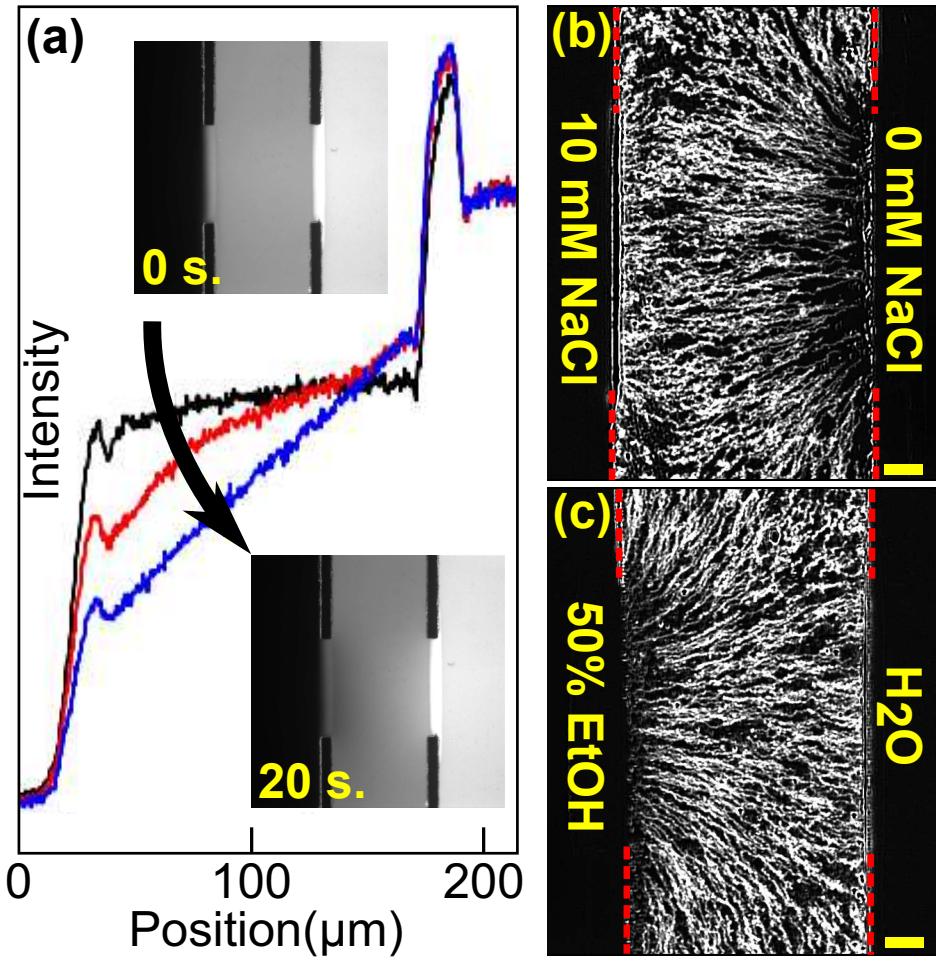

Figure 5.2: Concentration gradients created locally within microchannels. **(a)** Direct gradient visualization with Oregon Green fluorescent dye at 0 (black), 10 (red), and 20 (blue) seconds after stopping flow. **(b)** Diffusiophoretic motion of fluorescent colloids up a NaCl gradient. **(c)** Solvophoretic motion down an ethanol gradient. Scale bar: 20 μm.

centration gradients strong enough to drive diffusiophoresis generally give rise to hydrodynamic instabilities in macroscopic experiments. By contrast, the small dimensions of microfluidic systems enable even strong gradients to remain hydrodynamically stable. Recent microfluidic experiments have visualized diffusiophoresis in salt gradients, or "electrophoretic" diffusiophoresis [Abcassis et al., 2008, Abcassis et al., 2009, Palacci et al., 2010, Palacci et al., 2012]. Complementing these studies, localized diffusiophoresis using HMMs is demonstrated here. Fig. 5.2b shows the diffusiophoretic migration of colloids up a NaCl gradient established in a three-channel geometry ($\tau_D = 2.3$ sec.). Channel solutions were initially established and maintained by flowing solutions of 10 mM NaCl (left reservoir), 5 mM NaCl with 500 nm polystyrene beads (sample), and DI water (right reservoir). Flow was quickly eliminated in the sample channel by submerging both inlet tubes in a small beaker [Mansuripur et al., 2009] and the following 8.3 seconds of fluorescence images were superposed. Beads clearly migrate diffusiophoretically up the gradient in NaCl, even tracking the 2D 'fringing' shape once the gradient is established.

HMMs can also be used to establish solvent gradients, which can drive colloidal "chemiphoretic" diffusiophoresis [Anderson et al., 1982a, Anderson, 1989] or "solvophoresis" [Kosmulski and Matuevi, 1992]. While solvophoresis has been seen in macroscopic aggregation experiments [Kosmulski and Matuevi, 1992], it

has never been visualized experimentally. The solvent compatibility of HMMs and NOA-81 devices enabled the first direct visualization of colloids moving solvophoretically (fig. 5.2c).

To generate solvophoresis using HMMs, channels initially contain flows of (left to right) 50%, 25%, and 0% v/v ethanol solutions in DI water ($\tau_D = 2.9$ s), with 10 mM KCl in each to balance ionic strength, and superpose 10.4 seconds of images once the central flow is stopped. Polystyrene colloids migrate down the ethanol gradient solvophoretically (fig. 5.2c).

5.4 Permeability properties

To examine HMMs with different polymer network densities (fig. 5.3), HMMs from different precursor solutions were photopolymerized within a single, three-channel device: the left HMM using a 50% v/v PEG-DA solution and the right HMM from the standard 20% v/v solution.

5.4.1 Hydraulic permeability

To compare the Darcy permeability of the 20% and 50% PEG-DA HMMs, the transmembrane pressure, ΔP_m, was brought to 1.5 bar by pressurizing the reservoir inlets to 3.0 bar using compressed air and sealed containers, while main-

taining the pressure difference across the sample channel maintained at 3.9 mbar by immersing inlet and outlet tubing in beakers, one of which was attached to a vertical sliding stage [Groisman et al., 2003]. The transmembrane flow was visualized using the bead-free region near the membranes (fig. 2b in main text).

To calculate the Darcy permeability from this image, the width of the bead-free regions at the bottom of the image, $\delta_f^{L,R}$, must be related to the velocity through the left and right HMMs, $u_m^{L,R}$. These velocities will be uniform across the HMM cross section, so that

$$Q_m^{L,R} = L_m h u_m^{L,R} \tag{5.1}$$

where $Q_m^{L,R}$ is the flow rate through the left or right HMMs, h is the channel height, and L_m is the membrane length. Assuming fully developed Poiseuille flow at the top and bottom of the image, the flow profile is given by [Bruus, 2007]

$$u_y(x,z) = \frac{4h^2\Delta P}{\pi^3 \eta L} \sum_{n,odd}^{\infty} \frac{1}{n^3} \left[1 - \frac{\cosh n\pi \frac{x}{h}}{\cosh n\pi \frac{w}{2h}} \right] \sin(n\pi \frac{z}{h}). \tag{5.2}$$

where y runs along the channel, $-w_s/2 \leq x \leq w_s/2$ and $0 \leq z \leq h$. When $w_s \gg h$ (15:1 here), the maximum velocity is

$$u_{max} = \frac{4h^2\Delta P}{\pi^3 \eta L} \sum_{n,odd}^{\infty} \frac{(-1)^{\frac{n-1}{2}}}{n^3} \approx 0.97 \frac{4h^2\Delta P}{\pi^3 \eta L} \tag{5.3}$$

PEG-DA%	u (μm/s)	κ (nm^2)	l_p (nm)
20	20	11	3.3
50	57	4.4	2.1

Table 5.1: HMM Darcy permeabilties and estimated pore sizes

Assuming the beads follow the streamlines ($Pe_{bead} \sim 10^4$), δ_{f1} can be used to relate to the maximum velocity downstream of the HMMs, u_{bot}, to Q_m^L, by

$$Q_m^L = \int_0^h \int_{-w_s/2}^{-w_s/2+\delta_f^L} u_y(x,z)dxdz = \tag{5.4}$$
$$\frac{8h^3\Delta P}{\pi^4 \eta L} \sum_{n,odd}^{\infty} \frac{1}{n^4} \left(\delta_f^L - \frac{h}{n\pi} \left(1 - \frac{\sinh n\pi \frac{w_s - 2\delta_f^L}{2h}}{\cosh n\pi \frac{w_s}{2h}} \right) \right) \approx \frac{\delta_f^L h^3 \Delta P}{12\eta L},$$

where the last approximation holds for $\delta_f^L \gg h/\pi$. Comparing this relation to eqn. 5.3 and by analogy the right side,

$$Q_m^{L,R} \approx 0.67 \delta_f^{L,R} h u_{max} \tag{5.5}$$

giving from eqn. 5.1,

$$\boxed{u_m^{L,R} \approx 0.67 \frac{\delta_f^{L,R} u_{bot}}{L_m}} \tag{5.6}$$

Table 1 shows the values of u for each HMM, as well as the Darcy permeability $\kappa = u\eta w_m / \Delta P_m$ and estimated pore size $l_p \sim \sqrt{\kappa}$ calculated from that velocity.

Since this approach involves several assumptions, I verify that u_m satisfies a mass balance.

$$Q_{m1} + Q_{m2} + Q_{top} = Q_{bot}. \tag{5.7}$$

For rectangular Poiseuille flow in a 15:1 aspect ratio channel, the flow rate can be related to u_{max} by

$$Q = \frac{\pi^3 h w_s}{48} u_{max}, \tag{5.8}$$

so the mass balance gives

$$u_{left} + u_{right} = \frac{\pi^3 w_s (u_{bot} - u_{top})}{48 L_m}. \tag{5.9}$$

Comparing the values of the LHS from Table 1 to the RHS from the measured tracer bead displacement, the mass balance matches within 5%.

5.4.2 Diffusive permeability

Despite the lower Darcy permeability of the 50% HMM, its diffusive flux was indistinguishable from that of the 20% HMM. In fig. 5.3b, both reservoir channels were buffered at pH 9.8 with 10 mM Na_2CO_3 and pressurized to 150 mbar as previously, whereas the sample channel was held at pH 6.3 by 1 mM MES buffer. The flow velocity in the sample channel was set by controlling the hydrostatic pressure [Groisman et al., 2003]. All solutions contained 25 μM fluorescein as a pH indicator, revealing a bright boundary layer alongside each HMM (Fig. 5.3b), with width δ defined when the intensity drops to 20% of its maximum value.

Boundary layer widths for 20% and 50% HMMs are nearly identical at all channel velocities measured (fig. 5.3c). This indicates either identical effective diffusivity or solution-dominant mass transfer resistance for Na_2CO_3 in PEG-DA, since w_m is nearly identical for the two HMMs. Larger solutes, however, have been shown to have decreased diffusivity in high concentration PEG-DA gels [Cuchiara et al., 2010].

The shape of the boundary layer reflects the competing effects of diffusion and convection, and thus depends upon the Peclet number Pe=Uw_s/D, where U is the average velocity (calculated from the pressure head and hydraulic resistance [Bruus, 2007]), w_s is the sample channel width, and D is the solute diffusivity (*e.g.* $D = 10^3 \mu m^2/s$ for Na_2CO_3 [Cussler, 1997]). Depth-averaged 'Hele-Shaw' flows in low-aspect ratio channels (here 10 μm tall by 150 μm wide) have approximately uniform profiles. Solute diffusing perpendicular to such uniform flows at high Pe establish boundary layers with thickness $\delta/w_s \sim \mathrm{Pe}^{-1/2}$, as observed here (fig. 5.3c). The detailed, three-dimensional concentration profile, however, will reflect the inhomogeneous (parabolic) flow across the channel [Ismagilov et al., 2000].

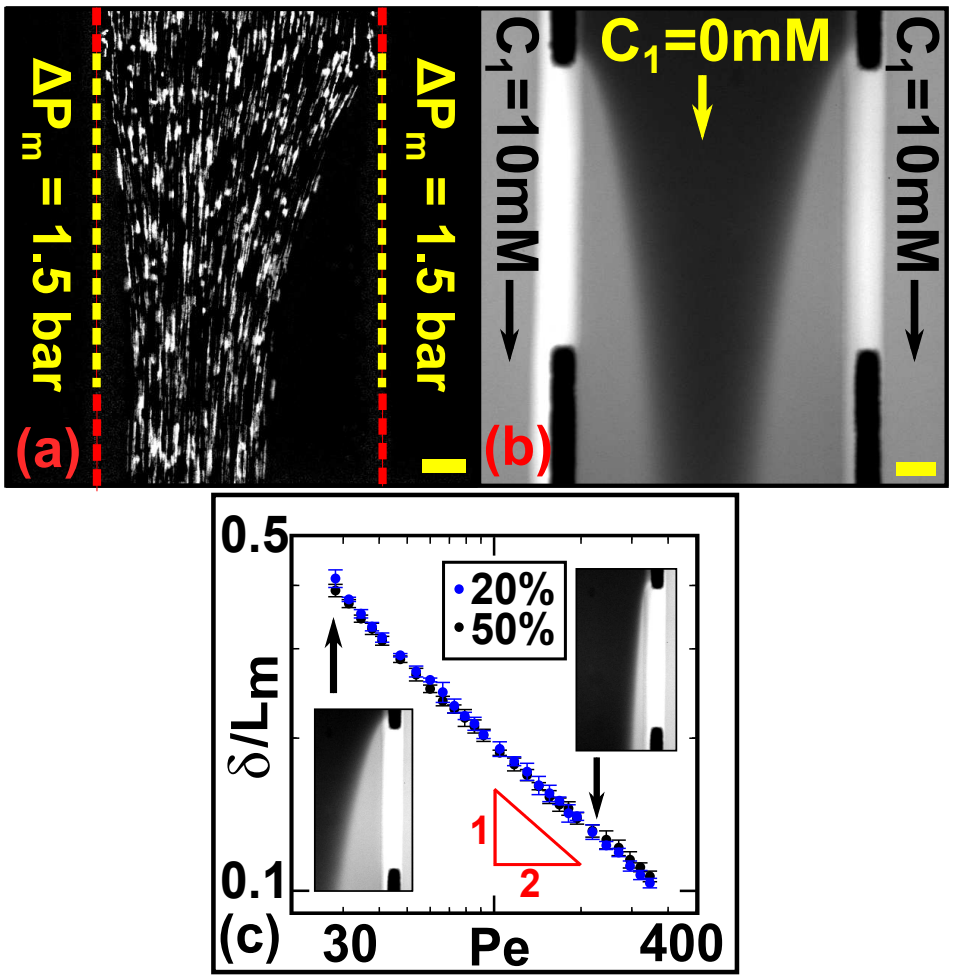

Figure 5.3: **(a)** In the three-channel device (figs. 4.1b-c), the amount of convection admitted by HMMs at large transmembrane pressure drops, here $\Delta P_m = 1.5$ bar, is lower for a highly-crosslinked HMM (50% v/v, left) than for a lightly-crosslinked HMM (20%, right). Tracer particles are focused towards the center of the channel by trans-membrane flow from the side channels. **(b)** The diffusive flux through a lightly-crosslinked membrane (20% v/v, right) is nearly identical to that through a highly-crosslinked (50% v/v, left) membrane. **(c)** After diffusing through each HMM, pH buffer is convected downstream, forming a boundary layer whose thickness decreases with Peclet number (flow velocity) like $\mathrm{Pe}^{1/2}$, as expected for 2D convection-diffusion. Scale bars: $20\mu m$.

5.5 Conclusion

HMMs enable microchannel walls that are locally permeable to electric and concentration fields, while acting as mechanical barriers to flow. The electric permeability was demonstrated by visualizing the electrophoretic motion of colloids, while the local concentration gradient capability was shown with diffusiophoretic and solvophoretic motion visualizations, along with fluorescent dye gradients. The dependence of the hydraulic and diffusive permeability on pore size was also investigated, and the hydraulic permeability was found to strongly depend on the concentration of PEG-DA in the precursor solution, while the diffusive permeability of sodium carbonate was relatively insensitive to this quantity.

Chapter 6

Rapid dialysis using thin hydrogel membranes

6.1 Introduction and concept

This chapter describes HMM-Rapid Dialysis (HMM-RaD) experiments, in which HMMs are used to rapidly change a chemical microenvironment. Such rapid diffusive swapping could be used for cell and developmental biology [Keenan and Folch, 2007]; modification of colloids and surfaces (*e.g.* for sample sorting, binding assays, or fundamental surface studies) [Sperling and Parak, 2010], and

This chapter is adapted from from Paustian *et al.*, *Physical Review X* 3 041010 (2013). http://dx.doi.org/10.1103/PhysRevX.3.041010

provoking the transient response of complex and soft materials [Scrimgeour et al., 2011]. These demonstrations also show that HMMs can be readily integrated with PDMS microvalves for rapid stepwise convection-diffusion.

6.2 Expermental methods

6.2.1 Device Fabrication

To investigate the temporal response of HMM-RaD experiments, tri-layer devices were designed and fabricated (Figure 6.1a). The fluidic layer, cast in NOA-81, consisted of a sample channel (width w_s either 150μm or 23μm), separated from a reservoir channel (300 μm wide) by a HMM of width w_m of 17μm. Solutions were delivered to the sample and reservoir channels through channels in a PDMS layer bonded atop the NOA-81 layer [Galas et al., 2009], and flows within the PDMS delivery channels were controlled with multilayer soft lithography 'push-up' valves [Unger et al., 2000] at intersections of the control and injection channels. In order to rapidly change between two reservoir solutions, two valved injection channels met over the NOA-81 reservoir inlet; all other inlets had a single valved injection channel for eliminating flow. The single layer NOA-81 device and two-layer PDMS device were fabricated separately according to standard 'stickers'

[Bartolo et al., 2008] and MSL [Melin and Quake, 2007] protocols, respectively, then ozone-bonded together.

6.2.2 Expermental procedure

To achieve precise valve timing, PDMS control channels were filled from sealed fluid containers which were switched between 0 and 750 mbar using computer-controlled solenoid valves (Pneumadyne S10MM-30-12-3) [Melin and Quake, 2007], while the two reservoir solutions were pressurized to 250 mbar.

6.3 Experimental results

Fig. 6.1b shows reversible HMM-RaD in a 150 μm wide sample channel. NaCl was chosen as solute due to its relatively high diffusivity (D=1.6x10^{-5}cm^2/s [Cussler, 1997]) among salts with an available indicator dye (CoroNa Green, Invitrogen). Solutions were prepared consisting of 40 μM CoroNa Green, 10 mM MOPS buffer (pH 7), and 0 mM NaCl (dark) or 250mM NaCl(bright). The fluorescence intensity of CoroNa was found to increase linearly with NaCl concentration in this range. Three 300 μm HMMs were polymerized to form a 900 μm long HMM. The reservoir solutions were periodically switched every 40 seconds, and the relative fluorescence intensity $(I(t) - I_f)/(I_0 - I_f)$ was averaged over the sample channel

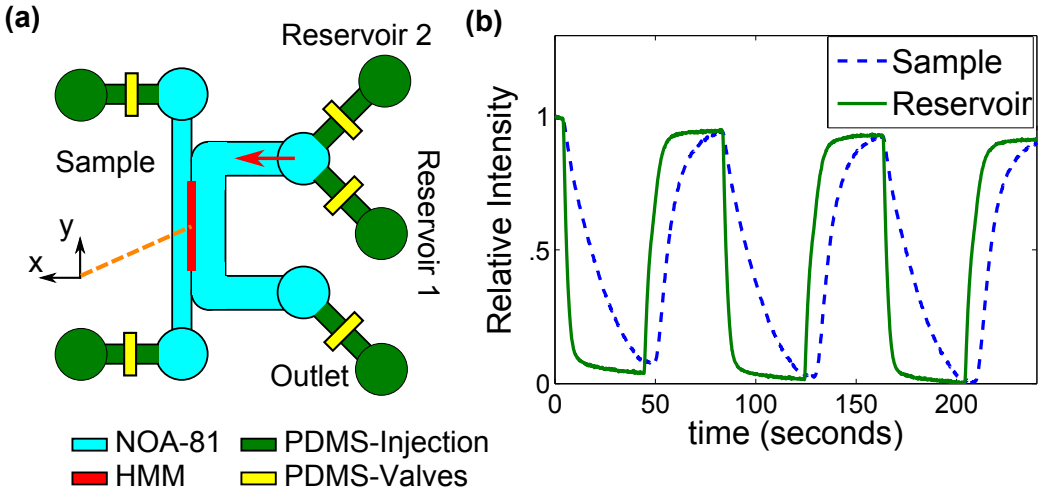

Figure 6.1: **(a)** Device geometry for prompt reservoir solution swapping using PDMS valves and rapid dialysis in the sample channel using an HMM. Credit: Matthew J. Gillkey for aiding photomask design. **(b)** Swapping between 250mM NaCl (bright) and 0mM NaCl (dark) solutions in a 150 μm wide sample channel, with fluorescent NaCl indicator.

region adjacent to the middle 300 μm HMM. The fluorescence intensity changes exponentially with a time scale $\tau_{\text{meas}} \approx 20$ s, which is slower than the $\tau_D = 7$s predicted from simple diffusion through an inert HMM,

$$\tau_{\text{RaD}}^{\text{min}} \sim \tau_D \sim \frac{4(w_m + w_s)^2}{\pi^2 D}, \tag{6.1}$$

(or, if solute were introduced from both sides and reservoirs synchronized, a factor of 4 faster). This suggests that the HMM introduces a mass transport resistance comparable to that of the sample channel, discussed below.

By decreasing the width of the sample channel, even faster solution swapping could be performed. A HMM-RaD device with sample channel of width w_s=23

μm and HMM of width $w_m = 17\mu$m (for which (6.1) predicts τ_D=0.4 s) was fabricated for this purpose. Fig. 6.2a shows the relative intensity averaged over the entire sample channel width and 1 μm of HMM at the sample interface. The intensity in the sample chamber closely follows that in the HMM, which changes exponentially with time constant $\tau_m = 2.5$ s. Swapping between 250 mM and 0 mM NaCl results in 90% NaCl removal in 5.6 seconds. Given the much faster τ_D from (6.1), the HMM-RaD is limited by the HMM itself. Figure 6.2b shows excellent agreement between the experimental concentration profile $c(x,t)$ and analytical theory within the sample chamber, imposing the experimentally observed τ_m as a boundary condition, but introducing no other free parameters.

Several mass transport processes may lengthen the time required for HMM-RaD beyond eq. (6.1): (i) diffusion across the boundary layer between the reservoir and the HMM; (ii) diffusion across the sample chamber, and (iii) diffusion through the HMM itself. The final is most likely, because the diffusivity D_m is usually slower within membranes than in solution for simple geometric reasons [Cussler, 1997], and may be reduced even further by adsorption. In addition to these steady-state mass transport limitations, highly-partitioning solutes require a finite time to 'fill' the HMM, before even quasi-steady diffusive permeation occurs.

6.4 Model for mass transport in rapid dialysis experiments

To analyze the spatio-temporal response of solute in HMM-RaD, I use a one-dimensional model system consisting of a sample channel ($0 < x < w_s$) with HMM at $x = 0$ and impermeable wall at $x = w_s$. The full solute transport dynamics depend on the sample channel and HMM geometry, the solute diffusivity D in the sample channel and D_m in the PEG-DA HMM, and the partition coefficient $K = c_m^{\mathrm{eq}}/c^{\mathrm{eq}}$ of the solute in the membrane.

To simplify the situation, consider only the sample channel concentration, which obeys

$$\frac{\partial \hat{c}}{\partial \hat{t}} = D\frac{\partial^2 \hat{c}}{\partial \hat{x}^2}, \tag{6.2}$$

with dimensional variables hatted. Assuming the NaCl concentration to be proportional to the intensity in the HMM, the experimentally observed boundary condition at the hydrogel is $\hat{c}(0,t) = c_0 e^{-\hat{t}/\tau_m}$. The other two conditions are standard ($\partial\hat{c}(w_s,\hat{t})/\partial\hat{x} = 0$, and $\hat{c}(\hat{x},0) = c_0$). The equation was non-dimensionalized by $x = \hat{x}/w_s$, $c = \hat{c}/c_0$, and $t = \hat{t}/\tau_S$, with $w_s = 23\mu$m, c_0 =250 mM, and

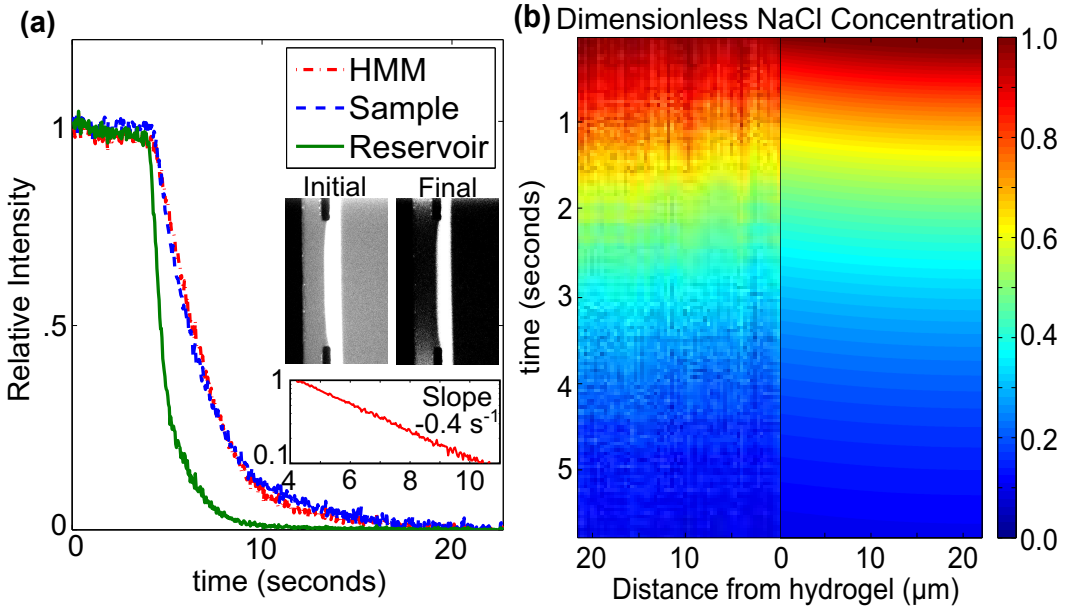

Figure 6.2: **(a)** Swapping time is greatly decreased by decreasing sample channel width (here, 23 μm wide). Inset graph: semilog plot of HMM intensity shows exponential decay of salt concentration in HMM. **(b)** Observed dynamics of NaCl concentration along the x-axis of the sample channel are well predicted by the 1D diffusion equation.

$\tau_S = w_s^2/D = 0.3$ s. The resulting dimensionless problem,

$$\frac{\partial c}{\partial t} = \frac{\partial^2 c}{\partial x^2}, \tag{6.3}$$

$$c(0,t) = e^{-kt}, \frac{\partial c(1,t)}{\partial x} = 0, c(x,0) = 1 \tag{6.4}$$

with $k = \tau_S/\tau_m$, can be solved by making the substitution $u(x,t) = c(x,t) - e^{-kt}$ and solving for $u(x,t)$ using eigenfunction expansion [Farlow, 1993], giving

$$c(x,t) = e^{-kt} + \sum_{n=1}^{\infty} \frac{2k}{\lambda_n(\lambda_n^2 - k)} \left(e^{-kt} - e^{-\lambda_n^2 t}\right) \sin \lambda_n x, \tag{6.5}$$

where $\lambda_n = \pi(n - \frac{1}{2})$. Figure 4d in the main text shows excellent agreement between experiment and Equation 6.5 using the experimentally observed τ_m, but no other free parameters.

6.5 Conclusion

Using hydrogel membranes, rapid solution swapping has been demonstrated over second timescales. This is over an order of magnitude faster than all other methods for performing flow-free solution swapping in microfluidic devices. By combining thin hydrogel membranes with thin microfluidic channels, previously inaccessible time scales for diffusive solution swapping can be accessed.

Chapter 7

Direct measurements of colloid diffusiophoretic and solvophoretic velocity

7.1 Introduction

7.1.1 Diffusiophoresis: physical picture

When a gradient of a small solute (*i.e.* salt) arises within a solution containing colloids or polymers, migration of the colloids and polymers along the solute gradient will sometimes occur. This phenomenon, "diffusiophoresis," [Prieve, 2008],

is well established by colloidal science literature [Anderson, 1989] as an important mechanism for multicomponent diffusion of large solutes [Shaeiwitz and Lechnick, 1984, Lightfoot et al., 1962], but has been challenging to study experimentally. Diffusiophoresis could occur in any process where solute concentration gradients can arise, and in particular, could lead to surface deposition of particles and polymer, whether purposeful (*e.g.* film deposition and coatings) or unintentional (*e.g.* contamination and fouling). Diffusiophoresis can happen mainly in low Peclet number processes (or within low-Pe boundary layers), for example membrane processes, packed-bed reactors, separation processes, crystallization processes, and biological processes. An improved understanding of diffusiophoresis would be widely relevant for understanding and engineering these processes.

To explain diffusiophoresis, an explanation of "diffusioosmosis" is first necessary. Diffusioosmosis is a flow driven along a surface by a bulk concentration gradient. Fig. 7.1a shows a standard mechanism for diffusio-osmosis. In fig. 7.1a, a solute has bulk concentration $n_\infty(x)$ with constant gradient ∇n_∞. This gives rise to a bulk chemical potential gradient $\nabla \mu_\infty = kT \nabla \ln n_\infty$. The absolute solute concentration near the surface $n_s(x, y)$ is different than the bulk, $n = n_s - n_\infty$ in a thin "excess layer" near the surface. This occurs because of surface-solute interactions, such as electrostatic attraction, Van der Waals forces, excluded volume forces, or hydration forces. The concentration gradient puts an entropic force on

the excess layer, resulting in body force $f = -n\nabla\mu$ on the fluid near the surface. This gives rise to a diffusio-osmotic slip (fig. 7.1a). The relationship between diffusioosmosis and diffusiophoresis is analogous to that between electroosmosis and electrophoresis. Particles are forced into diffusiophoresis by a solute gradient, which causes diffusioosmosis along its surface (fig. 7.1b).

Diffusioosmosis/diffusiophoresis under salt gradients has been studied more than non-electrolyte gradients. The mechanism for this is mainly electroosmosis due to an electric field that arises in salt gradients (fig. 7.1c). The strength of this electric field can be derived from the Nernst-Planck equation [Anderson, 1989]. At steady state and negligible Pe number, the salt motion is the sum of diffusion and electromigration,

$$0 = D_i \nabla n_i - \frac{ezD_i}{kT} n_i \nabla\phi, \tag{7.1}$$

with diffusivity and concentration of species i given by D_i and n_i and electric potential ϕ. By enforcing charge neutrality in the bulk, $n_+ + n_- = 0$, and assuming a symmetric $z:z$ electrolyte, the bulk electric field is

$$\nabla\phi = \frac{kT}{ze}\beta\nabla\ln n, \tag{7.2}$$

with

$$\beta = \frac{D_+ - D_-}{D_+ + D_-}. \tag{7.3}$$

Diffusiophoresis in a salt gradient will occur partially due to the natural electric field that arises within salt gradients when the ions have nonzero β, causing electrophoretic motion of the particle (fig. 7.1d). In reality, even salts with $\beta \approx 0$ can migrate by "chemiphoretic" diffusiophoresis, which happens when uneven osmotic pressure across the particle surface in the double layer drives the particle into motion. The distinction between these two mechanisms will be further explained subsequently.

7.1.2 Background

Diffusiophoresis came into industrial use as a method to deposit latex films upon reacting metal molds. It was first described in the Russian literature in the context of understanding this industrial process [Deryaguin et al., 1961]. Prieve, Anderson and coworkers continued to develop the theoretical understanding of diffusiophoresis in the 1980's [Anderson et al., 1982b, Prieve et al., 1984b, Anderson, 1989]. They carried out an asymptotic analysis for diffusiophoresis in non-electrolyte solutes in the limit where the particle radius a is much larger than the excess layer of solute at its surface, with characteristic length L [Anderson et al., 1982b]. L is analagous to the Debye length λ_D in electrolytes, which is $\mathcal{O}(1 - 100\text{nm})$. The zero-order expression for diffusiophoretic velocity of a parti-

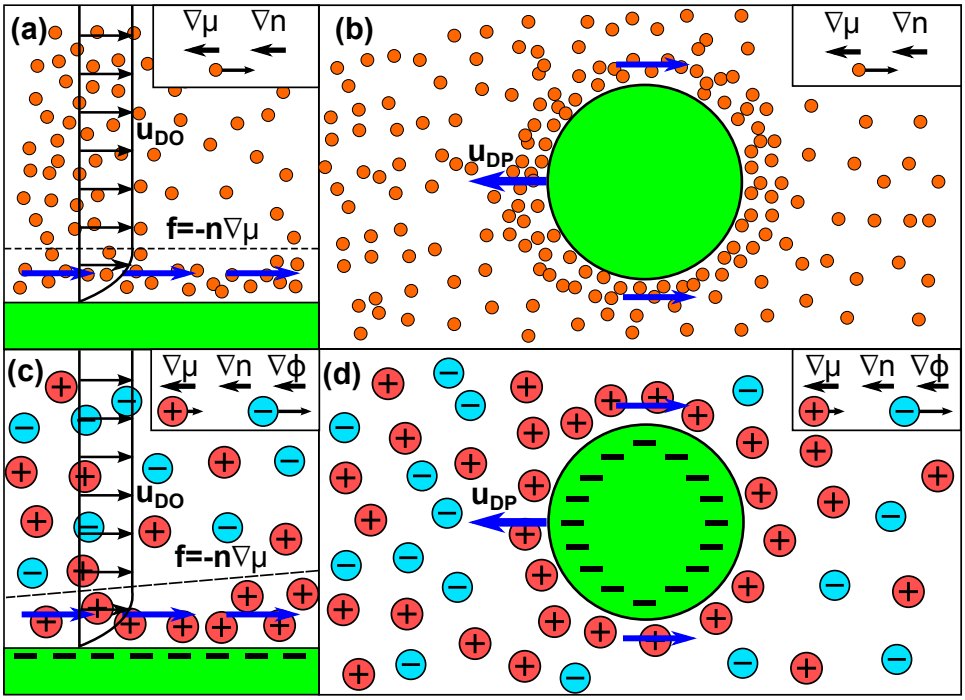

Figure 7.1: **(a)** Diffusio-osmotic flow occurs along a surface adjacent to a bulk concentration gradient ∇n (and corresponding chemical potential gradient $\nabla \mu$). A solute has excess concentration n along the surface. A body force $n\nabla\mu$ on the excess layer results in diffusio-osmotic slip along the surface. **(b)** Diffusio-osmotic slip along a colloidal particle results in diffusiophoresis. **(c)** The diffusioosmotic velocity u_{DO} in salt gradients has an electrophoretic and chemiphoretic contribution. In this case, the negative ion diffuses faster than the positive, resulting in an electric field in solution. The field puts a force on the double layer, resulting in electroosmotic slip. The chemiphoretic slip arises from uneven osmotic pressure across the surface. Combined with a chemiphoretic slip, this results in salt diffusioosmosis. **(d)** Diffusiophoresis in a salt gradient is caused by diffusioosmosis at the particle surface.

cle is

$$u = \frac{kT}{\eta} L^2 \nabla c \int_0^\infty y \left(\exp \frac{-\phi(y)}{kT} - 1 \right) dy, \tag{7.4}$$

with Boltzmann's constant k, temperature T, concentration c, solute-surface interaction energy ϕ, and distance from the surface y/L. The integrand is the moment of the solute energy well length, and the integral is $\mathcal{O}(1)$ when the solute is repelled by the surface, but may scale differently for an attractive interaction [Anderson et al., 1982b]. For example, strongly adsorbing solutes such as surfactants can have adsorption lengths as long as $\mathcal{O}(10\ \mu\text{m})$, which was predicted to exhibit a maximum diffusiophoretic velocity of $\mathcal{O}(25\ \mu\text{m/s})$ [Anderson and Prieve, 1991]. The above analysis assumed zero Peclet number, but finite Peclet number has recently been predicted to limit diffusiophoretic velocity [Khair, 2013]

Diffusiophoresis in electrolyte solutions was also studied theoretically [Prieve et al., 1984b]. The authors derived a diffusiophoretic velocity

$$u = \frac{\epsilon}{\eta} \frac{kT}{ze} \left(\zeta\beta + \frac{4kT}{ze} \ln \cosh \frac{ze\zeta}{4kT} \right) \nabla \ln c, \tag{7.5}$$

with permittivity ϵ, viscosity η, surface potential ζ, and β defined in eqn. 7.3. The left term is the electrophoretic contribution and the right term is the chemiphoretic contribution.

Early experimental studies of diffusiophoresis were able to confirm salt diffusiophoresis and measure velocities that agreed well with theory for NaCl, and

measured velocities for other electrolytes [Lechnick and Shaeiwitz, 1984]. Dialysis cells of various designs were often employed, typically containing a porous membrane between two well-mixed baths. These methods typically relied upon measurements of particle mass deposited on the membrane, when the pores were smaller than the particles. In one detailed study, Lin and Prieve demonstrated deposition of cationic particles for $\beta > 0$ (such as HCl and KIO_3, among others) and anionic particles for $\beta < 0$ (such as NaOH, KOH, and LiCl). Reduction of salt diffusiophoresis rate was demonstrated by addition of a supporting electrolyte, which reduces the gradient-induced electric field [Lin and Prieve, 1983]. Importantly, methods based on weighing of deposits often assume 100% particle coagulation at the membrane surface, even thouigh the true percentage is unknown.

The dialysis cell method could also be used with pores larger than the beads; this allowed the bead concentration to be measured via turbidity to determine the migration rate [Lechnick and Shaeiwitz, 1984]. This method allowed lower rates of diffusiophoretic transport to be measured. The authors calculated multicomponent diffusion coefficients for the bead-solute system and investigated concentration dependence of salt diffusiophoresis [Shaeiwitz and Lechnick, 1984, Lechnick and Shaeiwitz, 1985]. This was used to measure the diffusiophoretic mobilities of various salts, including standard choices such as NaCl and KCl, as well as multi-

valent ions and acetate salts. A more advanced version of this setup was used to confirm the existence of the chemiphoretic contribution using KCl gradients, as well as unambiguously confirming diffusiophoresis toward low concentration when $\beta < 0$ [Ebel et al., 1988].

Another experimental apparatus that contributed to diffusiophoresis understanding was a machined millifluidic apparatus called the "stopped-flow diffusion cell"(SFDC) [Staffeld and Quinn, 1989a]. A transparent flow cell was constructed that allowed two solutions (maintained at constant flow rate with two syringe pumps) to be brought into contact at a 4-way junction as a stagnation flow. The two colloidal solutions differed only in solute concentration. Colloidal "bands" formed due to excess and depleted bead concentration from diffusiophoresis at the junction of the two streams. The flow could then be brought to a halt by valves at the inlets and outlets and the displacement of the bead profile was used to determine the diffusiophoretic velocity. The transient solute gradient that formed resulted in formation of colloidal bands that were visualized using a stereomicroscope and camera. The authors used the SFDC to measure diffusiophoresis due to gradients of NaCl and KCl gradients [Staffeld and Quinn, 1989a]. They also studied diffusiophoresis from non-electrolytes that interacted with the colloid via excluded volume interaction [Staffeld and Quinn, 1989b]. Using gradients of Dextran (uncharged polymer, 4.8 nm radius, 0.2-1%) and Percoll (15-30 nm poly-

mer coated silica particles, 10 vol%), they fit the data to the interaction radius and found good agreement with theory.

Diffusiophoresis in solvent gradients, or "solvophoresis," has been observed in solvent gradients [Kosmulski and Matuevi, 1992]. The authors pipetted a turbid solution of one solvent on top of a bead-free solution within vials and tracked the displacement of the turbid region over many hours, demonstrating that the beads were migrating under the gradients. Tested solvent combinations included water/ethanol (with various KCl concentrations), water/glycerol, water/DMF, and 1-propanol/water. Beads migrated toward the water in most cases except the DMF. The proposed mechanism was non-electrolyte diffusiophoresis due to hydration of the particles.

Recently, advances in microfluidics have allowed direct visualization of diffusiophoretic migration of colloids and polymers. Abecassis et al. [Abcassis et al., 2008, Abcassis et al., 2009] used gradients across co-flowing solutions to visualize the migration of colloidal particles. Palacci et al. used 3-channel agarose devices to set up and switch gradients and visualize the resulting motion of colloidal particles and DNA molecules [Palacci et al., 2010, Palacci et al., 2012]. A similar phenomena, "thermophoresis" [Duhr and Braun, 2006, Wrger, 2010] or migration under temperature gradients, has been studied using microfluidics and can occur by many mechanisms, including diffusiophoresis from concentration or density

gradients induced by thermal gradients. Diffusiophoresis was also demonstrated to play a role in fouling of hollow-fiber membranes [Kar et al., 2014].

In certain situations, particles can set up their own gradients when their surface is undergoing a chemical reaction, leading to "micro-swimmers" which exhibit "self-diffusiophoresis" [Brady, 2011, Sharifi-Mood et al., 2013]. "Catalytic nanomotors" are one example, such as bimetallic rod shaped particles that migrate when immersed in a hydrogen peroxide solution [Paxton et al., 2004, Moran and Posner, 2011]. The asymmetric surface reaction sets up gradients of various reactants and products. The mechanism for phoretic motion is thought to be an electric field induced by the proton gradient, which is the same underlying physics as diffusiophoresis due to salt gradients. Another reaction-driven form of diffusiophoresis is the photocatalyzed oxidation of Ag-AgCl particles. When exposed to UV light, these particles swim toward the center of the light, which is thought to be caused by a photocatalyzed reaction at the particle surface, resulting in diffusive gradient formation in the adjacent solution [Ibele et al., 2009].

7.2 Experimental design

To set up gradients within a microfluidic channel, the hydrogel membrane micro-windows were fabricated in a 3-channel geometry [Paustian et al., 2013].

This method allows strong gradients to be established perpendicular to and entirely within the imaging plane, and the small channel dimensions prevent hydrodynamic flows and instabilities often associated with strong concentration gradients.

The concentration gradient can be calculated from the width of the hydrogels and channel. An imposed concentration gradient Δc results in a species flux j with a mass transfer resistance R_{tot} defined by

$$j = \frac{\Delta c}{R_{tot}}. \tag{7.6}$$

Here R_{tot} is the sum of the channel R_{ch} and membrane R_m resistances,

$$R_{tot} = 2R_m + R_{ch}, \tag{7.7}$$

assuming that R_m is independent of concentration. The resistances are given by

$$R_{ch} = \frac{w_{ch}}{D} \tag{7.8}$$

$$R_m = \frac{w_m}{D_m}, \tag{7.9}$$

with channel width w_{ch}, membrane width w_m, bulk diffusivity D, and membrane diffusivity D_m. Near the center of the membranes, the concentration profile can be assumed one dimensional, and the steady profile is then

$$c(x) = \frac{c_L + c_R}{2} + \frac{R_{ch}}{R_{ch} + 2R_m}(c_R - c_L)\frac{x}{w_{ch}} \tag{7.10}$$

where c_L and c_R are the concentrations in the rapidly flowing left and right channel, respectively.

The effective membrane diffusivity for NaCl in PEG-DA membranes can be found in literature (2.6x10^{-10} m^2/s, or $D/D_m = 6.2$, noting that this measurement was performed at 35 mM NaCl and using a slightly longer 13 monomer PEG chain [Sagle et al., 2009], but we assume it will serve as an adequate first approximation).

In ethanol-water solutions, the diffusivity in PEG-DA gels is not available in literature. An estimate for this value is derived by assuming that both NaCl and ethanol diffusion obey the equation [Cussler, 1997],

$$D_m = \frac{\epsilon}{\tau} D \tag{7.11}$$

with void fraction ϵ and tortuosity τ. ϵ and τ are assumed to be independent of species such that D/D_m is assumed to be the same for ethanol and NaCl. Although the void volume may be slightly higher for the uncharged, smaller ethanol molecules, this assumption serves our purposes of calculating a first approximation of the mobility.

7.3 Device fabrication

A 3-channel device was used to impose concentration gradients across colloidal solutions (fig. 7.2a). The channels were fabricated in microfluidic stickers devices [Bartolo et al., 2008] as described previously. To aid in hydrogel fabrication, the channel hydraulic resistances were matched [Bruus, 2007] which prevented PEG-DA solution from building up in unequal amounts in the device inlets, causing stray hydrostatic flows during crosslinking. The dimensions of each of the three channels were 1 cm x 150 μm x 10 μm.

Hydrogels were prepared using a modified procedure to reduce flow velocity through the hydrogel. The standard procedure results in flows of $\mathcal{O}(1\ \mu\text{m/s})$ through the hydrogel (calculated from Darcy permeabilities in Table 5.1), which must be reduced to measure diffusiophoresis velocities of similar magnitude. Flow through the hydrogel can be reduced by decreasing the Darcy permeability, increasing the width, or decreasing the pressure drop. Freshly prepared PEG_M-diacrylate (PEG-DA, $M = 400$ g/mol, Polysciencies Inc.) were mixed using 95% v/v PEG-DA and 5% v/v photoinitiator (2-hydroxy-2-methylpropiophenone, Sigma Aldrich). The UV lamp was set to 30 mW/cm^2 (measured at an empty objective slot). 500 μm wide photomask slits were inserted into the microscope and aligned as described previously. The PEG-DA solution was injected until

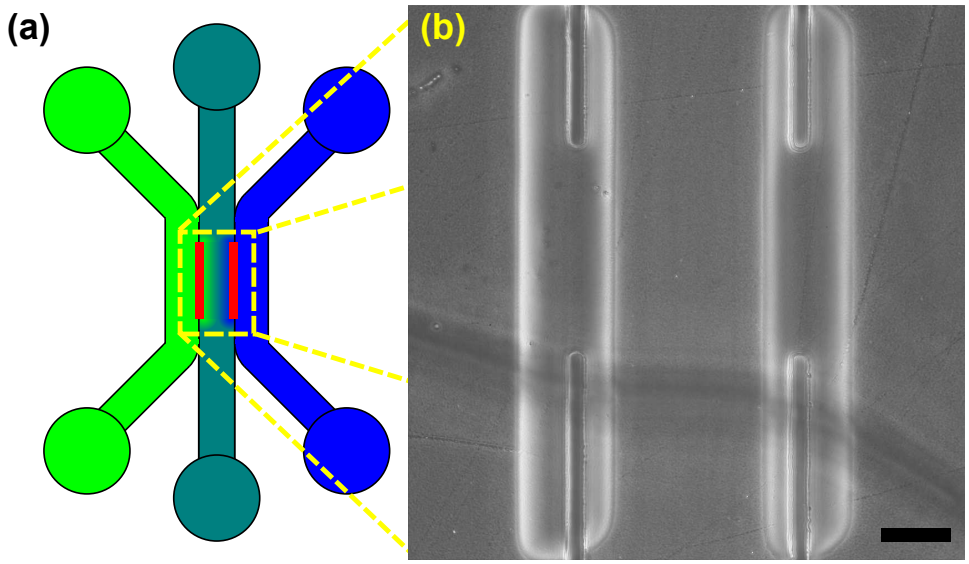

Figure 7.2: **(a)** A 3-channel device is used to impose gradients, with hydrogel membranes between channels. Credit: Craig D. Angulo for aiding device design. **(b)** Local PEG-DA hydrogel membranes are used to provide barriers to flow, while enabling diffusion of solute. (Phase contrast, scale bar: 50 μm.)

NOA-81 channels were filled, then the syringe was disconnected and 2 minutes were allowed for flows to relax. A 40 ms exposure was then used for each hydrogel. Finally, the channels were rinsed with DI water for at least 5 minutes. The procedure resulted in hydrogels that were 70-100 μm wide (fig. 7.2b).

7.4 Experimental method

Figure 7.3 summarizes the experimental setup. Experiments were performed using an inverted microscope (Nikon TE2000U). The main experimental challenge

is to rapidly stop flow in the center channel (in order to initialize the gradient). To accomplish this,the inlet and outlet tubing must be brought to exactly the same hydrostatic pressure without introducing bubbles into the tubing. Bubbles also must be fully eliminated from the center channel to avoid flows driven by capillary pressure.

Solutions were prepared and placed in vials with septa. The center solution contained 0.1wt% 1 μm diameter fluorescent particles (Bangs Labs FS03F). To control the pressure of the vials, tubing was connected from precision air pressure regulators with digital pressure gauges. The septum was punctured with syringe needles, which were connected with Luer Lock connections to tubing. The center channel inlet tubing had a metal pin inserted in the middle, where the tubing could be easily removed.

Initially, channels were filled by pressurizing each inlet to 500 mbar (fig. 7.3a). After filling the middle channel, the middle channel was checked for bubbles, which tended to stick at the low-pressure outlet of the microchannel. If bubbles were present, the pressure at the middle channel inlet was increased to 1 bar and the outlet tubing was pinched shut with a tweezers to bring the entire channel to high pressure. The tubing was held shut until the bubbles dissolved, which could take several minutes.

After the outlet tubing had been filled, it was placed into a beaker reservoir containing the same buffer solution as the center channel. Then, the metal pin in the inlet tube was submerged in the beaker reservoir. The pressure supply to the center channel was decreased to 20 mbar and the pressure supply to the outer channels was decreased to 150 mbar. The focus was adjusted to the center of the channel using a 20x ELWD objective (NA=0.45). The video recording could then be started and the metal pin was removed from the inlet tubing while the tubing was submerged underwater (fig. 7.3b). The pressure was then turned off to the center channel vial to prevent leakage. Flow velocity along the center channel could typically be reduced to 0.1-2 μm/s using this method.

7.5 Data recording and analysis

Images were recorded using an Andor iXon 885 fluorescence camera. In each experiment, videos were recorded with 0.1 second exposure times for 100 seconds. The recording was started just prior to stopping the flow and the tubing was . Fig. 7.4a shows a superposed image of the motion of colloidal particles under an ethanol-water gradient.

Micro-Particle Image Velocimetry (μ-PIV) was used to measure the velocity profile from the recorded image sequences (fig. 7.4b). The depth of correlation was

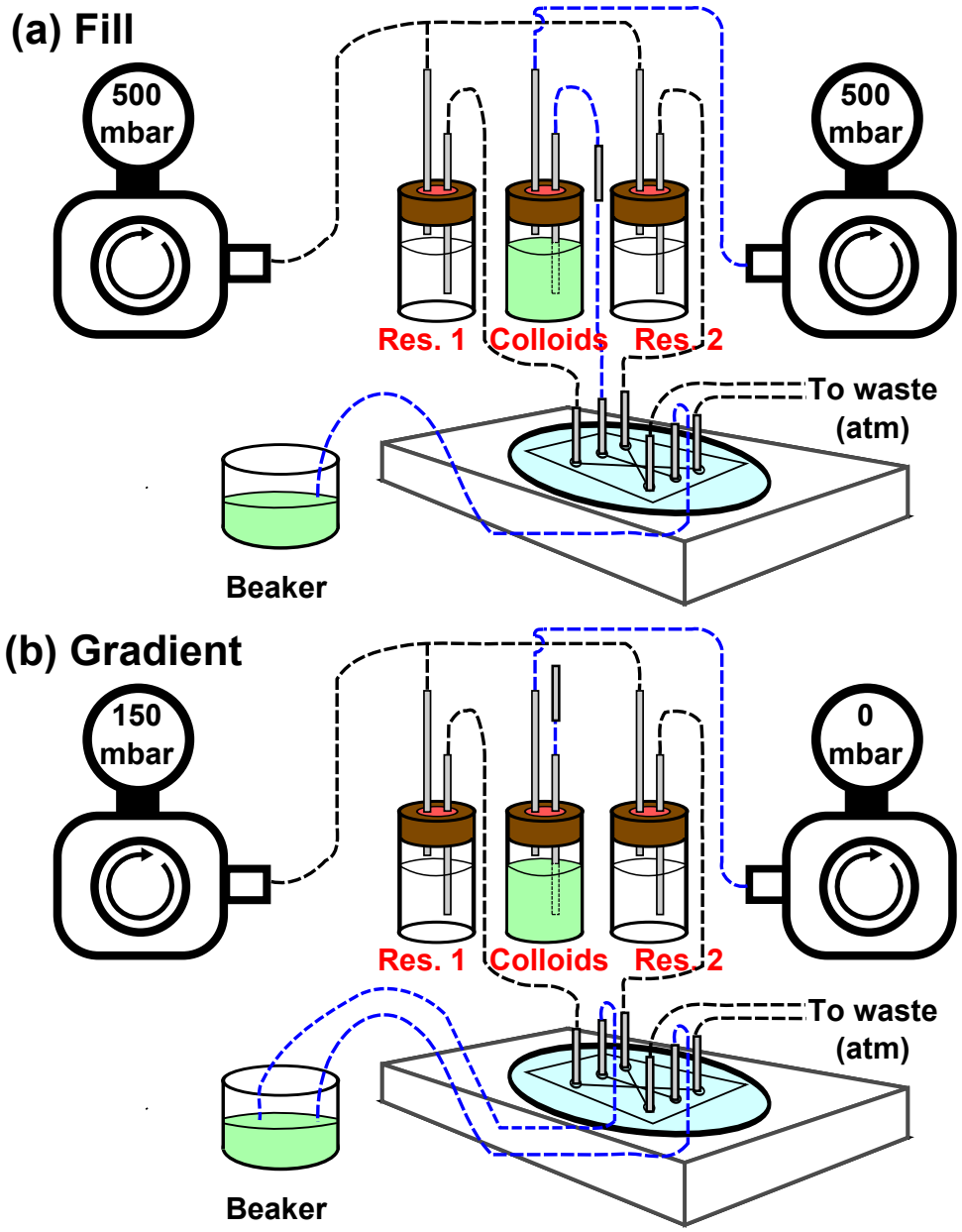

Figure 7.3: **(a)** Channels are filled by pressurizing sealed vials connected to each of the three channels. **(b)** Flow is quickly stopped in the center channel by dropping the inlet and outlet tubing into an external beaker. To accomplish this, the inlet tubing for the central channel is submerged in the beaker and disconnected from a metal pin connecting it to the source vial tubing. Flow is maintained in the outer channels, setting up a gradient across the center channel that causes diffusiophoresis of the colloids.

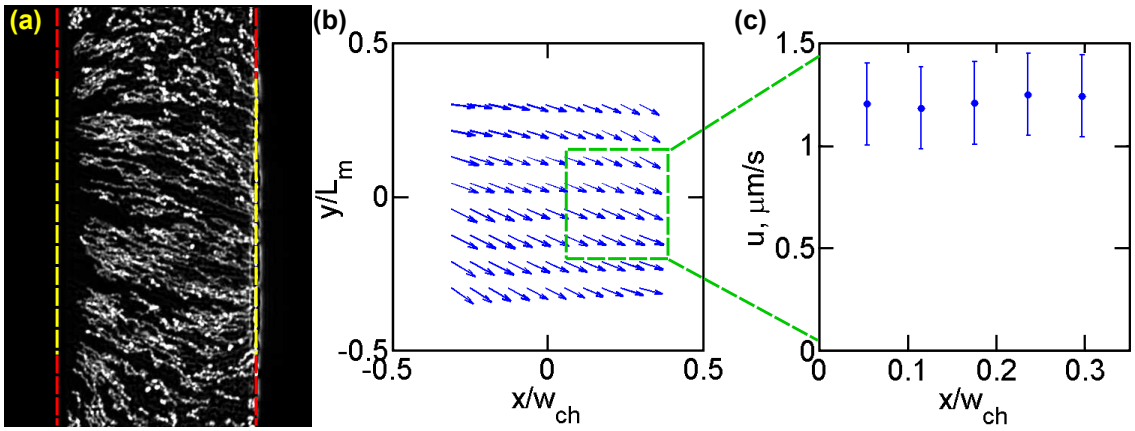

Figure 7.4: **(a)** After the experimental videos of solvophoresis have been recorded, the region between the hydrogels is selected for PIV analysis. The algorithm is run until particles are halfway across the channel. **(b)** A typical velocity field computed by PIV. The green box shows the region selected for further analysis. **(c)** The velocity is averaged in y and plotted along the gradient.

10 μm [Raffel et al., 2007]. The steady velocity profile is desired, but the movie contains a brief transient immediately after flow stoppage. PIV was performed only on the frames at least 5 seconds after flow stoppage. The initial frame was chosen by this method, while the final frame was chosen as the frame when beads became depleted up to $x = 0$. This allowed further analysis to be performed on the channel half where beads were steadily present ($x > 0$ in fig. 7.4). A steady profile was confirmed by plotting the profile for various earlier and later increments. The channel was broken into 64x128 pixel interrogation regions with 75% overlap. An average image was subtracted from each image before performing the correlation. The resulting velocity field was averaged over the middle four points in y, giving an average profile in x (fig. 7.4c).

7.5.1 Reproducibility of velocity measurements

Reproducibility experiments show that variation can occur between runs. Run-to-run reproducibility was determined by repeating three successive stop-flow experiments each for 5/2.5/0M ethanol (in water), followed by 17.1/14.6/12.1M ethanol (in water). These experiments were designed to give an estimate of the reproducibility at both high water and high ethanol content. However, another question is whether the ethanol affects the hydrogel properties. To test this, a third data set subsequently gathered, again at 5/2.5/0M ethanol and in the same device. Table 7.1 shows the results of this experiment.

Sequence	EtOH Concentrations	Average velocity (μm/s)	2σ (μm/s)
1	5M/2.5M/0M	1.4	0.1
2	17.1M/14.6M/12.1M	0.9	0.1
3	5M/2.5M/0M	1.5	0.1

Table 7.1: Run-to-run reproducibility of solvophoresis experiments.

Although the small change in velocity between the experiments in Sequence 1 and 3 was within the error, it raised the question of whether the velocity was changing due to exposure to ethanol. To further investigate this, a single run was performed at 5/2.5/0M ethanol at the beginning and end of a full day of experiments, in which various ethanol solutions were flowed in and out of the device over a full day. The average measured velocities were 1.4 $\pm$ 0.1 and 1.6 $\pm$

0.1 μm/s. This observation of a 10-20% higher solvophoretic velocity after a full day of experiments was confirmed several times in ethanol experiments. This is most likely caused by a higher ethanol diffusivity within the hydrogel caused by slow PEG-DA dissolution in ethanol.

Brownian motion of the particles does not contribute significant measurement noise in this case. This can be seen by calculating the relative error ϵ in velocity u from Brownian noise using the equation [Raffel et al., 2007]

$$\epsilon = \sqrt{\frac{2D}{MN\Delta t}} = \sqrt{\frac{2k_BT}{3\pi\eta d_p MN\Delta t}} \tag{7.12}$$

with particle diffusivity D, number of frames M, number of particles per interrogation region N, particle diameter d_p, and time between images Δt. In these experiments, insignificant Brownian error was present ($\epsilon \sim 10^{-7}$).

7.6 Results and discussion

The goal of the experiments is to determine the dependence of the solvophoretic velocity on the various experimental parameters, including concentration and gradient strength. However, in order to validate the experimental system, the velocity under NaCl gradients was first investigated.

7.6.1 Salt diffusiophoresis: NaCl gradients

Fig. 7.5a shows the steady velocities measured for NaCl gradients. The middle channel concentration and gradient strength were varied between c_{mid}=0.5-10 mM and $\Delta c = c_R - c_L$=1-20mM. The measured velocities span a range of -0.2 to -0.8 μm/s and were directed toward higher NaCl concentration in the left channel. The velocity profiles are nearly uniform across the channel; at the lowest NaCl concentrations, the velocity varied by up to 0.1 μm/s across the channel. This uniformity shows that the concentration across the channels is relatively constant, which is expected when $R_m \gg R_{ch}$. A general trend of higher velocity at lower concentration and higher gradient strength is clear.

The diffusiophoretic velocity for salt gradients is expected to obey eqn 7.5, giving

$$u = D_{DP} \nabla \ln c = D_{DP} \frac{\nabla c}{c}, \tag{7.13}$$

where D_{DP} is the diffusiophoretic mobility, including both the electrophoretic and chemiphoretic contributions [Palacci et al., 2012].

We first investigate whether our experimental system detects this trend. Since the velocity is expected to depend on two variables, c and ∇c, our strategy will be to scale by ∇c in order to determine the c dependence. A gradient-independent

mobility is defined,

$$D_C = -\frac{u}{\nabla c}. \tag{7.14}$$

If the velocity measurements all collapse onto a single D_C at a given c, the gradient proportionality is accurate. The concentration dependence of D_C can then be used to find an overal equation for $u\left(c, \nabla c\right)$. For salt diffusiophoresis, $D_C \sim c^{-1}$ is expected from eqn. 7.13.

Fig. 7.5b shows the mobility D_C for each data point plotted against the concentration in the channel, calculated from eqn 7.10. Clearly, the velocity is proportional to the gradient, as shown by the data at 5 mM and 10 mM for multiple gradient strengths. In addition, the data does follow a clear trend in concentration which is well described by a power law fit, $D_C \sim c^{-0.96\pm0.04}$. The logarithmic dependence of u is verified,

$$D_C = \frac{D_{DP}}{c}, \tag{7.15}$$

where D_{DP} is independent of concentration.

Although all the data sets show a single-valued average magnitude of D_C, the low concentration data sets slope in the opposite direction from the line of best fit. While the average D_C of a given experiment can be predicted by fitting the data to eqn.7.15, the velocity profiles within that experiment cannot be explained by the same equation at low concentration. This may be because of electrostatic

interactions between beads or channel walls, which are expected to be longer ranged at low salt concentration.

7.6.2 Solvophoresis: ethanol gradients

Next, the experimental system was used to measure solvophoretic velocities, where the concentration dependence was previously unknown. The concentration of ethanol was varied between c_{mid}=2.5-14.6 M (5-70 mol% EtOH) in water, and the gradient strength was either Δc=5 or 10 M. Higher ethanol concentration was on the left and migration was observed to the right, toward lower ethanol concentration. Fig. 7.5c shows the velocity profiles measured for each combination of c_{mid} and Δc. The measured velocities are 0.5-2.0 μm/s and the profiles are now nonuniform across the channel. A trend of higher velocity for larger gradients and lower ethanol concentration was observed.

To find how the velocity depends on concentration, initially the data was analyzed using eqn. 7.14 to plot D_C vs c. However, a more clear relation was obtained when plotting a mole fraction dependent mobility,

$$D_X = \frac{u}{\nabla X}. \tag{7.16}$$

Fig. 7.5d shows the mobilities computed using eqn. 7.16. Each data set falls on to the same line, showing that the gradient proportionality is correct. A power

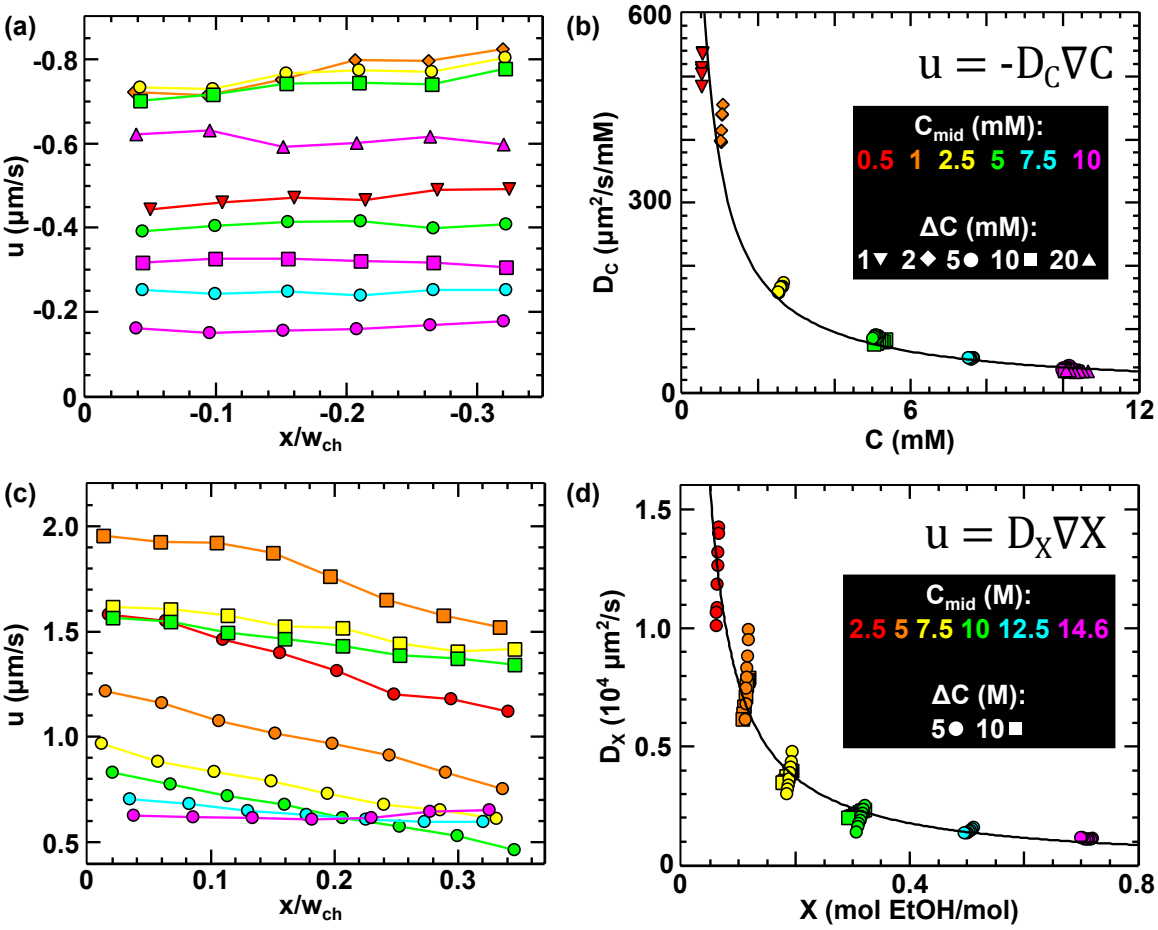

Figure 7.5: **(a)** Velocity profiles across the microchannel over a range of concentrations from 0.5-10mM and Δc=1-20mM. **(b)** Mobility vs NaCl concentration. **(c)** Velocity profiles over a range of ethanol concentrations and two different gradient strengths. **(d)** Mobility is calculated from the mole fraction gradient of ethanol. The average velocity per data set follows a trend in mole fraction, but the spatial dependence of the velocity cannot be explained by that trend.

law fit of this data now gives $D_X \sim X^{-1.06\pm0.06}$. The solvophoretic velocity can therefore be described by

$$u = D_{SP} \nabla \ln X \tag{7.17}$$

where

$$D_{SP} = X D_X. \tag{7.18}$$

Although eqn. 7.17 predicts the average velocity for a given experiment, the equation could not predict the velocity profiles. The data slopes in the opposite direction of the fit line, just as was observed at low ionic strengths for NaCl. This could be due to electrostatic interactions because of the small ionic strength of the ethanol-water solutions.

To verify that the average velocity follows the above trends, D_X and D_C averaged for each experiment are plotted against the middle channel concentration X and C (fig. 7.6a). The slope of the linear fits is similar to that obtained for the power-law fit to all the data, as expected. The large error bars in the ethanol mobility come mainly from the large spread in velocity for a given experiment, however, the trend in average mobility is clear.

Using eqns. 7.13 and 7.17, the mobilities D_{DP} and D_{SP} can be measured from the slope of u vs. $\nabla \ln c$ and $\nabla \ln X$, (Fig. 7.6b). The measured mobilities are shown in Table 7.2.

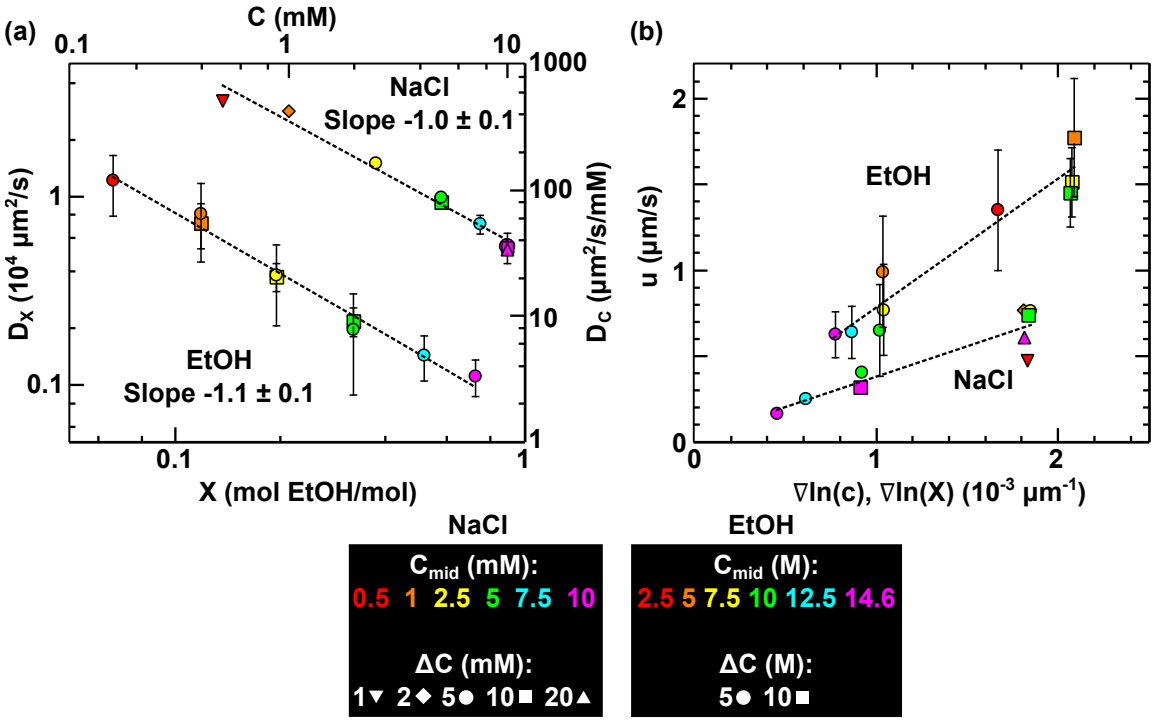

Figure 7.6: **(a)** Scaling of mobilities with concentration for NaCl and ethanol. **(b)** Velocity is plotted against combined concentration and gradient dependence. The slope of the lines is the mobility.

Quantity measured	Species	Colloid	Mobility (μm^2/s)
D_{DP}	NaCl	1 μm PS	350 $\pm$ 60
D_{SP}	Ethanol-water	1 μm PS	760 $\pm$ 80

Table 7.2: Mobilities from diffusiophoresis and solvophoresis experiments.

Experiments were also performed at larger ethanol gradients. The experiments resulted in qualitatively different behavior which appeared to be convective rather than phoretic, and is therefore excluded from the mobility measurements. Images of these experiments are shown in Appendix C.

7.7 Conclusion

The experimental system allows direct visualization of diffusiophoretic migration under diverse chemical gradients. This was applied to measure the velocity under NaCl and ethanol concentration gradients, and compute the resulting mobility. The diffusiophoretic velocity in NaCl gradients showed a $u \sim \nabla \ln c$ dependence, as expected from theory and literature. The solvophoretic velocity was found to obey a $u \sim \nabla \ln X$ dependence.

The velocity profiles of solvophoresis could not be explained by the general concentration dependence. This could be because of electrostatic interactions. Addition of salt to each solution could be used to decrease the electrostatic range

of interaction, but will also set up salt gradients via multicomponent diffusion. Multicomponent diffusion could be eliminated if salt concentrations are set at equilibrium (equal activity) in all three channels. However, in real world systems, salt can easily be present at $\mathcal{O}$(mM) concentrations and salt gradients could enhance (or, sometimes, decrease) the solvophoretic velocity.

The experimental system proposed here could be used to measure diffusiophoretic velocities in a variety of solutions. For example, preliminary experiments have demonstrated the presence of solvophoresis in other alcohol gradients besides ethanol, including isopropanol and glycerol. The dependence on particle size and surface chemistry could also be investigated. Many mechanisms could underly solvophoresis: hydration, Van der Waals forces, or multicomponent diffusion of salt. The original proposal was that hydration gradients along the colloid surface led to the motion [Kosmulski and Matuevi, 1992], but clearly other forces could play a role in multicomponent mixtures, especially salt gradients. This experimental work has unveiled the functional dependence of the solvophoretic velocity on concentration and gradient strength, which was enabled by the improved accuracy afforded from direct visualization. The groundwork has been laid for future studies using salt, surfactant, polymers, and other colloids to develop an enhanced understanding of solvophoresis.

Chapter 8

Conclusion

In this thesis, I described two microfluidic tools that enable enhanced local sample transport, and demonstrated their use in several ways. I started by describing the ICEO micropump. Prior to this work, ICEO had been used only to drive flows locally within microfluidic channels, *e.g.* for mixing solutions. I demonstrated the first chip-scale pumping using ICEO flow. The work presented here opens the way to use of ICEO for on-chip fluid handling, especially for electrolytes. Optimization routes were suggested, which could be pursued by if desired.

Hydrogel Membrane Micro-windows (HMMs) were also described. Thin, local membranes within microfluidic channels enable rapid diffusive delivery to a sample, local concentration gradients, and local electric currents. These three simple capabilities greatly enhance microscale solution control, and should enable new

applications in colloids, soft matter, biology, and materials fabrication. A key feature of these membranes is the rapid and robust fabrication method, which allows membranes to be fabricated in under 30 minutes. Another key feature is their thin dimension, which allows fast diffusion times and low electrical and diffusive resistance. The HMMs can be combined with PDMS microvalves, as in Chapter 6, to allow rapid solution switching.

Finally, the local gradient capability of HMMs was applied to study diffusiophoretic and solvophoretic motion of colloidal particles. NaCl gradients were shown to obey a $u \sim \nabla \ln c$ scaling, as expected from theory and experimental literature. The solvophoretic velocity was found to obey the same functional form, but depends on the mole fraction X, $u \sim \nabla \ln X$. This relation was not previously known. The work shows that solvophoresis is present both at large gradient strengths and at large water concentrations, but is not strong at ethanol-rich concentrations. This is the first quantitative study of the solvophoretic mobility and first direct visualization, and opens the way for future investigations using other solvents, particles, and more complex mixtures.

Bibliography

[Abcassis et al., 2008] Abcassis, B., Cottin-Bizonne, C., Ybert, C., Ajdari, A., and Bocquet, L. (2008). Boosting migration of large particles by solute contrasts. *Nature materials*, 7(10):785789.

[Abcassis et al., 2009] Abcassis, B., Cottin-Bizonne, C., Ybert, C., Ajdari, A., and Bocquet, L. (2009). Osmotic manipulation of particles for microfluidic applications. *New Journal of Physics*, 11(7):075022.

[Addae-Mensah et al., 2010] Addae-Mensah, K. A., Cheung, Y. K., Fekete, V., Rendely, M. S., and Sia, S. K. (2010). Actuation of elastomeric microvalves in point-of-care settings using handheld, battery-powered instrumentation. *Lab on a Chip*, 10(12):16181622.

[Ahmed et al., 2013] Ahmed, D., Chan, C. Y., Lin, S.-C. S., Muddana, H. S., Nama, N., Benkovic, S. J., and Jun Huang, T. (2013). Tunable, pulsatile chemical gradient generation via acoustically driven oscillating bubbles. *Lab on a Chip*, 13(3):328.

[Ajdari, 2000] Ajdari, A. (2000). Pumping liquids using asymmetric electrode arrays. *Physical Review E*, 61(1):4548.

[Anderson, 1989] Anderson, J. L. (1989). Colloid transport by interfacial forces. *Annual Review of Fluid Mechanics*, 21(1):6199.

[Anderson et al., 1982a] Anderson, J. L., Lowell, M. E., and Prieve, D. C. (1982a). Motion of a particle generated by chemical gradients part 1. non-electrolytes. *Journal of Fluid Mechanics*, 117(1):107121.

[Anderson et al., 1982b] Anderson, J. L., Lowell, M. E., and Prieve, D. C. (1982b). Motion of a particle generated by chemical gradients. part 1. non-electrolytes. *J. Fluid Mech*, 117:107121.

[Anderson and Prieve, 1991] Anderson, J. L. and Prieve, D. C. (1991). Diffusiophoresis caused by gradients of strongly adsorbing solutes. *Langmuir*, 7(2):403406.

[Atencia et al., 2009] Atencia, J., Morrow, J., and Locascio, L. E. (2009). The microfluidic palette: A diffusive gradient generator with spatio-temporal control. *Lab on a Chip*, 9(18):2707.

[Balagadde et al., 2005] Balagadde, F. K., You, L., Hansen, C. L., Arnold, F. H., and Quake, S. R. (2005). Long-term monitoring of bacteria undergoing programmed population control in a microchemostat. *Science*, 309(5731):137140.

[Bartolo et al., 2008] Bartolo, D., Degr, G., Nghe, P., and Studer, V. (2008). Microfluidic stickers. *Lab Chip*, 8(2):274279.

[Bazant and Ben, 2006] Bazant, M. Z. and Ben, Y. (2006). Theoretical prediction of fast 3D AC electro-osmotic pumps. *Lab on a Chip*, 6(11):14551461.

[Bazant et al., 2009a] Bazant, M. Z., Kilic, M. S., Storey, B. D., and Ajdari, A. (2009a). Nonlinear electrokinetics at large voltages. *New Journal of Physics*, 11(7):075016.

[Bazant et al., 2009b] Bazant, M. Z., Kilic, M. S., Storey, B. D., and Ajdari, A. (2009b). Towards an understanding of induced-charge electrokinetics at large applied voltages in concentrated solutions. *Advances in colloid and interface science*, 152(1):4888.

[Bazant and Squires, 2004] Bazant, M. Z. and Squires, T. M. (2004). Induced-charge electrokinetic phenomena: theory and microfluidic applications. *Physical Review Letters*, 92(6):66101.

[Bazant and Squires, 2010] Bazant, M. Z. and Squires, T. M. (2010). Induced-charge electrokinetic phenomena. *Current Opinion in Colloid & Interface Science*, 15(3):203213.

[Beebe et al., 2000] Beebe, D. J., Moore, J. S., Bauer, J. M., Yu, Q., Liu, R. H., Devadoss, C., and Jo, B.-H. (2000). Functional hydrogel structures for autonomous flow control inside microfluidic channels. *Nature*, 404(6778):588590.

[Brady, 2011] Brady, J. F. (2011). Particle motion driven by solute gradients with application to autonomous motion: continuum and colloidal perspectives. *Journal of Fluid Mechanics*, 667:216259.

[Brask et al., 2005] Brask, A., Kutter, J. P., and Bruus, H. (2005). Long-term stable electroosmotic pump with ion exchange membranes. *Lab on a Chip*, 5(7):730738.

[Brask et al., 2006] Brask, A., Snakenborg, D., Kutter, J. P., and Bruus, H. (2006). AC electroosmotic pump with bubble-free palladium electrodes and rectifying polymer membrane valves. *Lab on a Chip*, 6(2):280288.

[Brown et al., 2000] Brown, A. B. D., Smith, C. G., and Rennie, A. R. (2000). Pumping of water with ac electric fields applied to asymmetric pairs of microelectrodes. *Physical Review E*, 63(1):016305.

[Bruus, 2007] Bruus, H. (2007). *Theoretical microfluidics*, volume 18. Oxford University Press, USA.

[Cheng et al., 2007] Cheng, S.-Y., Heilman, S., Wasserman, M., Archer, S., Shuler, M. L., and Wu, M. (2007). A hydrogel-based microfluidic device for the studies of directed cell migration. *Lab Chip*, 7(6):763769.

[Chin et al., 2012] Chin, C. D., Linder, V., and Sia, S. K. (2012). Commercialization of microfluidic point-of-care diagnostic devices. *Lab on a Chip*, 12(12):21182134.

[Choi et al., 2012a] Choi, E., Chang, H.-k., Young Lim, C., Kim, T., and Park, J. (2012a). Concentration gradient generation of multiple chemicals using spatially controlled self-assembly of particles in microchannels. *Lab on a Chip*, 12(20):3968.

[Choi et al., 2012b] Choi, N., Lee, K., Lim, D. W., Lee, E. K., Chang, S.-I., Oh, K. W., and Choo, J. (2012b). Simultaneous detection of duplex DNA oligonucleotides using a SERS-based micro-network gradient chip. *Lab on a Chip*, 12(24):5160–5167.

[Chou et al., 2001] Chou, H. P., Unger, M. A., and Quake, S. R. (2001). A microfabricated rotary pump. *Biomedical Microdevices*, 3(4):323330.

[Chun et al., 2005] Chun, H., Chung, T. D., and Kim, H. C. (2005). Cytometry and velocimetry on a microfluidic chip using polyelectrolytic salt bridges. *Analytical chemistry*, 77(8):24902495.

[Chun et al., 2010] Chun, H., Chung, T. D., and Ramsey, J. M. (2010). High yield sample preconcentration using a highly ion-conductive charge-selective polymer. *Analytical chemistry*, 82(14):62876292.

[Cooksey and Atencia, 2014] Cooksey, G. A. and Atencia, J. (2014). Pneumatic valves in folded 2D and 3D fluidic devices made from plastic films and tapes. *Lab on a Chip*, 14(10):1665–1668.

[Crane et al., 2010] Crane, M. M., Chung, K., Stirman, J., and Lu, H. (2010). Microfluidics-enabled phenotyping, imaging, and screening of multicellular organisms. *Lab Chip*, 10(12):15091517.

[Cuchiara et al., 2010] Cuchiara, M. P., Allen, A. C., Chen, T. M., Miller, J. S., and West, J. L. (2010). Multilayer microfluidic PEGDA hydrogels. *Biomaterials*, 31(21):5491–5497.

[Cussler, 1997] Cussler, E. L. (1997). *Diffusion: Mass transfer in fluid systems*. Cambridge university press.

[Cyster, 1999] Cyster, J. G. (1999). Chemokines and cell migration in secondary lymphoid organs. *Science*, 286(5447):20982102.

[De Jong et al., 2006] De Jong, J., Lammertink, R. G. H., and Wessling, M. (2006). Membranes and microfluidics: a review. *Lab Chip*, 6(9):11251139.

[Dendukuri et al., 2007] Dendukuri, D., Gu, S. S., Pregibon, D. C., Hatton, T. A., and Doyle, P. S. (2007). Stop-flow lithography in a microfluidic device. *Lab Chip*, 7(7):818828.

[Dendukuri et al., 2008] Dendukuri, D., Panda, P., Haghgooie, R., Kim, J. M., Hatton, T. A., and Doyle, P. S. (2008). Modeling of oxygen-inhibited free radical photopolymerization in a PDMS microfluidic device. *Macromolecules*, 41(22):85478556.

[Dendukuri et al., 2006] Dendukuri, D., Pregibon, D. C., Collins, J., Hatton, T. A., and Doyle, P. S. (2006). Continuous-flow lithography for high-throughput microparticle synthesis. *Nature materials*, 5(5):365369.

[Dendukuri et al., 2005] Dendukuri, D., Tsoi, K., Hatton, T. A., and Doyle, P. S. (2005). Controlled synthesis of nonspherical microparticles using microfluidics. *Langmuir*, 21(6):21132116.

[Derjaguin et al., 1947] Derjaguin, B. V., Sidorenkov, G. P., Zubashchenkov, E. A., and Kiseleva, E. V. (1947). Kinetic phenomena in boundary films of liquids. *Kolloidn. Zh*, 9:33547.

[Deryaguin et al., 1961] Deryaguin, B. V., Dukhin, S. S., and Korotkova, A. A. (1961). Diffusiophoresis in electrolyte solutions and its role in the mechanism of film formation from rubber latexes by the method of ionic deposition. *Kolloidn. Zh*, 23:53.

[Dhopeshwarkar et al., 2005] Dhopeshwarkar, R., Sun, L., and Crooks, R. M. (2005). Electrokinetic concentration enrichment within a microfluidic device using a hydrogel microplug. *Lab Chip*, 5(10):11481154.

[Diao et al., 2006] Diao, J., Young, L., Kim, S., Fogarty, E. A., Heilman, S. M., Zhou, P., Shuler, M. L., Wu, M., and DeLisa, M. P. (2006). A three-channel microfluidic device for generating static linear gradients and its application to the quantitative analysis of bacterial chemotaxis. *Lab on a Chip*, 6(3):381.

[Dittrich and Manz, 2006] Dittrich, P. S. and Manz, A. (2006). Lab-on-a-chip: microfluidics in drug discovery. *Nature Reviews Drug Discovery*, 5(3):210218.

[Dormann and Weijer, 2003] Dormann, D. and Weijer, C. J. (2003). Chemotactic cell movement during development. *Current opinion in genetics & development*, 13(4):358364.

[Du et al., 2009] Du, W., Li, L., Nichols, K. P., and Ismagilov, R. F. (2009). SlipChip. *Lab Chip*, 9(16):22862292.

[Dubrulle and Pourqui, 2004] Dubrulle, J. and Pourqui, O. (2004). fgf8 mRNA decay establishes a gradient that couples axial elongation to patterning in the vertebrate embryo. *Nature*, 427(6973):419422.

[Duffy et al., 1998] Duffy, D. C., McDonald, J. C., Schueller, O. J. A., and Whitesides, G. M. (1998). Rapid prototyping of microfluidic systems in poly(dimethylsiloxane). *Analytical Chemistry*, 70(23):4974–4984.

[Duhr and Braun, 2006] Duhr, S. and Braun, D. (2006). Why molecules move along a temperature gradient. *Proceedings of the National Academy of Sciences*, 103(52):1967819682.

[Dydek et al., 2012] Dydek, E. V., Petersen, M. V., Nocera, D. G., and Jensen, K. F. (2012). Realization of a salt bridge-free microfluidic reference electrode. *Lab on a Chip*, 12(8):1431.

[Ebel et al., 1988] Ebel, J. P., Anderson, J. L., and Prieve, D. C. (1988). Diffusiophoresis of latex particles in electrolyte gradients. *Langmuir*, 4(2):396406.

[Eckstein et al., 2009] Eckstein, Y., Yossifon, G., Seifert, A., and Miloh, T. (2009). Nonlinear electrokinetic phenomena around nearly insulated sharp tips in microflows. *Journal of colloid and interface science*, 338(1):243249.

[Eijkel, 2007] Eijkel, J. (2007). Chip-based HPLC: the quest for the perfect column. *Lab on a Chip*, 7(7):815817.

[Farlow, 1993] Farlow, S. J. (1993). *Partial differential equations for scientists and engineers*. Dover Publications.

[Fox et al., 2006] Fox, M. B., Esveld, D. C., Valero, A., Luttge, R., Mastwijk, H. C., Bartels, P. V., Van Den Berg, A., and Boom, R. M. (2006). Electroporation of cells in microfluidic devices: a review. *Analytical and bioanalytical chemistry*, 385(3):474485.

[Frank and Tay, 2013] Frank, T. and Tay, S. (2013). Flow-switching allows independently programmable, extremely stable, high-throughput diffusion-based gradients. *Lab on a Chip*, 13(7):1273.

[Galas et al., 2009] Galas, J. C., Bartolo, D., and Studer, V. (2009). Active connectors for microfluidic drops on demand. *New Journal of Physics*, 11(7):075027.

[Gangwal et al., 2008] Gangwal, S., Cayre, O. J., Bazant, M. Z., and Velev, O. D. (2008). Induced-charge electrophoresis of metallodielectric particles. *Physical review letters*, 100(5):058302.

[Gervais et al., 2011] Gervais, L., de Rooij, N., and Delamarche, E. (2011). Microfluidic chips for point-of-care immunodiagnostics. *Advanced Materials*, 23(24):H151H176.

[Gonzalez et al., 2000] Gonzalez, A., Ramos, A., Green, N. G., Castellanos, A., and Morgan, H. (2000). Fluid flow induced by nonuniform ac electric fields in electrolytes on microelectrodes. II. a linear double-layer analysis. *Physical review E*, 61(4):4019.

[Gonzlez et al., 2006] Gonzlez, A., Ramos, A., Morgan, H., Green, N. G., and Castellanos, A. (2006). Electrothermal flows generated by alternating and rotating electric fields in microsystems. *Journal of Fluid Mechanics*, 564:415–433.

[Green et al., 2000] Green, N. G., Ramos, A., Gonzalez, A., Morgan, H., and Castellanos, A. (2000). Fluid flow induced by nonuniform ac electric fields in electrolytes on microelectrodes. i. experimental measurements. *Physical review E*, 61(4):4011.

[Green et al., 2002] Green, N. G., Ramos, A., Gonzalez, A., Morgan, H., and Castellanos, A. (2002). Fluid flow induced by nonuniform ac electric fields in electrolytes on microelectrodes. III. observation of streamlines and numerical simulation. *Physical review E*, 66(2):026305.

[Gregersen et al., 2009] Gregersen, M. M., Okkels, F., Bazant, M. Z., and Bruus, H. (2009). Topology and shape optimization of induced-charge electro-osmotic micropumps. *New Journal of Physics*, 11(7):075019.

[Groisman et al., 2003] Groisman, A., Enzelberger, M., and Quake, S. R. (2003). Microfluidic memory and control devices. *Science*, 300(5621):955–958.

[Gu et al., 2012] Gu, C., Jia, Z., Zhu, Z., He, C., Wang, W., Morgan, A., Lu, J. J., and Liu, S. (2012). Miniaturized electroosmotic pump capable of generating pressures of more than 1200 bar. *Analytical chemistry*, 84(21):96099614.

[Hansen and Quake, 2003] Hansen, C. and Quake, S. R. (2003). Microfluidics in structural biology: smaller, faster better. *Current Opinion in Structural Biology*, 13(5):538–544.

[Hansen et al., 2006] Hansen, C. L., Classen, S., Berger, J. M., and Stephen, R. (2006). A microfluidic device for kinetic optimization of protein crystallization and in situ structure determination. *Journal of the American Chemical Society*, 128(10):31423143.

[Hansen et al., 2002] Hansen, C. L., Skordalakes, E., Berger, J. M., and Quake, S. R. (2002). A robust and scalable microfluidic metering method that allows protein crystal growth by free interface diffusion. *Proceedings of the National Academy of Sciences*, 99(26):16531–16536. PMID: 12486223.

[Hansen et al., 2004] Hansen, C. L., Sommer, M. O. A., and Quake, S. R. (2004). Systematic investigation of protein phase behavior with a microfluidic formulator. *Proceedings of the National Academy of Sciences of the United States of America*, 101(40):14431–14436.

[Harnett et al., 2008] Harnett, C. K., Templeton, J., Dunphy-Guzman, K. A., Senousy, Y. M., and Kanouff, M. P. (2008). Model based design of a microfluidic mixer driven by induced charge electroosmosis. *Lab on a Chip*, 8(4):565572.

[Hatch et al., 2006] Hatch, A. V., Herr, A. E., Throckmorton, D. J., Brennan, J. S., and Singh, A. K. (2006). Integrated preconcentration SDSPAGE of proteins in microchips using photopatterned cross-linked polyacrylamide gels. *Analytical Chemistry*, 78(14):4976–4984.

[Helgeson et al., 2011] Helgeson, M. E., Chapin, S. C., and Doyle, P. S. (2011). Hydrogel microparticles from lithographic processes: Novel materials for fundamental and applied colloid science. *Current Opinion in Colloid & Interface Science*, 16(2):106–117.

[Herr and Singh, 2004] Herr, A. E. and Singh, A. K. (2004). Photopolymerized cross-linked polyacrylamide gels for on-chip protein sizing. *Analytical chemistry*, 76(16):47274733.

[Hersen et al., 2008] Hersen, P., McClean, M. N., Mahadevan, L., and Ramanathan, S. (2008). Signal processing by the HOG MAP kinase pathway. *Proceedings of the National Academy of Sciences*, 105(20):7165–7170.

[Hjgaard Olesen et al., 2010] Hjgaard Olesen, L., Bazant, M. Z., and Bruus, H. (2010). Strongly nonlinear dynamics of electrolytes in large ac voltages. *Physical Review E*, 82(1):011501.

[Hoffman, 2012] Hoffman, A. S. (2012). Hydrogels for biomedical applications. *Advanced drug delivery reviews*.

[Hoyle and Bowman, 2010] Hoyle, C. E. and Bowman, C. N. (2010). ThiolEne click chemistry. *Angewandte Chemie International Edition*, 49(9):15401573.

[Huang et al., 2009] Huang, C. C., Bazant, M. Z., and Thorsen, T. (2009). Ultrafast high-pressure AC electro-osmotic pumps for portable biomedical microfluidics. *Lab Chip*, 10(1):8085.

[Huh et al., 2010] Huh, D., Matthews, B. D., Mammoto, A., Montoya-Zavala, M., Hsin, H. Y., and Ingber, D. E. (2010). Reconstituting organ-level lung functions on a chip. *Science*, 328(5986):1662–1668. PMID: 20576885.

[Ibele et al., 2009] Ibele, M., Mallouk, T. E., and Sen, A. (2009). Schooling behavior of light-powered autonomous micromotors in water. *Angewandte Chemie International Edition*, 48(18):33083312.

[Irimia, 2010] Irimia, D. (2010). Microfluidic technologies for temporal perturbations of chemotaxis. *Annual review of biomedical engineering*, 12:259.

[Ismagilov et al., 2000] Ismagilov, R. F., Stroock, A. D., Kenis, P. J. A., Whitesides, G., and Stone, H. A. (2000). Experimental and theoretical scaling laws for transverse diffusive broadening in two-phase laminar flows in microchannels. *Applied Physics Letters*, 76(17):2376 –2378.

[Iverson and Garimella, 2008] Iverson, B. D. and Garimella, S. V. (2008). Recent advances in microscale pumping technologies: a review and evaluation. *Microfluidics and Nanofluidics*, 5(2):145174.

[Jeon et al., 2000] Jeon, N. L., Dertinger, S. K. W., Chiu, D. T., Choi, I. S., Stroock, A. D., and Whitesides, G. M. (2000). Generation of solution and surface gradients using microfluidic systems. *Langmuir*, 16(22):8311–8316.

[Kamholz et al., 1999] Kamholz, A. E., Weigl, B. H., Finlayson, B. A., and Yager, P. (1999). Quantitative analysis of molecular interaction in a microfluidic channel: the t-sensor. *Analytical Chemistry*, 71(23):5340–5347.

[Kar et al., 2014] Kar, A., Guha, R., Dani, N., Velegol, D., and Kumar, M. (2014). Particle deposition on microporous membranes can be enhanced or reduced by salt gradients. *Langmuir*.

[Keenan and Folch, 2007] Keenan, T. M. and Folch, A. (2007). Biomolecular gradients in cell culture systems. *Lab Chip*, 8(1):3457.

[Khair, 2013] Khair, A. S. (2013). Diffusiophoresis of colloidal particles in neutral solute gradients at finite pclet number. *Journal of Fluid Mechanics*, 731:6494.

[Khair and Squires, 2008] Khair, A. S. and Squires, T. M. (2008). Surprising consequences of ion conservation in electro-osmosis over a surface charge discontinuity. *Journal of Fluid Mechanics*, 615(1):323334.

[Khair and Squires, 2009] Khair, A. S. and Squires, T. M. (2009). Ion steric effects on electrophoresis of a colloidal particle. *Journal of Fluid Mechanics*, 640:343.

[Kim et al., 2012] Kim, C., Kreppenhofer, K., Kashef, J., Gradl, D., Herrmann, D., Schneider, M., Ahrens, R., Guber, A., and Wedlich, D. (2012). Diffusion- and convection-based activation of wnt/-catenin signaling in a gradient generating microfluidic chip. *Lab on a Chip*, 12(24):5186.

[Kim and Beebe, 2008] Kim, D. and Beebe, D. J. (2008). Interfacial formation of porous membranes with poly (ethylene glycol) in a microfluidic environment. *Journal of Applied Polymer Science*, 110(3):15811589.

[Kim et al., 2013] Kim, H., Jebrail, M. J., Sinha, A., Bent, Z. W., Solberg, O. D., Williams, K. P., Langevin, S. A., Renzi, R. F., Van De Vreugde, J. L., Meagher, R. J., Schoeniger, J. S., Lane, T. W., Branda, S. S., Bartsch, M. S., and Patel, K. D. (2013). A microfluidic DNA library preparation platform for next-generation sequencing. *PLoS ONE*, 8(7):e68988.

[Kim et al., 2009] Kim, K. B., Chun, H., Kim, H. C., and Chung, T. D. (2009). Red blood cell quantification microfluidic chip using polyelectrolytic gel electrodes. *Electrophoresis*, 30(9):14641469.

[Klank et al., 2002] Klank, H., Kutter, J. P., and Geschke, O. (2002). CO2-laser micromachining and back-end processing for rapid production of PMMA-based microfluidic systems. *Lab on a Chip*, 2(4):242.

[Kosmulski and Matuevi, 1992] Kosmulski, M. and Matuevi, E. (1992). Solvophoresis of latex. *Journal of colloid and interface science*, 150(1):291294.

[Kothapalli et al., 2011] Kothapalli, C. R., van Veen, E., de Valence, S., Chung, S., Zervantonakis, I. K., Gertler, F. B., and Kamm, R. D. (2011). A high-throughput microfluidic assay to study neurite response to growth factor gradients. *Lab on a Chip*, 11(3):497507.

[Kuo et al., 2003] Kuo, T.-C., Cannon, Chen, Y., Tulock, J. J., Shannon, M. A., Sweedler, J. V., and Bohn, P. W. (2003). Gateable nanofluidic interconnects for multilayered microfluidic separation systems. *Analytical Chemistry*, 75(8):1861–1867.

[Laser and Santiago, 2004] Laser, D. J. and Santiago, J. G. (2004). A review of micropumps. *Journal of micromechanics and microengineering*, 14(6):R35.

[Leal, 2007] Leal, L. G. (2007). *Advanced transport phenomena: fluid mechanics and convective transport processes*. Cambridge University Press.

[Lechnick and Shaeiwitz, 1984] Lechnick, W. J. and Shaeiwitz, J. A. (1984). Measurement of diffusiophoresis in liquids. *Journal of colloid and interface science*, 102(1):7187.

[Lechnick and Shaeiwitz, 1985] Lechnick, W. J. and Shaeiwitz, J. A. (1985). Electrolyte concentration dependence of diffusiophoresis in liquids. *Journal of Colloid and Interface Science*, 104(2):456–470.

[Levitan et al., 2005] Levitan, J. A., Devasenathipathy, S., Studer, V., Ben, Y., Thorsen, T., Squires, T. M., and Bazant, M. Z. (2005). Experimental observation of induced-charge electro-osmosis around a metal wire in a microchannel. *Colloids and Surfaces A: Physicochemical and Engineering Aspects*, 267(1):122132.

[Li et al., 2009] Li, L., Du, W., and Ismagilov, R. F. (2009). Multiparameter screening on slipchip used for nanoliter protein crystallization combining free interface diffusion and microbatch methods. *Journal of the American Chemical Society*, 132(1):112119.

[Li and Ismagilov, 2010] Li, L. and Ismagilov, R. F. (2010). Protein crystallization using microfluidic technologies based on valves, droplets, and slipchip. *Annual review of biophysics*, 39:139158.

[Lightfoot et al., 1962] Lightfoot, E. N., Cussler, E. L., and Rettig, R. L. (1962). Applicability of the stefan-maxwell equations to multicomponent diffusion in liquids. *AIChE Journal*, 8(5):708710.

[Lin and Prieve, 1983] Lin, M. M. J. and Prieve, D. C. (1983). Electromigration of latex induced by a salt gradient. *Journal of Colloid and Interface Science*, 95(2):327–339.

[Liu et al., 2009] Liu, J., Gao, D., Li, H. F., and Lin, J. M. (2009). Controlled photopolymerization of hydrogel microstructures inside microchannels for bioassays. *Lab Chip*, 9(9):13011305.

[Liu et al., 2003] Liu, J., Hansen, C., and Quake, S. R. (2003). Solving the world-to-chip interface problem with a microfluidic matrix. *Analytical Chemistry*, 75(18):47184723.

[Loman et al., 2012] Loman, N. J., Misra, R. V., Dallman, T. J., Constantinidou, C., Gharbia, S. E., Wain, J., and Pallen, M. J. (2012). Performance comparison of benchtop high-throughput sequencing platforms. *Nature Biotechnology*, 30(5):434–439.

[Love et al., 2001] Love, J. C., Wolfe, D. B., Jacobs, H. O., and Whitesides, G. M. (2001). Microscope projection photolithography for rapid prototyping of masters with micron-scale features for use in soft lithography. *Langmuir*, 17(19):60056012.

[Mair et al., 2006] Mair, D. A., Geiger, E., Pisano, A. P., Frchet, J. M., and Svec, F. (2006). Injection molded microfluidic chips featuring integrated interconnects. *Lab on a Chip*, 6(10):13461354.

[Mansuripur et al., 2009] Mansuripur, T. S., Pascall, A. J., and Squires, T. M. (2009). Asymmetric flows over symmetric surfaces: capacitive coupling in induced-charge electro-osmosis. *New Journal of Physics*, 11(7):075030.

[Mark et al., 2010] Mark, D., Haeberle, S., Roth, G., von Stetten, F., and Zengerle, R. (2010). Microfluidic lab-on-a-chip platforms: requirements, characteristics and applications. *Chemical Society Reviews*, 39(3):11531182.

[Martinez et al., 2009] Martinez, A. W., Phillips, S. T., Whitesides, G. M., and Carrilho, E. (2009). Diagnostics for the developing world: microfluidic paper-based analytical devices. *Analytical Chemistry*, 82(1):310.

[McCormick et al., 1997] McCormick, R. M., Nelson, R. J., Alonso-Amigo, M. G., Benvegnu, D. J., and Hooper, H. H. (1997). Microchannel electrophoretic separations of DNA in injection-molded plastic substrates. *Analytical Chemistry*, 69(14):26262630.

[McKnight et al., 2001] McKnight, T. E., Culbertson, C. T., Jacobson, S. C., and Ramsey, J. M. (2001). Electroosmotically induced hydraulic pumping with integrated electrodes on microfluidic devices. *Analytical Chemistry*, 73(16):40454049.

[Melin and Quake, 2007] Melin, J. and Quake, S. R. (2007). Microfluidic large-scale integration: the evolution of design rules for biological automation. *Annu. Rev. Biophys. Biomol. Struct.*, 36:213231.

[Messinger and Squires, 2010] Messinger, R. J. and Squires, T. M. (2010). Suppression of electro-osmotic flow by surface roughness. *Physical review letters*, 105(14):144503.

[Meyvantsson and Beebe, 2008] Meyvantsson, I. and Beebe, D. J. (2008). Cell culture models in microfluidic systems. *Annu. Rev. Anal. Chem.*, 1:423449.

[Mller et al., 2008] Mller, C. B., Loman, A., Pacheco, V., Koberling, F., Willbold, D., Richtering, W., and Enderlein, J. (2008). Precise measurement of diffusion by multi-color dual-focus fluorescence correlation spectroscopy. *EPL (Europhysics Letters)*, 83(4):46001.

[Moran and Posner, 2011] Moran, J. L. and Posner, J. D. (2011). Electrokinetic locomotion due to reaction-induced charge auto-electrophoresis. *J Fluid Mech*, 680:3166.

[Morel et al., 2012] Morel, M., Galas, J. C., Dahan, M., and Studer, V. (2012). Concentration landscape generators for shear free dynamic chemical stimulation. *Lab Chip*.

[Morrison Jr and Osterle, 1965] Morrison Jr, F. A. and Osterle, J. F. (1965). Electrokinetic energy conversion in ultrafine capillaries. *The Journal of Chemical Physics*, 43(6):2111–2115.

[Moseley et al., 2009] Moseley, J. B., Mayeux, A., Paoletti, A., and Nurse, P. (2009). A spatial gradient coordinates cell size and mitotic entry in fission yeast. *Nature*, 459(7248):857860.

[Nagrath et al., 2007] Nagrath, S., Sequist, L. V., Maheswaran, S., Bell, D. W., Irimia, D., Ulkus, L., Smith, M. R., Kwak, E. L., Digumarthy, S., and Muzikansky, A. (2007). Isolation of rare circulating tumour cells in cancer patients by microchip technology. *Nature*, 450(7173):12351239.

[Nathan, 2006] Nathan, C. (2006). Neutrophils and immunity: challenges and opportunities. *Nature Reviews Immunology*, 6(3):173182.

[Ng et al., 2011] Ng, W. Y., Ramos, A., Lam, Y. C., Wijaya, I. P. M., and Rodriguez, I. (2011). DC-biased AC-electrokinetics: a conductivity gradient driven fluid flow. *Lab on a Chip*, 11(24):42414247.

[Nguyen and Wu, 2005] Nguyen, N.-T. and Wu, Z. (2005). Micromixersa review. *Journal of Micromechanics and Microengineering*, 15(2):R1.

[Oddy and Santiago, 2004] Oddy, M. H. and Santiago, J. G. (2004). A method for determining electrophoretic and electroosmotic mobilities using AC and DC electric field particle displacements. *Journal of colloid and interface science*, 269(1):192204.

[Olesen et al., 2006] Olesen, L. H., Bruus, H., and Ajdari, A. (2006). ac electrokinetic micropumps: The effect of geometrical confinement, faradaic current injection, and nonlinear surface capacitance. *Physical Review E*, 73(5):056313.

[Olsen and Adrian, 2000] Olsen, M. G. and Adrian, R. J. (2000). Out-of-focus effects on particle image visibility and correlation in microscopic particle image velocimetry. *Experiments in Fluids*, 29(1):S166–S174.

[Ostrovidov et al., 2012] Ostrovidov, S., Annabi, N., Seidi, A., Ramalingam, M., Dehghani, F., Kaji, H., and Khademhosseini, A. (2012). Controlled release of drugs from gradient hydrogels for high-throughput analysis of CellDrug interactions. *Analytical Chemistry*, 84(3):1302–1309.

[Palacci et al., 2010] Palacci, J., Abcassis, B., Cottin-Bizonne, C., Ybert, C., and Bocquet, L. (2010). Colloidal motility and pattern formation under rectified diffusiophoresis. *Physical Review Letters*, 104(13):138302.

[Palacci et al., 2012] Palacci, J., Cottin-Bizonne, C., Ybert, C., and Bocquet, L. (2012). Osmotic traps for colloids and macromolecules based on logarithmic sensing in salt taxis. *Soft Matter*, 8(4):980994.

[Panda et al., 2008] Panda, P., Ali, S., Lo, E., Chung, B. G., Hatton, T. A., Khademhosseini, A., and Doyle, P. S. (2008). Stop-flow lithography to generate cell-laden microgel particles. *Lab Chip*, 8(7):10561061.

[Park and Wereley, 2013] Park, C. and Wereley, S. T. (2013). Rapid generation and manipulation of microfluidic vortex flows induced by AC electrokinetics with optical illumination. *Lab on a Chip*.

[Park et al., 2010] Park, J. I., Saffari, A., Kumar, S., Gnther, A., and Kumacheva, E. (2010). Microfluidic synthesis of polymer and inorganic particulate materials. *Annual Review of Materials Research*, 40:415443.

[Pascall, 2010] Pascall, A. J. (2010). *Ph.D. Thesis*.

[Pascall and Squires, 2010a] Pascall, A. J. and Squires, T. M. (2010a). An automated, high-throughput experimental system for induced charge electrokinetics. *Lab Chip*, 10(18):23502357.

[Pascall and Squires, 2010b] Pascall, A. J. and Squires, T. M. (2010b). Induced charge electro-osmosis over controllably contaminated electrodes. *Physical review letters*, 104(8):88301.

[Pascall and Squires, 2011] Pascall, A. J. and Squires, T. M. (2011). Electrokinetics at liquid/liquid interfaces. *Journal of Fluid Mechanics*, 684:163.

[Paustian et al., 2013] Paustian, J. S., Azevedo, R. N., Lundin, S.-T. B., Gilkey, M. J., and Squires, T. M. (2013). Microfluidic microdialysis: Spatiotemporal control over solution microenvironments using integrated hydrogel membrane microwindows. *Physical Review X*, 3(4):041010.

[Paxton et al., 2004] Paxton, W. F., Kistler, K. C., Olmeda, C. C., Sen, A., St. Angelo, S. K., Cao, Y., Mallouk, T. E., Lammert, P. E., and Crespi, V. H. (2004). Catalytic nanomotors: Autonomous movement of striped nanorods. *Journal of the American Chemical Society*, 126(41):1342413431.

[Perry et al., 2009] Perry, S. L., Roberts, G. W., Tice, J. D., Gennis, R. B., and Kenis, P. J. A. (2009). Microfluidic generation of lipidic mesophases for membrane protein crystallization. *Crystal Growth & Design*, 9(6):2566–2569.

[Prieve, 2008] Prieve, D. C. (2008). Particle transport: Salt and migrate. *Nature Materials*, 7(10):769–770.

[Prieve et al., 1984a] Prieve, D. C., Anderson, J. L., Ebel, J. P., and Lowell, M. E. (1984a). Motion of a particle generated by chemical gradients. part 2. electrolytes. *Journal of Fluid Mechanics*, 148:247–269.

[Prieve et al., 1984b] Prieve, D. C., Anderson, J. L., Ebel, J. P., and Lowell, M. E. (1984b). Motion of a particle generated by chemical gradients. part 2. electrolytes. *J. Fluid Mech*, 148:247269.

[Raffel et al., 2007] Raffel, M., Willert, C., Wereley, S., and Kompenhans, J. (2007). Particle image VelocimetryA pratical guide. *Particle image velocimetry: a pratical guide*.

[Ramos et al., 2003] Ramos, A., Gonzalez, A., Castellanos, A., Green, N. G., and Morgan, H. (2003). Pumping of liquids with ac voltages applied to asymmetric pairs of microelectrodes. *Physical Review E*, 67(5):056302.

[Ramos et al., 1999] Ramos, A., Morgan, H., Green, N. G., and Castellanos, A. (1999). AC electric-field-induced fluid flow in microelectrodes. *Journal of Colloid and Interface Science*, 217(2):420–422.

[Ramos et al., 2005] Ramos, A., Morgan, H., Green, N. G., Gonzalez, A., and Castellanos, A. (2005). Pumping of liquids with traveling-wave electroosmosis. *Journal of Applied Physics*, 97(8):084906084906.

[Randall et al., 2006] Randall, G. C., Schultz, K. M., and Doyle, P. S. (2006). Methods to electrophoretically stretch DNA: microcontractions, gels, and hybrid gel-microcontraction devices. *Lab on a Chip*, 6(4):516525.

[Reyes et al., 2002] Reyes, D. R., Iossifidis, D., Auroux, P.-A., and Manz, A. (2002). Micro total analysis systems. 1. introduction, theory, and technology. *Analytical chemistry*, 74(12):26232636.

[Rice and Whitehead, 1965] Rice, C. L. and Whitehead, R. (1965). Electrokinetic flow in a narrow cylindrical capillary. *The Journal of Physical Chemistry*, 69(11):40174024.

[Ryu et al., 2010] Ryu, J. C., Park, H. J., Park, J. K., and Kang, K. H. (2010). New electrohydrodynamic flow caused by the onsager effect. *Physical Review Letters*, 104(10):104502.

[Sagle et al., 2009] Sagle, A. C., Van Wagner, E. M., Ju, H., McCloskey, B. D., Freeman, B. D., and Sharma, M. M. (2009). PEG-coated reverse osmosis membranes: Desalination properties and fouling resistance. *Journal of Membrane Science*, 340(12):92–108.

[Santiago et al., 1998] Santiago, J. G., Wereley, S. T., Meinhart, C. D., Beebe, D. J., and Adrian, R. J. (1998). A particle image velocimetry system for microfluidics. *Experiments in fluids*, 25(4):316319.

[Schnitzer and Yariv, 2012a] Schnitzer, O. and Yariv, E. (2012a). Induced-charge electro-osmosis beyond weak fields. *Phys. Rev. E*, 86(6):061506.

[Schnitzer and Yariv, 2012b] Schnitzer, O. and Yariv, E. (2012b). Macroscale description of electrokinetic flows at large zeta potentials: Nonlinear surface conduction. *Physical Review E*, 86(2):021503.

[Scrimgeour et al., 2011] Scrimgeour, J., Cho, J. K., Breedveld, V., and Curtis, J. (2011). Microfluidic dialysis cell for characterization of macromolecule interactions. *Soft Matter*, 7(10):4762.

[Seong et al., 2002] Seong, G. H., Zhan, W., and Crooks, R. M. (2002). Fabrication of microchambers defined by photopolymerized hydrogels and weirs within microfluidic systems: Application to DNA hybridization. *Analytical chemistry*, 74(14):33723377.

[Shaeiwitz and Lechnick, 1984] Shaeiwitz, J. A. and Lechnick, W. J. (1984). Ternary diffusion formulation for diffusiophoresis. *Chemical engineering science*, 39(5):799807.

[Sharifi-Mood et al., 2013] Sharifi-Mood, N., Koplik, J., and Maldarelli, C. (2013). Molecular dynamics simulation of the motion of colloidal nanoparticles in a solute concentration gradient and a comparison to the continuum limit. *Physical Review Letters*, 111(18):184501.

[Sharp et al., 2011] Sharp, K. V., Yazdi, S. H., and Davison, S. M. (2011). Localized flow control in microchannels using induced-charge electroosmosis near conductive obstacles. *Microfluidics and Nanofluidics*, 10(6):12571267.

[Shepherd et al., 2008] Shepherd, R. F., Panda, P., Bao, Z., Sandhage, K. H., Hatton, T. A., Lewis, J. A., and Doyle, P. S. (2008). Stop-flow lithography of colloidal, glass, and silicon microcomponents. *Advanced Materials*, 20(24):47344739.

[Shin et al., 2011] Shin, W., Lee, J. M., Nagarale, R. K., Shin, S. J., and Heller, A. (2011). A miniature, nongassing electroosmotic pump operating at 0.5 v. *Journal of the American Chemical Society*, 133(8):2374–2377.

[Snyder et al., 2013] Snyder, J. L., Getpreecharsawas, J., Fang, D. Z., Gaborski, T. R., Striemer, C. C., Fauchet, P. M., Borkholder, D. A., and McGrath, J. L. (2013). High-performance, low-voltage electroosmotic pumps with molecularly thin silicon nanomembranes. *Proceedings of the National Academy of Sciences*, 110(46):18425–18430. PMID: 24167263.

[Song et al., 2004a] Song, S., Singh, A. K., and Kirby, B. J. (2004a). Electrophoretic concentration of proteins at laser-patterned nanoporous membranes in microchips. *Analytical Chemistry*, 76(15):4589–4592.

[Song et al., 2004b] Song, S., Singh, A. K., Shepodd, T. J., and Kirby, B. J. (2004b). Microchip dialysis of proteins using in situ photopatterned nanoporous polymer membranes. *Analytical Chemistry*, 76(8):2367–2373.

[Soni, 2008] Soni, G. (2008). Ph.D. thesis.

[Sperling and Parak, 2010] Sperling, R. A. and Parak, W. J. (2010). Surface modification, functionalization and bioconjugation of colloidal inorganic nanoparticles. *Philosophical Transactions of the Royal Society A: Mathematical, Physical and Engineering Sciences*, 368(1915):13331383.

[Squires, 2008] Squires, T. M. (2008). Electrokinetic flows over inhomogeneously slipping surfaces. *Physics of Fluids*, 20(9):092105092105.

[Squires, 2009] Squires, T. M. (2009). Induced-charge electrokinetics: fundamental challenges and opportunities. *Lab on a Chip*, 9(17):24772483.

[Squires and Bazant, 2004] Squires, T. M. and Bazant, M. Z. (2004). Induced-charge electro-osmosis. *Journal of Fluid Mechanics*, 509(217-252):7280.

[Squires and Bazant, 2006] Squires, T. M. and Bazant, M. Z. (2006). Breaking symmetries in induced-charge electro-osmosis and electrophoresis. *Journal of Fluid Mechanics*, 560:65102.

[Squires and Quake, 2005] Squires, T. M. and Quake, S. R. (2005). Microfluidics: Fluid physics at the nanoliter scale. *Reviews of modern physics*, 77(3):977.

[Staffeld and Quinn, 1989a] Staffeld, P. O. and Quinn, J. A. (1989a). Diffusion-induced banding of colloid particles via diffusiophoresis: 1. electrolytes. *Journal of colloid and interface science*, 130(1):6987.

[Staffeld and Quinn, 1989b] Staffeld, P. O. and Quinn, J. A. (1989b). Diffusion-induced banding of colloid particles via diffusiophoresis: 2. non-electrolytes. *Journal of colloid and interface science*, 130(1):88100.

[Streets and Quake, 2010] Streets, A. M. and Quake, S. R. (2010). Ostwald ripening of clusters during protein crystallization. *Physical review letters*, 104(17):178102.

[Strickland et al., 2010] Strickland, D. G., Suss, M. E., Zangle, T. A., and Santiago, J. G. (2010). Evidence shows concentration polarization and its propagation can be key factors determining electroosmotic pump performance. *Sensors and Actuators B: Chemical*, 143(2):795798.

[Studer et al., 2004a] Studer, V., Hang, G., Pandolfi, A., Ortiz, M., French Anderson, W., and Quake, S. R. (2004a). Scaling properties of a low-actuation pressure microfluidic valve. *Journal of applied physics*, 95(1):393398.

[Studer et al., 2004b] Studer, V., Ppin, A., Chen, Y., and Ajdari, A. (2004b). An integrated AC electrokinetic pump in a microfluidic loop for fast and tunable flow control. *Analyst*, 129(10):944949.

[Sugioka, 2011] Sugioka, H. (2011). Asymmetrical reverse vortex flow due to induced-charge electro-osmosis around carbon stacking structures. *Physical Review E*, 83(5):056321.

[Takahashi et al., 2003] Takahashi, T., Ogata, S., Nishizawa, M., and Matsue, T. (2003). A valveless switch for microparticle sorting with laminar flow streams and electrophoresis perpendicular to the direction of fluid stream. *Electrochemistry communications*, 5(2):175177.

[Tan et al., 2010] Tan, D. C.-W., Yung, L.-Y. L., and Roy, P. (2010). Controlled microscale diffusion gradients in quiescent extracellular fluid. *Biomedical microdevices*, 12(3):523532.

[Tentori and Herr, 2011] Tentori, A. M. and Herr, A. E. (2011). Photopatterned materials in bioanalytical microfluidic technology. *Journal of Micromechanics and Microengineering*, 21(5):054001.

[Thorsen et al., 2002] Thorsen, T., Maerkl, S. J., and Quake, S. R. (2002). Microfluidic large-scale integration. *Science*, 298(5593):580584.

[Unger et al., 2000] Unger, M. A., Chou, H.-P., Thorsen, T., Scherer, A., and Quake, S. R. (2000). Monolithic microfabricated valves and pumps by multilayer soft lithography. *Science*, 288(5463):113116.

[Urbanski et al., 2006] Urbanski, J. P., Thorsen, T., Levitan, J. A., and Bazant, M. Z. (2006). Fast ac electro-osmotic micropumps with nonplanar electrodes. *Applied Physics Letters*, 89(14):143508143508.

[van Hal et al., 1996] van Hal, R. E. G., Eijkel, J. C. T., and Bergveld, P. (1996). A general model to describe the electrostatic potential at electrolyte oxide interfaces. *Advances in Colloid and Interface Science*, 69(13):31–62.

[VanDersarl et al., 2011] VanDersarl, J. J., Xu, A. M., and Melosh, N. A. (2011). Rapid spatial and temporal controlled signal delivery over large cell culture areas. *Lab on a Chip*, 11(18):3057.

[Volkmuth and Austin, 1992] Volkmuth, W. D. and Austin, R. H. (1992). DNA electrophoresis in microlithographic arrays. *Nature*, 358(6387):600602.

[Vyawahare et al., 2008] Vyawahare, S., Sitaula, S., Martin, S., Adalian, D., and Scherer, A. (2008). Electronic control of elastomeric microfluidic circuits with shape memory actuators. *Lab Chip*, 8(9):15301535.

[Wheeler et al., 2003] Wheeler, A. R., Throndset, W. R., Whelan, R. J., Leach, A. M., Zare, R. N., Liao, Y. H., Farrell, K., Manger, I. D., and Daridon, A. (2003). Microfluidic device for single-cell analysis. *Analytical chemistry*, 75(14):35813586.

[Whitesides, 2006] Whitesides, G. M. (2006). The origins and the future of microfluidics. *Nature*, 442(7101):368373.

[Wilding et al., 1994] Wilding, P., Shoffner, M. A., and Kricka, L. J. (1994). PCR in a silicon microstructure. *Clinical Chemistry*, 40(9):1815–1818. PMID: 8070107.

[Wrger, 2010] Wrger, A. (2010). Thermal non-equilibrium transport in colloids. *Reports on Progress in Physics*, 73(12):126601.

[Wu and Li, 2008] Wu, Z. and Li, D. (2008). Micromixing using induced-charge electrokinetic flow. *Electrochimica Acta*, 53(19):5827–5835.

[Wunderlich et al., 2010] Wunderlich, B. K., Kleinger, U. A., and Bausch, A. R. (2010). Diffusive spreading of time-dependent pressures in elastic microfluidic devices. *Lab on a Chip*, 10(8):10251029.

[Xia and Whitesides, 1998] Xia, Y. and Whitesides, G. M. (1998). Soft lithography. *Annual review of materials science*, 28(1):153184.

[Yao et al., 2003] Yao, S., Hertzog, D. E., Zeng, S., Mikkelsen Jr, J. C., and Santiago, J. G. (2003). Porous glass electroosmotic pumps: design and experiments. *Journal of Colloid and Interface Science*, 268(1):143153.

[Yao and Santiago, 2003] Yao, S. and Santiago, J. G. (2003). Porous glass electroosmotic pumps: theory. *Journal of Colloid and Interface Science*, 268(1):133142.

[Yldrm et al., 2012] Yldrm, E., Arkan, M. A., and Klah, H. (2012). A normally closed electrostatic parylene microvalve for micro total analysis systems. *Sensors and Actuators A: Physical*, 181:8186.

[Zhan et al., 2002] Zhan, W., Seong, G. H., and Crooks, R. M. (2002). Hydrogel-based microreactors as a functional component of microfluidic systems. *Analytical Chemistry*, 74(18):4647–4652.

[Zhao and Yang, 2011] Zhao, C. and Yang, C. (2011). ac electrokinetic phenomena over semiconductive surfaces: Effective electric boundary conditions and their applications. *Physical Review E*, 83(6):066304.

[Zheng et al., 2012] Zheng, Y., Chen, J., Craven, M., Choi, N. W., Totorica, S., Diaz-Santana, A., Kermani, P., Hempstead, B., Fischbach-Teschl, C., Lpez, J. A., and Stroock, A. D. (2012). In vitro microvessels for the study of angiogenesis and thrombosis. *Proceedings of the National Academy of Sciences*, 109(24):9342–9347. PMID: 22645376.

Appendices

Appendix A

ICEO Pump: Reciprocal Theorem calculation

The calculation for maximum pressure and flow rate of the rectangular array design of ICEO micropump is performed in 3D and uses the Reciprocal Theorem,

$$\int \hat{\mathbf{u}} \cdot \mathbf{T} \cdot \hat{\mathbf{n}} dS = \int \mathbf{u} \cdot \hat{\mathbf{T}} \cdot \hat{\mathbf{n}} dS, \tag{A.1}$$

where $\mathbf{u}$ and $\mathbf{T}$ are the ICEO driven flow and $\hat{\mathbf{u}}$ and $\hat{\mathbf{T}}$ are Poiseuille flow in a rectangular channel [Bruus, 2007],

$$\hat{\mathbf{u}}_y(x,z) = \frac{4s^2}{\pi^3 \eta} \frac{\partial \hat{P}}{\partial y} \sum_{n,odd}^{\infty} \frac{1}{n^3} \left(1 - \frac{\cosh \frac{n\pi z}{s}}{\cosh \frac{n\pi h}{2s}} \right) \sin \frac{n\pi x}{s}. \tag{A.2}$$

I assume fully developed Poiseuille flow in the channel running parallel to the longer rectangle axis. This assumption is valid for long pillars ($l \gg w$), but introduces an error otherwise. However, an extremely accurate expression is unnecessary to satisfy the goal of obtaining an approximate design expression.

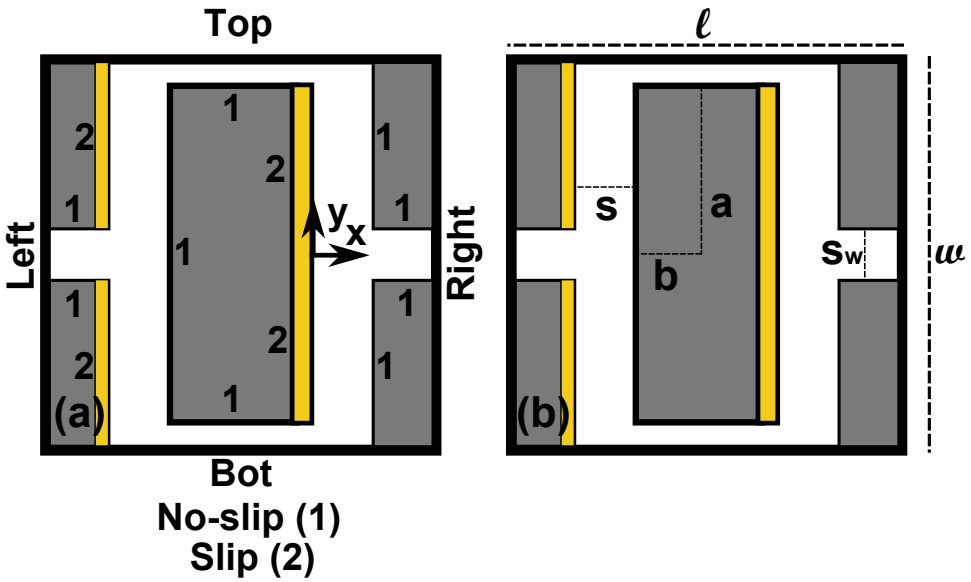

Figure A.1: **(a)** Boundary conditions for Reciprocal Theorem calculation. **(b)** Geometric parameter definitions.

Figure A.1 shows the geometry of the unit cell. While this unit cell could actually be broken down even further into four separate cells, this unit cell allows a more intuitive derivation. First, the boundary conditions must be defined. In Figure 1, each of the surfaces in the unit cell cross-section have been labeled, while 'floor' and 'ceiling' (not shown) represent the bottom and top of the channel. The

conditions on the micropillar surface, floor, and ceiling are listed first:

$$\hat{\mathbf{u}}_{no-slip} = \hat{\mathbf{u}}_{slip} = \hat{\mathbf{u}}_{floor} = \hat{\mathbf{u}}_{ceiling} = \mathbf{u}_{no-slip} = \mathbf{u}_{floor} = \mathbf{u}_{ceiling} = \mathbf{0} \tag{A.3}$$

$$\mathbf{u}_{slip} = \mathbf{u}_s \tag{A.4}$$

The analysis assumes a thin double layer ($\lambda_D \ll s$), allowing $\mathbf{u}_s$ to be modeled as a slip velocity. The Helmholtz-Smoluchowski velocity is often used, but slip velocity will vary greatly depending on experimental conditions, so I first solve the problem for a generic slip velocity.

The symmetry conditions along 'top' and 'bot' allow further simplification,

$$\mathbf{u}_{top} = \mathbf{u}_{bot} = (u_x, 0, 0); \tag{A.5}$$

$$\hat{\mathbf{u}}_{top} = \hat{\mathbf{u}}_{bot} = (\hat{u}_x, 0, 0); \tag{A.6}$$

$$T_{bot,xy} = T_{top,xy} = \hat{T}_{bot,xy} = \hat{T}_{top,xy} = 0; \tag{A.7}$$

$$\hat{\mathbf{n}}_{bot} = (0, 1, 0) = -\hat{\mathbf{n}}_{top}; \tag{A.8}$$

Taking the dot product of all the vectors results in zero contribution from the 'top' and 'bot' surfaces. Equation A.1 has now been reduced to the following:

$$\int_{left,right} \hat{\mathbf{u}} \cdot \mathbf{T} \cdot \hat{\mathbf{n}} dA = \int_{left,right} \mathbf{u} \cdot \hat{\mathbf{T}} \cdot \hat{\mathbf{n}} dA + \int_{slip} \mathbf{u}_s \cdot \hat{\mathbf{T}} \cdot \hat{\mathbf{n}} dA \tag{A.9}$$

Simplifying the LHS by taking the dot product of the normal,

$$\int_{left} \hat{\mathbf{u}} \cdot \mathbf{T} \cdot \hat{\mathbf{n}} dA + \int_{right} \hat{\mathbf{u}} \cdot \mathbf{T} \cdot \hat{\mathbf{n}} dA = \int_{left} (\hat{u}_x T_{xx} + \hat{u}_y T_{yx} + \hat{u}_z T_{zx}) dA - \int_{right} (\hat{u}_x T_{xx} + \hat{u}_y T_{yx} + \hat{u}_z T_{zx}) dA \tag{A.10}$$

Both velocity profiles are the same is the same on the left and right side. For this reason, the stress tensors are also identical, except for the pressure term, resulting in.

$$\int_{left} \hat{\mathbf{u}} \cdot \mathbf{T} \cdot \hat{\mathbf{n}} dA + \int_{right} \hat{\mathbf{u}} \cdot \mathbf{T} \cdot \hat{\mathbf{n}} dA = \int_{right} \hat{u}_x P dA - \int_{left} \hat{u}_x P dA. \tag{A.11}$$

The pressure at these locations is not a strong function of y, so I assume it is constant in y, allowing a solution for the LHS

$$\int_{left,right} \hat{\mathbf{u}} \cdot \mathbf{T} \cdot \hat{\mathbf{n}} dA = \hat{Q} \Delta P \tag{A.12}$$

where $\Delta P = P_{right} - P_{left}$. Repeating this procedure for the second remaining integral results in

$$\int_{left,right} \mathbf{u} \cdot \hat{\mathbf{T}} \cdot \hat{\mathbf{n}} dA = Q \Delta \hat{P} \tag{A.13}$$

Equation A.1 has now become

$$\hat{Q} \Delta P - Q \Delta \hat{P} = 4 \int_{slip} \mathbf{u}_s \cdot \hat{\mathbf{T}} \cdot \hat{\mathbf{n}} dA \tag{A.14}$$

noting that the four slipping surfaces provide the same contribution. Noting that $\mathbf{u}_s$=(0,u_s,0) allows further simplification.

$$\hat{Q} \Delta P - Q \Delta \hat{P} = 4 \int_{slip} \eta u_s \frac{\partial \hat{u}_y}{\partial x} dy dz \tag{A.15}$$

The hatted velocity is specified by Poiseuille flow, so that

$$\left. \frac{\partial \hat{u}_y}{\partial x} \right|_{x=wall} = \frac{4s}{\pi^2 \eta} \frac{\partial \hat{P}}{\partial y} \sum_{n,odd}^{\infty} \frac{1}{n^2} \left(1 - \frac{\cosh \frac{n\pi z}{s}}{\cosh \frac{n\pi h}{2s}} \right) \tag{A.16}$$

Integrating out the z-dependence,

$$\begin{aligned}\hat{Q}\Delta P - Q\Delta\hat{P} &= 4\int_{slip}\eta u_s\frac{\partial\hat{u}_y}{\partial x}dydz \\ &= \frac{16s}{\pi^2}\frac{\partial\hat{P}}{\partial y}\int_{slip}u_s(y)\sum_{n,odd}^{\infty}\frac{1}{n^2}\left(1-\frac{\cosh\frac{n\pi z}{s}}{\cosh\frac{n\pi h}{2s}}\right)dydz \\ &= \frac{16s^2}{\pi^2}\frac{\partial\hat{P}}{\partial y}\left(\int_{slip}u_s(y)dy\right)\sum_{n,odd}^{\infty}\frac{h}{sn^2}\left(1-\frac{2s\tanh\frac{n\pi h}{2s}}{hn\pi}\right) \\ &= \frac{16s^2}{\pi^2}\frac{\partial\hat{P}}{\partial y}f(A)\int_{slip}u_s(y)dy\end{aligned} \tag{A.17}$$

where $A = h/s$ is the gap aspect ratio and $f(A)$ is the entire summation (for A=1, f(A)= 0.617). The Poiseuille flow splits down the two halves of the unit cell so that the pressure gradient along each slipping surface is half the total drop across the cell, $\frac{\partial\hat{P}}{\partial y} \approx \frac{-\Delta\hat{P}}{2(2a+4b+2s+s_w)} = \frac{-\Delta\hat{P}}{p}$ with unit cell perimeter p. Q_{max} for a cell is Q when ΔP=0, resulting in

$$Q_{max} = \frac{16s^2}{p\pi^2}f(A)\int_{slip}u_s(y)dy \tag{A.18}$$

Likewise, the cell ΔP_{max} is given when $Q = 0$. $\hat{Q}$ is the pressure driven flow rate through the entire cell, which is twice the flow rate through an individual channel along a slipping surface,

$$\hat{Q} = \frac{16s^4}{\pi^4\eta}\frac{\partial\hat{P}}{\partial y}\sum_{n,odd}^{\infty}\frac{h}{sn^4}\left(1-\frac{2s}{n\pi h}\tanh\frac{n\pi h}{2s}\right), \tag{A.19}$$

the maximum pressure for a cell is

$$\Delta P_{max} = \frac{\pi^2 \eta}{s^2} \frac{f(A)}{g(A)} \int_{slip} u_s(y) dy \tag{A.20}$$

where g(A) is summation shown in $\hat{Q}$ (for A=1, g(A)=0.428, and f(A)/g(A)=1.44).

The total pump flow rate and pressure drop can be found for an NxM array of unit cells with total length L and total width W.

$$N = \frac{L}{l} = \frac{L}{4b + 2s} \tag{A.21}$$

$$M = \frac{W}{w} = \frac{W}{2a + s_w} \tag{A.22}$$

The maximum total flow rate is

$$Q_{max} = MQ_{cell} \tag{A.23}$$
$$= \frac{W}{2a + s_w} \frac{16 s^2}{p\pi^2} f(A) \int_{slip} u_s(y) dy.$$

The maximum total pressure is

$$\Delta P_{max} = N \Delta P_{cell}$$
$$= \frac{L}{l} \frac{\pi^2 \eta}{s^2} \frac{f(A)}{g(A)} \int_{slip} u_s(y) dy. \tag{A.24}$$

To simplify, I insert values to used for the fabrication method presented here. In particular, I set $A = 1$, $s = 2b$, $4s = l$, and $2.5 s_w = a$. This results in a maximum pressure and flow rate

$$\boxed{\Delta P_{max} = 3.6\frac{L\eta}{s^3}\int_{slip} u_s(y)dy} \tag{A.25}$$

$$\boxed{Q_{max} = 0.21\frac{W}{a}\frac{s^2}{(a+2s)}\int_{slip} u_s(y)dy} \tag{A.26}$$

The above equations could be combined with numerical computation of slip velocity depending on the physics one wants to incorporate, however this goes beyond the scope of this work. My goal is to derive a scaling expression, which can be accomplished by inserting the Helmholtz-Smoluchowski velocity for time-averaged ICEO flow in the low frequency, low-ζ limit with correction factor Λ,

$$u_s = \frac{\epsilon E\zeta_i(y)}{2\eta} = \frac{\Lambda\epsilon E^2 y}{2\eta}. \tag{A.27}$$

In this case, the equations become

$$\Delta P_{max} = 0.9\frac{\Lambda\epsilon L a^2 E^2}{s^3} = 0.9\frac{\Lambda\epsilon L a^2\phi^2}{W^2 s^3} \tag{A.28}$$

$$Q_{max} = 0.05\frac{\Lambda\epsilon W a s^2 E^2}{\eta(a+2s)} = 0.05\frac{\Lambda\epsilon a s^2\phi^2}{W\eta(a+2s)} \tag{A.29}$$

where ϕ is the amplitude of the applied voltage.

Appendix B

Induced charge elctroosmotic flow using silicon micropillars

B.1 Introduction

In this section, I generate ICEO flow using conductive silicon micropillars and measure the velocity. Recent theoretical work has predicted that ICEO can also occur over semiconducting surfaces, including silicon [Zhao and Yang, 2011], but ICEO flow over a semiconducting surface has never been experimentally measured in the literature. The original motivation of this work was to allow the use of silicon micropillars for pumping and mixing within microfluidic devices. Although issues were encountered with electrochemical reactions that would have to be overcome

before those applications could be pursued, I include this demonstration because of its novelty as a proof-of-concept for ICEO at semiconductor-electrolyte interfaces.

B.2 Micropillar fabrication

The goal of the fabrication process was to produce an electrically isolated conductive silicon micropillar for insertion into a microfluidic channel. The process used silica as an etch mask for the silicon because of the high selectivity (100:1 etch rate for silicon:silica) in Bosch etching.

A silicon-on-insulator (SOI) wafer (fig. B.1a) was purchased as the starting material (University Wafer lot 2219). These wafers consist of a silica (buried oxide, "BOX") layer sandwiched between two silicon wafers. The electrical properties of the two silicon wafers can be independently selected. The top ("device") layer was selected to have high conductivity to maximize the ICEO flow at the surface. The bottom ("handle") layer was selected to have a low conductivity to minimize stray flow toward the ground electrode due to capacitive coupling [Mansuripur et al., 2009], which was observed in early experiments with conductive handles. The wafer used in the below experiment was a 100 mm diameter wafer with 50 μm thick device layer (n-doped with As, resistivity $0.001 - 0.005$ Ω·cm), 2 μm thick

BOX, and 400 μm thick handle (undoped, resistivity >1000 Ω·cm) (University Wafer lot 2219).

A silica etch mask had to be patterned before performing the Bosch etch. The wafer was first cleaned in a Piranha solution (3:1 H_2SO_4:H_2O_2) for 3' at 120°C. A dehydration bake was then performed for 5' at 200° C on a hot plate. A 1 μm silica layer was deposited using Plasma-Enhanced Chemical Vapor Deposition (PECVD) (fig. B.1b). A circular photoresist shape (75 μm diameter) was patterned on this layer using standard photolithography (fig. B.1c). The oxide was etched in buffered HF for 5' until the oxide had been removed (fig. B.1d). The wafer was rinsed in H_2O for several minutes. The photoresist was then removed by sonicating in acetone and isopropanol for 3' each (fig. B.1e). An O_2 plasma clean was performed (Technics plasma chamber) at 300 mTorr and 100 Watts for 2' to remove any residual photoresist. The Bosch etch was then performed for 47'. The etch automatically stopped when it reached the buried oxide. The resulting wafer had a 50 μm tall, 50 μm diameter conductive silicon pillar atop an oxide surface. This was again Piranha cleaned for 3' at 120°C.

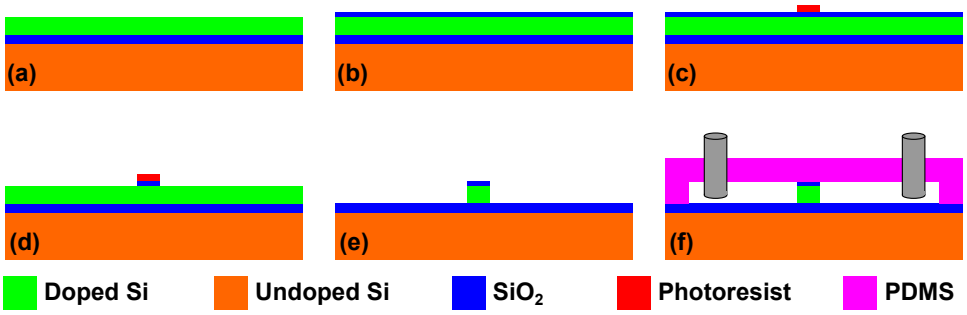

Figure B.1: Fabrication of silicon micropillars for ICEO. **(a)** Silicon-on-Insulator wafer. **(b)** PECVD deposition of SiO_2. **(c)** Photolithography of circular pattern. **(d)** HF etch of oxide. **(e)** Bosch etch of top silicon layer. **(f)** Bonding to PDMS channel with metal pins inserted to serve as electrodes and inlet ports.

B.3 Experimental method

The micropillar had to be inserted into a microchannel to test the ICEO flow. A PDMS microchannel was fabricated using standard soft lithography methods [Xia and Whitesides, 1998] with 32mmx5mmx50μm. After bonding the channel to the etched SOI wafer, hollow stainless steel pins (New England Small Tube) were inserted at the ends of the channel. The channel was filled with 100 μM KCl electrolyte and tracer particles (Bangs Labs FS03F, 500nm diameter fluorescent polystyrene). An AC electric field was applied between two metal pins as described previously [Pascall and Squires, 2010a]. Videos of the resulting ICEO flow were recorded using an upright microscope looking through the PDMS and 20x objective. The velocity was measured by applying a μPIV MATLAB algorithm to the videos.

B.4 Results

Fig. B.2 shows a typical flow profile around a silicon micropillar (100 Hz, 500 V_{pp}/cm, 2 second superposed image, 100 μM KCl with 500 nm fluorescent polystyrene tracers). A quadripolar flow profile was observed, which is expected for ICEO flow around polarizable cylinders [Squires and Bazant, 2004]. This profile was superposed with a stray flow due to capacitive coupling, which grew as the experiment progressed [Mansuripur et al., 2009]

The maximum observed ICEO velocity was 30 μm/s. Comparing to eqn. 2.4, the correction factor $\Lambda \approx .004$, which is similar to the value for bare metal surfaces in Ch.3. However, the velocity decreased as the experiment progressed, most likely due to surface oxidation by Faradaic reactions. The experimental system was not ideal for quantitative measurements because of the systematic decrease in velocity, as well as capacitive coupling driven flow that was sometimes observed after long periods of operation, and the need to focus the microsope through PDMS, which scatters light and lowers image quality. However, it is the first demonstration of ICEO flow around a semiconductor, which qualitatively validates the theoretical prediction of such flow [Zhao and Yang, 2011] and expands the field of possible materials that can be used for nonlinear electrokinetic pumping and mixing in microfluidic devices.

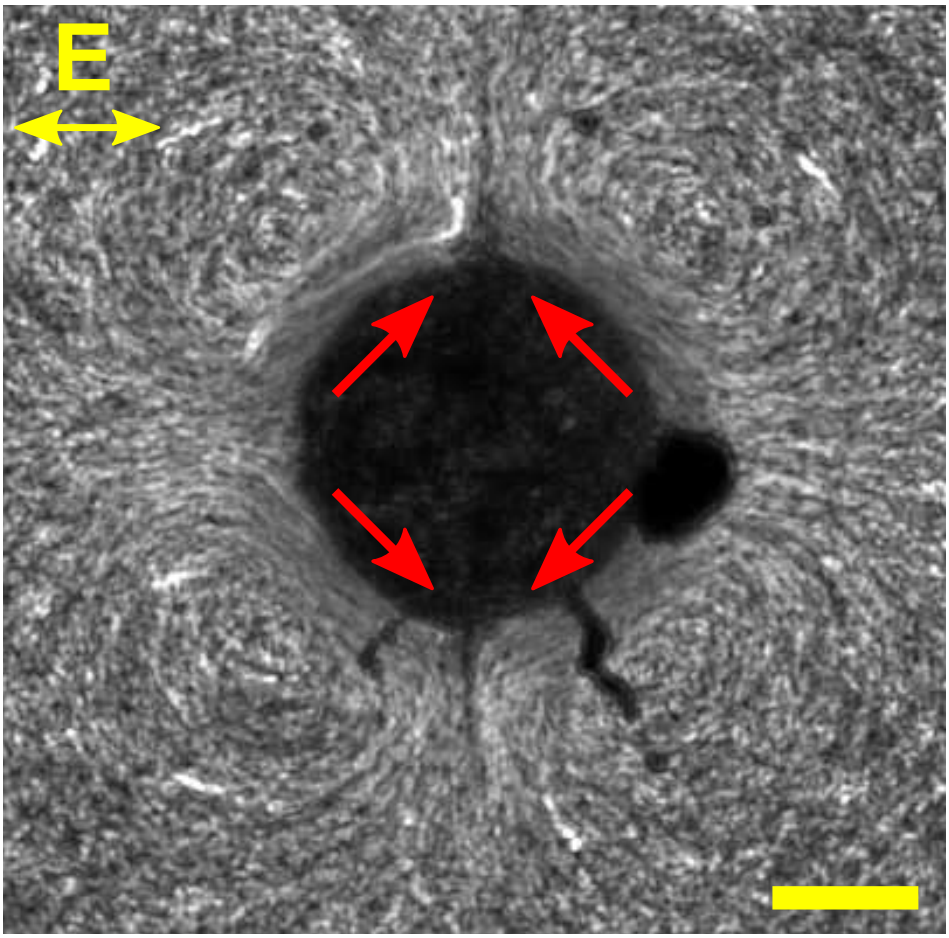

Figure B.2: Background-subtracted, superposed image showing 4 seconds of flow from ICEO around a silicon micropillar. Red arrows show direction of flow, while noncircular black regions are present because stuck beads were subtracted in the average image. Scale bar: 25 μm.

Appendix C

Colloid motion in large ethanol-water gradients

Experiments were performed as in Chapter 7 but with larger ethanol gradients. The experiments resulted in qualitatively different behavior which appears to be convective rather than phoretic, and is therefore excluded from the mobility measurements. The solutions contained 16.9/8.5/0M ethanol in water (99 mol% to 0 mol% ethanol gradient) with 5 mM KCl in each channel, and 500 nm fluorescent polystyrene colloids (Bangs Labs FS03F) in the middle channel. The gels were fabricated using the original HMM procedure described in Chapter 4. The images are included to demonstrate the qualitative behavior at large ethanol gradients.

Fig. C.1a shows the general behavior at these ethanol concentrations. A 10 second superposed image of the colloid motion is shown. The particles on the right side (high water) move toward the right, while the particles on the left (low water) move to the left. However, the particles on the left do not stick to the gel, and instead accumulate near the gel surface. This experiment was performed in a device after a full day of solvophoresis experiments. Fig. C.1b shows the same experimental conditions, but performed in a new device with freshly prepared hydrogels. After the flow stopped, large swirls were observed to develop on the ethanol-rich side, which were clearly convective. The water-rich side still showed unaltered solvophoresis. This image superposes frames 0-10 seconds after flow stoppage. Fig. C.1c shows the same experiment 10-20 seconds after flow stoppage. More convective rolls begin to develop. Fig. C.1d shows a combined phase contrast and fluorescence image of the device after the experiment had been performed. Droplets of PEG-DA have deposited in a plume shape on the surface of the device. This could indicate a flow through the membrane which is dissolving uncrosslinked PEG-DA is being forced against a diffusio-osmotic flow.

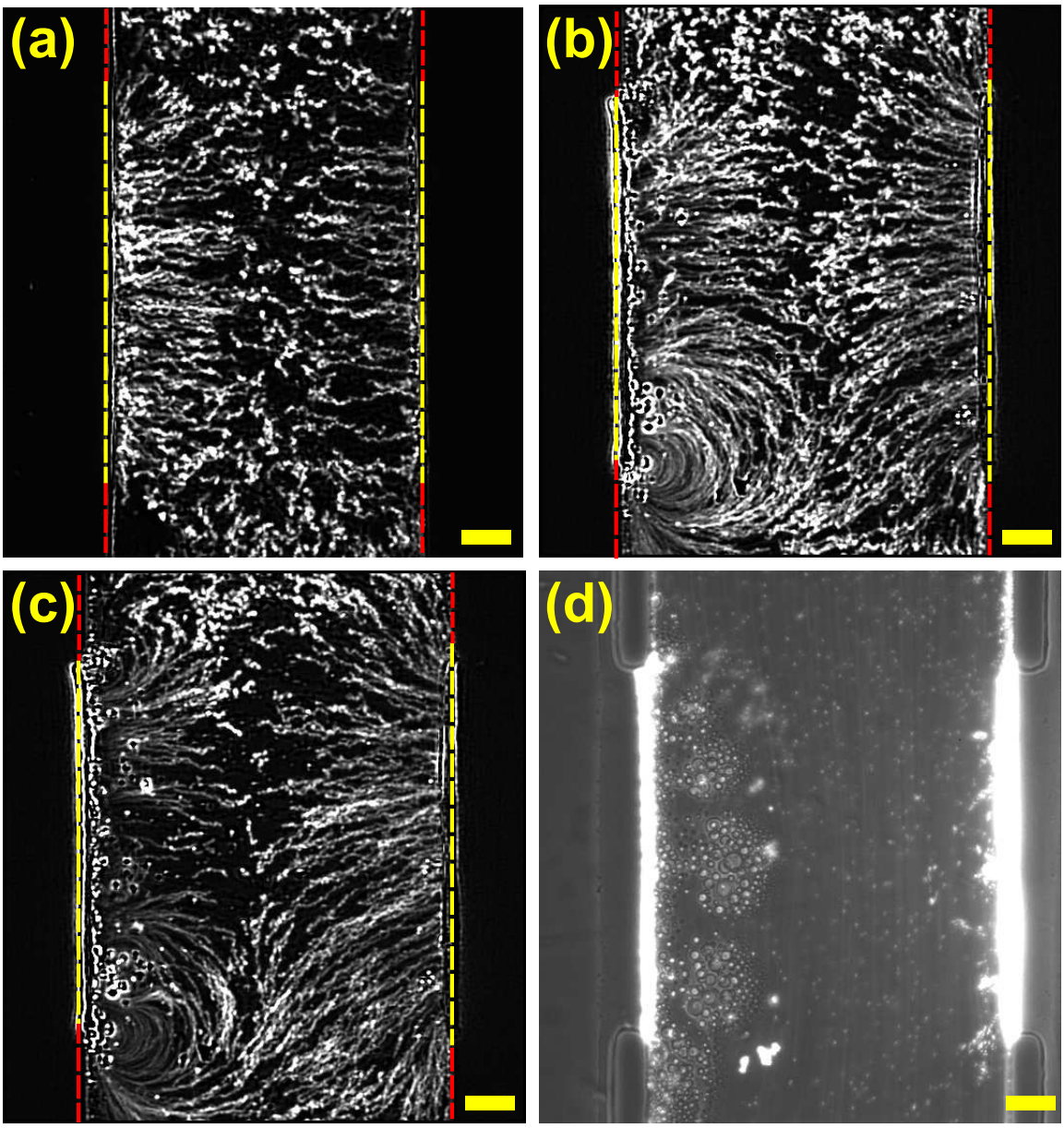

Figure C.1: **(a)** Colloid motion under 99% to 0% EtOH gradient in a device which had previously been washed with ethanol for several hours. **(b)** Colloid motion using the same solutions but with freshly prepared hydrogels. 0-10 seconds after flow stoppage. **(c)** 10-20 seconds after flow stoppage. **(d)** Phase contrast and fluorescence image of device after experiment shown in (b)-(c). PEG-DA droplets have deposited on the surface of the device near the ethanol-rich gel. (Scale bars: 20 μm.)

Appendix D

Copyright License